TABLE of CONTENTS

LIST of FIGURES

LIST of TABLES

LIST OF SYMBOLS/ABBREVIATIONS

BET	Surface area
CB	Conduction band
Ce_2O_3	Cerium oxide
d	Particle Size Diameter
$d_{anatase}$	Particle Size Diameter of Anatase
d_{rutile}	Particle Size Diameter of Rutile
e^-	Electron
E_{bg}	Band Gap Energy
EDAX	Energy Dispersive X-Ray
FWHM	Full Width Half Maximum
FTIR	Infrared Spectroscopy
h^+	Hole
MeO	Methyl Orange
l	Path Length of the Spectrophotometer
La_2O_3	Lanthanum oxide
λ	Wavelength of X-ray Radiation
PILCs	Pillared Clays
XRD	X–Ray Diffraction
SEM	Scanning Electron Microscopy
TGA	Thermogravimetric Analysis
TEM	Transmission eElectron Microscopy
θ	Angle Between X-ray Radiation
TiO_2	Titanium Dioxide
UV-Vis	Ultraviole-Visible Spectrophotometer
VB	Valence Band
Y_2O_3	Yttrium Oxide

2. THEORY

2.1. Zeolites

Zeolites have been an object of scientific research and a material beneficial to mankind for more than 200 years since their discovery in 1756 [1]. However, it was not until 10–15 years ago that zeolites attracted the keen interest of photochemists who wanted to use them for their research. Since then, an active interplay of zeolites with photochemistry has started. Photochemists are most interested in controlling chemical reactions with the aid of zeolites and other supramolecular assemblies, aimed at constructing artificial photosynthetic systems, controlling chirarity and inventing nanoscale advanced materials. Zeolites are found to be particularly useful for such purposes since they host various molecules including organics in their cavities and channels, and such inclusions have often been shown to modify the normal solution photochemistry of a given species. The confinement of molecules within the constrained space and the catalytic activity of the surface adsorption sites were considered decisive for product distributions unique to zeolites. On the other hand, zeolite science covers a broad spectrum, from synthesis to structural characterization, adsorption and transport phenomena, and applications such as catalysts and other classical uses (adsorbents or desiccants, water softeners, soil improvers, and so forth). Furthermore, zeolites have been recognized as new materials for optical and electronic applications, such as lasers, quantum dots and second harmonic generation, in recent years [2, 3]. These days, zeolite science as materials science is getting closer and closer to photochemistry than ever before.

2.1.1. Structure and Chemical Properties of Zeolites

Zeolites are microporous crystalline aluminosilicate materials, with alkali or alkaline earth metals as counter ions [4]. As pictorially represented in Figure 2.1, they consist of a framework of $[SiO_4]^{4-}$ and $[AlO_4]^{5-}$ tetrahedra, linked to each other at the corners by sharing their oxygens. This leads to the general formula "$(M^+)_x$ $[(AlO^{2-})_x$ $(SiO_2)_y$] · mH_2O"

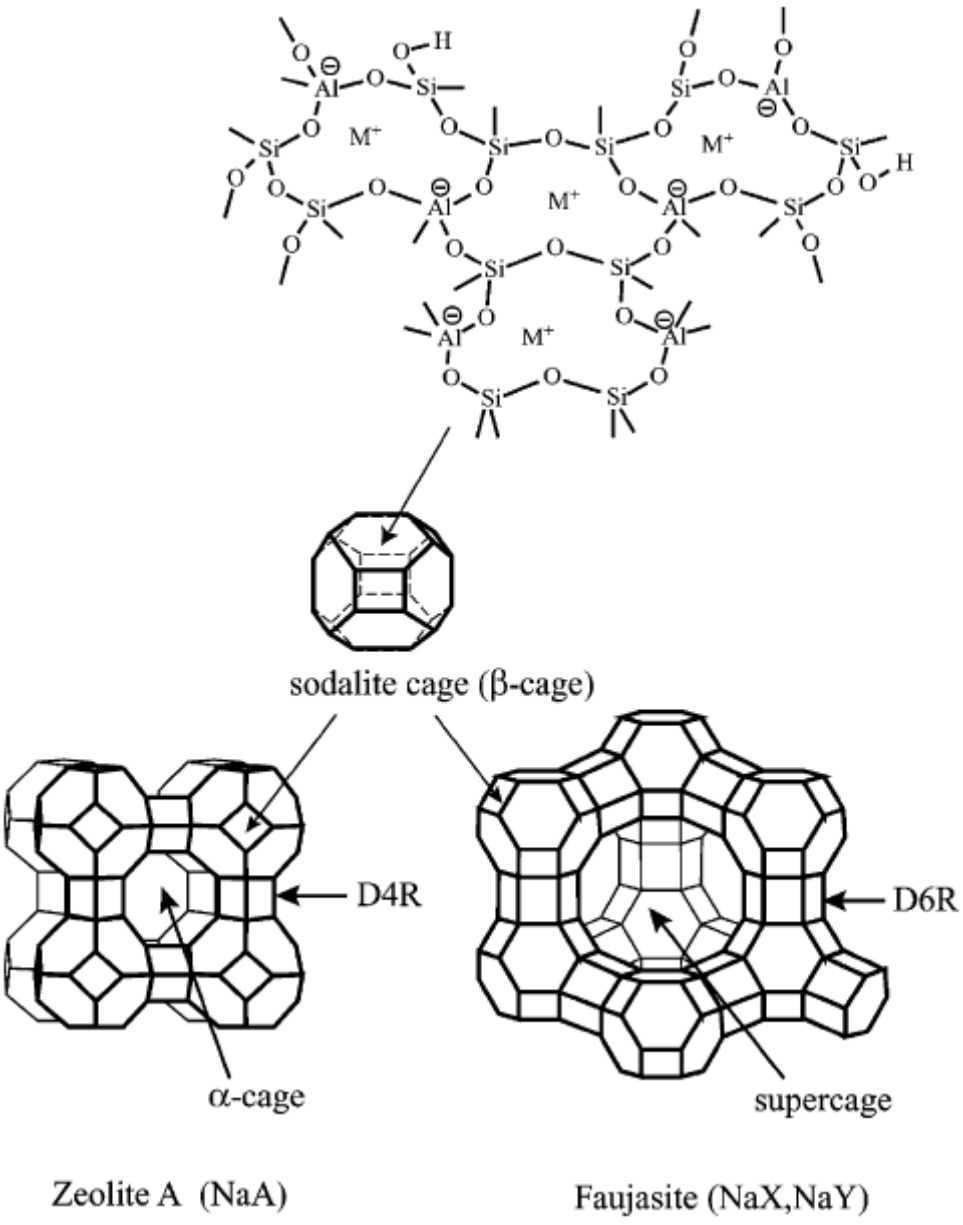

Figure 2.1. Framework structures of sodalite-based zeolites

The cations and water molecules present are located in the cages (cavities) and channels.

Several types of zeolites are frequently employed in photochemical research: their common names are X, Y, A, mordenite, L, ZSM-5, silicalite, MCM-41, to name a few. In the crystallographical classification, X and Y belong to FAU (faujasite), A to LTA, L to LTL, and ZSM-5 and silicalite to MFI. These three-letter framework type codes were assigned by the Structure Commission of the International Zeolite Association. The chemical composition of zeolites is not necessarily limited to the aluminosilicate: aluminophosphate-based zeolites with the $AlPO_4$ lattice and molecular sieves composed of other elements have been synthesized and exhibited catalytic properties distinct from those of aluminosilicate-based zeolites. The structure of faujasite zeolites (zeolites X and Y) is cubic and built from sodalite cages (-cages, 0.66 nm in diameter, with an entry aperture of 0.21 nm) connected via the double 6-membered ring (D6R) frame. Note that the entry aperture of the sodalite cage is too small for the oxygen molecule to enter; however, water molecules are known to go in. Zeolites X and Y have different framework Si/Al ratios: $1.0 < Si/Al < 1.5$ for zeolite X and $1.5 < Si/Al < 3$ for zeolite Y. Interestingly, no faujasite with Si/Al ratio of less than 1.0 has been prepared to date because of the unstable framework structure (Lowenstein's rule). These zeolites form a three-dimensional network of nearly spherical supercages of about 1.3 nm in diameter connected tetrahedrally through 0.74 nm windows (diamond lattice). The supercage concentration in zeolite Y, with Na^+ ions as the charge-compensating cation (Na^+-Y) is estimated to be approximately 6×10^{-4} mol/g on the basis of the crystal structure (Figure 2.2). The charge-compensating cations are mobile and distributed among several types of sites: SI (both in X and Y) in the center of the D6R cage, SI (both in X and Y) inside the sodalite cage, SII (both in X and Y) on top of the hexagonal faces of the sodalite cages facing into the supercage and SIII (only in X) on the four-ring on the supercage wall. Only cations at SII and SIII are accessible to the organic molecules adsorbed within a supercage. A de-aluminated zeolite can be prepared through various post-synthesis modifications. Ultra-stable zeolite Y (USY), for example, de-aluminated by hydrothermal treatment and subsequent extraction of the extra-framework aluminum, has fewer charge-neutralizing cations, resulting from the decrease in the aluminium content and consequently provides less polar environment in supercage networks than Al-containing zeolites do. Zeolite A is a synthetic material, the structure of

which is also composed of sodalite cages similar to faujasite but connected through double 4-membered ring (D4R) of $[SiO_4]^{4-}$ and $[AlO_4]^{5-}$ as shown in the Figure 2.1. By this connection, three cages are present: D4R, sodalite cage and α-cage (1.1 nm in diameter with a 0.41 nm opening). The structure of zeolite A is also cubic, having a Si/Al ratio of 1.0, with alternating Si and Al atoms in the framework.

On the other hand, the channel system in mordenite is a one-dimensional 12-membered ring system with an opening of 0.65 nm×0.70 nm. Of other channel-type zeolites, zeolite L has a unidimensional channel system as in the mordenite, formed by 6- and 4-membered rings (Figure 2.2). The main channels of zeolite L are made by the stacking of sections with a length of 0.75 nm in the c-direction. The sections are joined by shared 12-membered ring windows having a free diameter of 0.71 nm. These rings make up the narrowest parts of the main channel. The largest free diameter is about 1.3 nm and lies midway between the 12-membered rings. In zeolite L, five positions are found for the extra-framework cations, i.e. sites A, B, C, D and E. Only the cations in site D are exchangeable at room temperature. Additionally, the synthesis of mesoporous (extra-large-pore) channel-type aluminosilicates, which allow the inclusion of molecules larger than that possible with faujasite zeolites, has been reported recently. The crystalline aluminosilicate MCM-41 is formed from an array of parallel hexagonal channels whose diameter can be controlled from 2.0 to 6.0 nm by varying a template during its synthesis. These zeolites present an interesting contrast in topology, as well as in the sizes of pores or channels and of their openings from an entrapment point of view, adsorbing molecules inside the zeolites in a size-selective, shape-selective manner.

Pentasil (5-membered ring) units as building blocks, in contrast to the sodalites, constitute channel-type zeolites such as ZSM-5 and mordenite. ZSM-5 and its high-silica analogue silicalite possess a structure consisting of two intersecting channel systems, with the vertical channel being elliptical (0.57 nm × 0.51 nm), whereas the horizontal channels have nearly circular 0.54 nm × 0.56 nm openings as shown in the Figure 2.3 [1]. ZSM-5 zeolites, with highly ordered micropores, surface acidity and ion-exchange capacities are one of the most widely applied inorganic materials as catalyst supports, adsorbents and

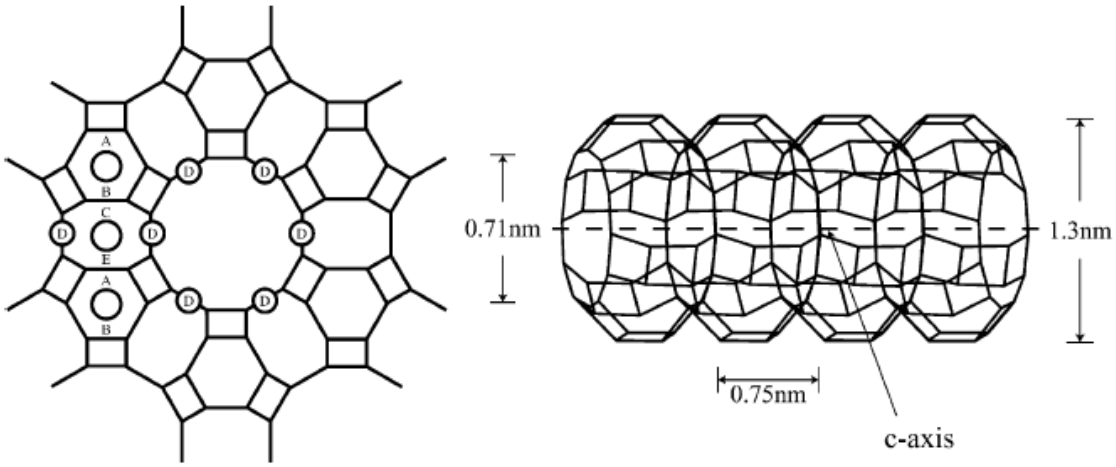

Figure 2.2. Framework structure of zeolite L

molecular-sized spaces for various chemical or photochemical reactions. Highly siliceous ZSM-5 zeolites with low Al_2O_3 content are known to have highly hydrophobic surfaces [5].

Zeolite can be regarded as a solvent that dissolves or disperses molecules into pores and channels, similar to solvent cages [1]. The solvation-like interaction can be expected for zeolites host–guest molecule pairs, and the negatively charged framework and the mobile cations combine to produce an electrostatic field similar to solvent polarity inside the cavities where the molecules reside. The electrostatic field strength (polarity) in zeolites has been suggested to be extremely high and is considered to be due to the fact that the cations exposed at the center of the supercage being only partially shielded. The electric field strength is dependent both on cation size and on Si/Al ratio. For example, the small Li^+ ion induces a stronger field in its proximity than the larger Cs^+ ion. Also, cations in zeolite Y exhibit higher fields than those in zeolite X. The effects of the fields, being similar to those of solvent polarity, have been explored with a number of fluorescence probes incorporated into zeolites. Despite the similarity of zeolite pores to solvent shells, zeolite pores are rigid and distinctly shaped, in contrast to the soft and featureless solvent shells. Examination of physical and chemical properties characteristic to the zeolite is appropriate to gain some insight into the active role of the host material.

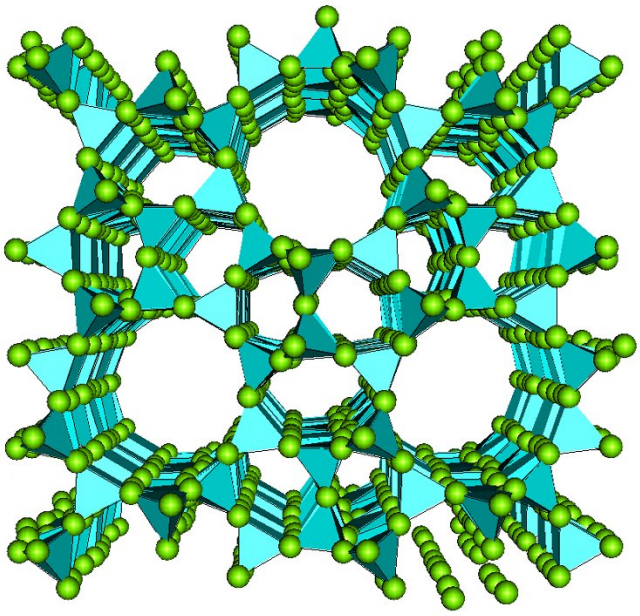

Figure 2.3. Structure of ZSM-5

Zeolites have amphoteric properties and the existence of acid and base sites presented in Figure 2.4 [6]. The bridging Si–OH · · · Al group is usually referred to as a Brønsted acid site in zeolites. On the contrary, no basic framework OH group has been reported to exist. Zeolites contain Lewis as well as Brønsted acid sites. The three-coordinated aluminium sites on the framework and non-framework Al sites are normally considered to be Lewis sites. Additionally, charge-compensating cations act as Lewis acids, while the framework oxygens represent a base. In particular, the oxygens adjacent to Al (Si–O–Al oxygens) are more basic because of a larger negative charge on oxygen. The Lewis acidity is usually connected to an electron accepting property and the basicity to an electron-donating property. Thus, the zeolites behave both as electron donors and as acceptors of moderate strength to the guest species, depending on the adsorption site.

As a rule, the acid strength or the electron-accepting ability increases with increasing Si/Al ratio and for zeolites with smaller alkali metal cations. For example, Li^{+}-Y is more acidic than Cs^{+}-X. On the other hand, the basic strength (electron-donating ability) of the zeolites increases with decreasing Si/Al ratio and for zeolites with larger alkali metal

cations. In this regard, Cs^+-X is more basic than Li^+-Y. Accordingly, the chemical properties of the zeolites can be fine-tuned in terms of composition, cations and framework structure [7].

The range of Si/Al ratios varies a great deal between different zeolites. ZSM-5 can only tolerate low levels of aluminium substitution and an almost purely siliceous version of the structure can be synthesized. Zeolite X/Y can be prepared by Si/Al ratios varying from close to infinity to 1; the lower ratios correspond to "X" and the higher to "Y". Zeolite A is normally obtained with a Si/Al ratio close to unity and a fully ordered Si-Al distribution of the tetrahedral sites, in accordance with Lowenstein's rule.

The incorporation of aluminium into the structure has other major consequences. First the replacement of silicon by aluminium results in a net negative charge for the framework. This can be neutralize by protons which it is generally accepted are firmly bonded to the lone pairs of the bridging oxygen species. These acidic hydroxyl groups play a vital role in the catalytic activity of zeolites. Other acid sites present a defect or surface cations, monovalent, divalent, or trivalent, may be incorporated into extra framework sites. Generally these are in some well-defined location with respect to the framework. The sites S_1 are within the hexagonal prisms created on linking the six-rings of the neighboring the sodalite cages; the $S_{1'}$ are adjacent to the same six rings but project into the sodalite cages.

The S_2 sites are next to non-linking six-rings and project out into the supercage; the $S_{2'}$ sites are next to the same ring and again project into the sodalite unit. Other, less frequently occupied, sites (S_3) are adjacent to four-rings. The second consequence of the inclusion of aluminium in the zeolite framework is that the materials become hydrophilic. Indeed, as normally prepared the materials are extensively hydrated. Some of this water can be ascribed to hydration of the extra framework cations. But additional molecules may be loosely bonded to the framework.

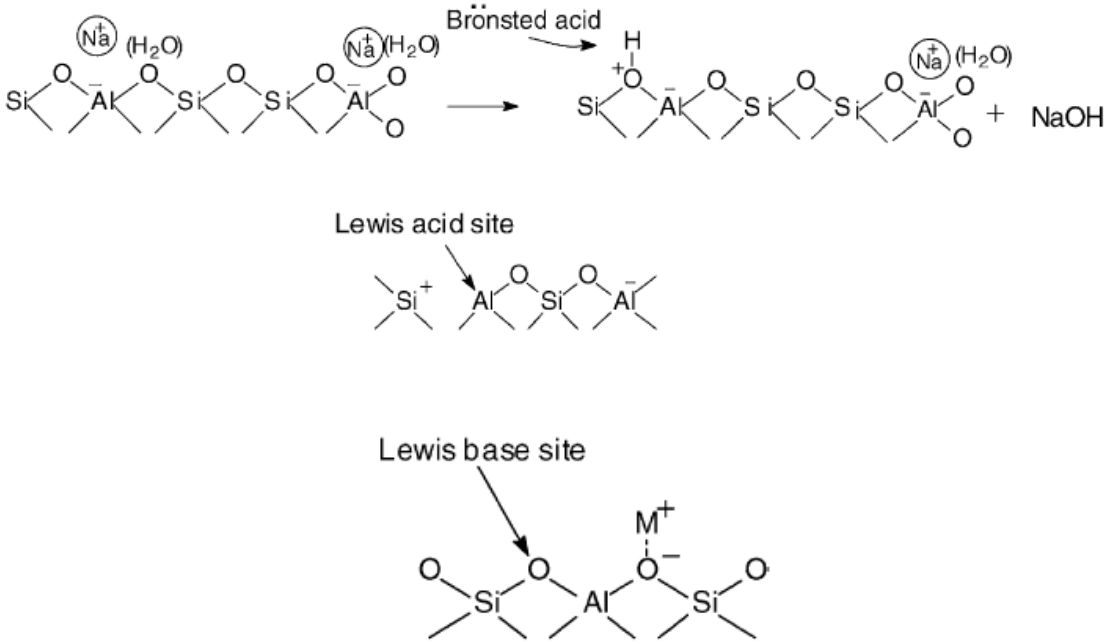

Figure 2.4. Acidic and basic sites in the structure of zeolites

Many other types of atom can be substituted into zeolite frameworks. A wide range of gallo silicates have been synthesized; but transition metal atoms such as titanium and iron have also been successfully introduced at tetrahedral sites, often with interesting and important consequences for the catalytic behavior of materials [8].

2.1.2. Reaction Mechanism

Brønsted acid mechanisms are most important in zeolite catalysis [8]. Bridging hydroxyl groups are the commonest type acid site. These may be considered as protonated oxygens, the protons being present as charge compensator for the negatively charged framework aluminium. The columbic interaction between the tetrahedral aluminium and the protons means that Si-OH-Al bridges provide the dominant type acid species although acid sites associated with defects are thought to contribute to catalytic processes. Brønsted acid catalysis within the zeolites is essentially conventional. The acidic hydroxyl groups protonate unsaturated organic molecules, or basic groups such as OH^- and NH_2. The fate of the protonated species may, however, depend on other acid-base properties of zeolite,

including Lewis acidity and basicity of the framework oxygen ions. Moreover, the nature of the product is controlled by the structure of zeolite pores. A simple but important example is the catalytic conversion of metaxylene to paraxylene. The isomers can be interconverted by acid catalysis. However, if the isomerization is undertaken within the pores of zeolite ZSM-5 the para isomer has a much higher diffusion coefficient as, unlike metaxylene, it can be migrate along the pores of this zeolite. It thus diffuses rapidly out of the catalyst, which therefore effects the required isomerization with high yield. Lewis acidity is known to be important in zeolites. Indeed it has been speculated that it plays an important role in hydrocarbon cracking reactions. Fluid bed catalytic cracking which employs zeolite Y and in which the heavy components of the crude oil are broken down into hydrocarbons in the gasoline range remains single most important application of zeolites. Although the technology of this complex process is well developed, our understanding the reaction pathway is far from complete. The process of coking, whereby the pores of the zeolite become blocked with carbon, is also poorly understood and there is a clear need for better knowledge at the atomic level of the reaction mechanisms involved.

Despite the dominance of acidic catalysis it has been argued that the basic properties may also be of importance to zeolites. Indeed it has been suggested that basic reactions play an important role in the methanol to gasoline conversion affected by ZSM-5, a suggestion that has received some support from quantum mechanical calculations [9]. It is clear that the possibility of basic in addition to acidic reactions in zeolites confers an extra degree of flexibility to zeolite catalysis.

The range of zeolite catalysis is further extended by the possibility of incorporating metal atoms both within the zeolite framework and at extra framework sites. In some cases it is uncertain which type of site will be occupied by a substituent. But in general, small high valence ions such as Ti^{4+}occupy T sites in the framework, while large low-valence ions, e.g. Ca^{2+} occupy extra framework positions. The case of titanium substitution is particularly opposite as appreciable concentrations of Ti can be incorporated in ZSM-5, thereby conferring valuable catalytic properties, in particular with oxidations involving hydrogen peroxide.

New types of catalytic reaction can also be induced by organometallic species created, for example, by carbonylation or by metallic species created by reduction of zeolites containing extra framework transition metal ions such as Ni^{2+} or Pt^{2+}. Indeed it is likely to be increasingly possible to "fine tune" the catalytic properties of metal cations and particles within zeolites, leading to a growing range of applications to the synthesis of organic fine chemicals.

In summary, zeolites can promote a very diverse range of catalytic reactions, including acid-base and metal atom and metal particle induced reactions. The occurrence of such reactions within the pores of the zeolite allows a unique degree of product control [8].

2.2. Titanium Dioxide

Titanium was discovered as a metal in 1791 in England by Reverend William Gregor. It occurs primarily in minerals like rutile, anatase, brookite, and it is found in titanates and many iron ores [10].

Titanium dioxide (TiO_2) belongs to the family of transition metal oxides. In the beginning of the 20th century, industrial production started with titanium dioxide replacing toxic lead oxides as pigments for white paint. The consumption of TiO_2 as a pigment increased in the last few years in a number of sectors such as textiles, food, leather, pharmaceuticals (tablet coatings, toothpastes, and as a UV absorber in sunscreen cream with high sun protection factors and other cosmetic products [11,12].

2.2.1. Titanium Dioxide as a Semiconductor

A semiconductor is a material which has a band structure, characterized as a series of energetically closed spaced energy levels (valence band) and a second series of energetically similar levels lying at a higher energy (conduction band). Its band gap energy (E_{bg}) for electronic excitation lies between zero and about 3 electron volts [13]. Under light irradiation with energy larger than the band gap energy of semiconductors, an electron is excited from the valence band to the conduction band, leaving a hole. Electrons formed in the conduction band and the holes formed in the valence band in this way work as powerful reductants and oxidants, respectively [14].

The most widely known photocatalysts are TiO_2, ZnO and CdS. Due to its highest activity, titanium dioxide is used in photocatalytic measurements. Both CdS and ZnO suffer from corrosion and show lower photoactivity than TiO_2.

Degussa P25 TiO_2 which becomes a standard in photocatalytic studies is reported to have a high photocatalytic activity, which is due to the mixed phase of anatase and rutile in P25 promoting charge-pair separation and inhibiting recombination [15]. A semiconductor photocatalyst should be chemically and biologically inert, stable, easy to produce and to use, efficiently activated by sunlight, cheap, and without risks for the environment or humans [16]. Fine TiO_2 semiconductor nanoparticles are ideal photocatalysts due to their chemical stability, nontoxicity, and high photocatalytic reactivity in the elimination of pollutants in air and water. TiO_2 semiconductor photocatalysts have the potential to oxidize a wide range of organic compounds, into harm-less compounds such as CO_2 and H_2O by irradiation with UV light.

TiO_2 semiconductors have a relatively large band gap of 3.2 eV, corresponding to wavelengths shorter than 388 nm. In other words, TiO_2 in itself can make use of only 3–

4% of the solar energy that reaches the earth, necessitating a UV light source for its use as a photocatalyst.

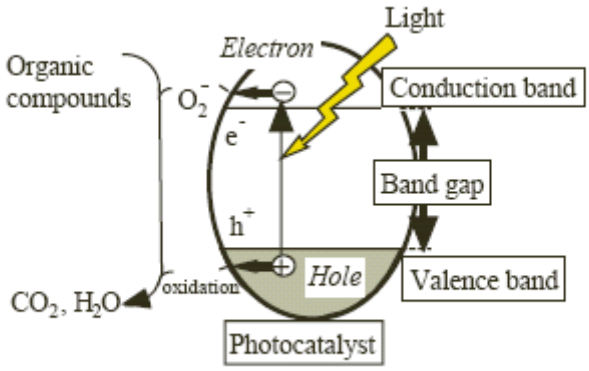

Figure 2.5. TiO_2-sensitized photooxidiative mineralization of organic compounds

Continuous band-gap irradiation of an aqueous TiO_2 dispersion excites an electron from the valence band (VB) to the conduction band (CB), creating an electron-hole pair. The heterogeneous photocatalytic process takes place through a complex sequence of reactions that can be expressed by the fallowing set of equations:

$$TiO_2 + h\nu\ (UV) \rightarrow TiO_2\ (e^-_{CB} + h^+_{VB}) \tag{4.2}$$

The formation of redox pair could either be followed by respective reaction resulting in the dissipation of the reactive species:

$$TiO_2\ (h^+_{VB}) + HO_{2\,ads} \rightarrow TiO_2 + HO^{\bullet}_{ads} + H^+ \tag{4.3}$$

$$TiO_2\ (h^+_{VB}) + HO^-_{ads} \rightarrow TiO_2 + HO_{ads} \tag{4.4}$$

$$TiO_2\ (e^-_{CB}) + O_{2\,ads} + H^+ \rightarrow TiO_2 + HO_2 \tag{4.5}$$

$$H_2O_2 + O_2^- \rightarrow HO\cdot + O_2 + HO^- \tag{4.6}$$

$$TiO_2\ (e^-_{CB}) + H_2O_2 \rightarrow HO^- + HO^{\bullet} \tag{4.7}$$

$$HO^{\bullet}_{ads} + D_{ads} \rightarrow D_{ox} \tag{4.8}$$

$$HO_2^{\cdot} + D_{ads} \rightarrow D_{ox} \tag{4.9}$$

where D represents a dye molecule. Thus, $HO^{\cdot}$ and $HO_2^{\cdot}$ produced in the above reaction series are responsible from the oxidation of organic compounds.

2.2.2. Factors Affecting Surface and Morphological Aspects in TiO_2 Photocatalysis

2.2.2.1. Surface Area of TiO_2. A large surface area can be the determining factor in certain photodegradation reactions, as a large amount of adsorbed organic molecules promotes the reaction rate. However, powders with a large surface area are usually associated with large amounts of crystalline defects, which favour the recombination of electrons and holes leading to a poor photoactivity [10].

The widely used isotherm dealing with multilayer adsorption was derived from by Stephan Brunauer, Pul Emmit and Edward Teller, and is called the BET isotherm. BET isotherms rise indefinitely as the pressure is increased because there is no limit to the amount of material that may condense when multilayer coverage may occur. A BET isotherm is not accurate at all pressure values, but used in indusrty to determine the surface areas of solids [17].

2.2.2.2. Particle Size of TiO_2. Particle size is an important parameter for photocatalytic efficiency, since the predominant way of electron–hole recombination may be different depending on the particle size. It is well known that in the nanometer-size range, physical and chemical properties of semiconductors are modified (compared with bulk). Small variations in particle diameters lead to great modifications in the surface/bulk ratio, thus modifying the significance of volume and surface electron–hole recombination. Experimental investigations support the existence of an optimum particle size of TiO_2, where photocatalytic oxidation rates of organic substrates are maximized. According to some literature data, this value lies around 10 nm, although other authors claim improved activity for particles below such value [10]. Theoretical investigations, via mathematical models, have also concluded that particle size plays a significant role in the photoactivity

of TiO_2. A model based on the mechanism of TiO_2 photocatalysis predicts an increase of the quantum yield when particle sizes decrease from 1000 to 10 nm. It supposes a higher fraction of electron–hole pairs taking part in redox reactions at the surface when fewer electron– hole pairs are generated in the particle.

The average particle sizes are determined from the Scherrer's equation (Equation 4.10) using the broadening of the (101) anatase reflection with the usual assumption of spherical crystallites [18].

$$D = \frac{A\lambda}{(B - b)Cos\theta} \tag{4.10}$$

where D is the average particle diameter, A is 0,09 which is a constant value, λ is the wavelength which equals to 0,1542 nm, B is full width half maximum of the corresponding diffraction peak and θ is the diffraction peak angle.

2.2.2.3. Sol-gel Method: Preparation of Nano-sized TiO_2 Particles. These methods are used for the synthesis of thin films, powders, and membranes. Two types are known: the non-alkoxide and the alkoxide route. The sol–gel method has many advantages over other fabrication techniques such as purity, homogeneity, felicity, and flexibility in introducing dopants in large concentrations, stochiometry control, ease of processing, control over the composition, and the ability to coat large and complex areas. The non-alkoxide route uses inorganic salts (such as nitrates, chlorides, acetates, carbonates, acetylacetonates, etc.), which requires an additional removal of the inorganic anion; while the alkoxide route (the most employed) uses metal alkoxides as starting material [10,19]. This method involves the formation of a TiO_2 sol or gel or precipitation by hydrolysis and condensation (with polymer formation) of titanium alkoxides. Acetic acid may be used in order to initiate hydrolysis via an esterification reaction, and alcoholic sols prepared from titanium alkoxide using amino alcohols have been shown to stabilize the sol, reducing or preventing the condensation and the precipitation of titania [20]. These reactions are followed by a

thermal treatment (450–600 ^{o}C) to remove the organic part and to crystallize either anatase or rutile TiO_2.

2.2.3. Support

There are certain limitations of using bare TiO_2 in photocatalytic reactors. For example, due to small size (about 4–30 nm) TiO_2 aggregates rapidly in a suspension loosing its effective surface area as well as the catalytic efficiency. Being on-porous, TiO_2 exhibits low adsorption ability for the pollutants, especially for the non-polar organic compounds due to its polar surface. Immobilizing TiO_2 on substrates such as glass matrix, optical fiber and stainless steel plate eliminates the problem of agglomeration, although the photocatalytic efficiency of immobilized TiO_2 is less than the suspended TiO_2 particles. Besides, the specific surface area also decreases due to the fixing of the TiO_2 non non-porous supports reducing the adsorption capacity. For photocatalytic decomposition of a target compound, adsorption of it on the TiO_2 surface is essential prior to the surface reaction. Furthermore organic pollutants generally occur in low concentrations (ppm level or below) and pre-concentration of the substrates on the surface where photons are adsorbed is a desirable feature for effective photodegradation. In recent years, attempts have been made to support fine TiO_2 on porous adsorbent materials like silica, alumina, activated carbon, clay and zeolites. TiO_2 supported on these types of adsorbents provide higher specific surface area and facilitate more effective adsorption sites than bare TiO_2. The enhanced decomposition rates are attributed to;

- an enhanced concentration of substrate compounds is progressively built up around the TiO_2 sites, leading to a significant increase of the reaction rate;
- an advanced degradation of the pollutant succeeding their mineralization in the case where this was not achieved with bare TiO_2, was due to the fact the reaction intermediates are also adsorbed and then further oxidized. So, toxic intermediates, if formed, are not released in air or in solution, thereby preventing secondary pollution by intermediates if any;
- the possibility of photodestruction of low levels of pollutants (either in water decontamination or indoor applications);

- the continued use of the photocatalyst without deactivation, since the adsorbed substances are oxidized finally to CO_2 [21].

2.2.4. Metal Incorporation

Doping with metal ions has been proven to be a potential route for the improvement of photoactivity of TiO_2 and enhanced photoactivity has been observed by transition metal ion doping. Due to the fact that doping ions act as trapping sites, they can influence the lifetime of charge carriers. Usually, they enhance the recombination of photogenerated electrons and holes, and therefore do not allow reactions to proceed with any noticeable effect under either ultraviolet or visible light. P-Type doping is obtained by dissolving heterocations of valencies lower than that of Ti^{4+} (Al^{3+}, Cr^{3+}, Ga^{3+}, Ln^{3+}) in the TiO_2 lattice, while n-type doping is obtained by heterocations of valencies higher than Ti^{+4} (Nb^{5+}, Ta^{5+}, Sb^{5+}). The inhibition effect is ascribed to an increase in the electron–hole recombination rate. More precisely, p-type dopants act as acceptor centers, which trap photoelectrons and, once negatively charged, attract holes, thus forming recombination centers [22,23].

On the opposite, n-type dopants act as donor centers. By increasing the concentration of conduction electrons, they also favor the electron–hole recombination, which is detrimental for the photoefficiency [24]. Fe^{3+}, Ru^{3+}, Os^{3+}, and Gd^{3+} represent a special position between the metallic dopants. These four metal ions have a half-filled electronic configuration (d5 and f7) that is known to be more stable. When these metallic ions trap electrons, the half-filled electronic configuration is destroyed and their stability decreases. The trapped electrons can easily be transferred to oxygen adsorbed on the surface of the catalyst and the metallic ions return to the original stable half-filled electron structure. This might promote charge transfer and efficient separation of the electrons and holes by shallow trapped electrons. The prerequisite for an effective dopant involves the possibility of charge detrapping and migration to the surface. Codoping may represent a viable way to improve the charge separation. Nanocrystalline TiO_2 codoped with Eu^{3+} and

Fe^{3+} in an optimal concentration shows a co-operative (synergetic) effect, which significantly increases the photocatalytic degradation of chloroform in solution (five times compared to pure nanocrystalline TiO_2 and about two to six times compared to Fe^{3+} or Er^{3+} doped separately, respectively). Fe^{3+} serves as a hole trap and Eu^{3+} as an electron trap, speeding up the anodic and the cathodic processes, respectively, via improved interfacial charge transfer [10].

Rare earth metal compounds especially their oxides have become of increasing interest in recent years because of their special photoluminescence and catalytic properties. Lanthanide ions are known for their ability to form complexes with various Lewis bases in the interaction of these functional groups with the f-orbitals of lanthanides. It is expected that incorporation of lanthanide ions into a TiO_2 matrix could provide a means to concentrate the organic pollutant at the semiconductor surface and therefore enhance the photoactivity of TiO_2 [25].

There is an optimum loading value above which metal deposition has a detrimental effect on the photocatalytic activity. The existence of this optimum loading value may have different reasons. For metal loadings above optimum values, a decrease in electron density occurs, due to electron attraction by numerous metal particles. The resulting complicated field configuration has a detrimental effect on the charge separation, lowering the photocatalytic activity of the catalyst. Also, excessive coverage of TiO_2 catalyst limits the amount of light reaching the surface, reducing the number of photogenerated hole–electron and lowering consequently the photodegradation rate [10]. Di Paola et al [24], have confirmed that the addition of transition metals to TiO_2 is generally detrimental for the photooxidation of organic compounds in aqueous solutions. In their work only samples containing 1 per cent of loading metal have been studied because, for other photoreactions, only a few samples containing between ca. 1 and 2 per cent of transition metal ions have shown photoactivity higher than that of the bare support. Higher amounts of metal species can give rise to a full coverage of the surface of TiO_2, thus hindering the photoexcitation of the semiconductor whilst lower metal amounts are not generally more beneficial as well. Lastly, once negatively charged, metal particles, especially for highly loaded samples (>5

at. per cent), attract holes and subsequently recombine them with electrons. In this case, the metal deposits become recombination centers [10].

2.3. Literature Survey

Xu and Langford [26] investigated the photocatalytic activity of TiO_2 supported on ZSM-5, zeolite A, silicate, and alumina using the photooxidation of 4-chlorophenol and acetonephenone. X-ray diffraction (XRD), infrared (FTIR), scanning electron microscopy (SEM) and BET surface area analysis were performed to characterize the prepared catalysts. Results indicated that the structure of zeolite plays an important role in photoactivity enhancement of the zeolite supported oxides and high activity of low titania loading implies favorable light collection and efficient access to photoactive sites or species. It was found that the photocatalytic activity of TiO_2 on ZSM-5 and zeolite A was higher than that of a TiO_2 powder or TiO_2 formed on silica and alumina**.** Also, TiO_2-ZSM-5 showed the highest photoactivity at low Ti content which has large adsorptivity for the organic substrates.

Yang and Long [27] carried out the study of ion-exchanged pillared clays (PILCs) as catalyst for selective reduction of NO by ethylene. Three important pillared clays Al_2O_3-PILC, ZrO_2-PILC and TiO_2-PILC were synthesized. Selective catalytic reduction activities by cation exchanged pillared clays were compared directly with that of Cu-ZSM-5. Characterization was carried out by BET surface area and X-ray diffraction (XRD). The most active PILC catalyst was found to be Cu-exchanged TiO_2-pillared clay and Cu-exchanged Al_2O_3-pillared clay.

The photocatalytic activities of the mixtures of TiO_2 (P25) with three rare earth oxides were studied by Lin and Yu [28]. The effects of the rare earth oxide contents and calcination temperature on the photocatalytic activities were studied. The results reveal that the mixtures of TiO_2 with La_2O_3 (0.5 wt %) or Y_2O_3 (0.5wt %) calcined at 700^oC or

650^{o}C exhibit higher photoactivity than pure TiO_2 (P25) for the oxidation of acetone. Experimental results of polycrystalline X-ray diffraction (XRD), photoexcited transient absorption decay and zeta potential measurements showed that the presence of these rare earth oxides can inhibit anatase to rutile transformation at elevated temperatures which means that anatase-rutile transformation is somehow inhibited in the mixtures.

Pal et al [29] investigated the preparation of binary mixed oxide of Fe/Ti with homogenous distribution of iron into the TiO_2 by sol-gel impregnation method. X-ray diffraction (XRD), Frourier infrared spectroscopy (FT-IR), scanning electron microscopy (SEM), and transmission electron microscopy (TEM) analysis were performed to characterize each sample. Results indicated that the mixed oxides always contain rutile phase and pseudobrookite phase at higher firing temperatures and mixture of anatase and rutile formed at low sintering temperature, when samples are prepared by impregnation method. And the photocatalytic efficiency of Fe/Ti oxide for the degradation of O-Cresol is strongly depended on the phase composition and sintering temperature of the samples.
In 1999, Chen et al [30], studied the modification of zeolites with TiO_2 via a complex method comprising partial ion-exchange and impregnation in a low concentration of $(NH_4)_2Ti0(C_20_4)_2$ aqueous solution. The change in porosity of zeolite by TiO_2 modification was shown by using N_2 adsorption measurement. Results showed that the photochemical activity of TiO_2 in the TiO_2-zeolite system to decompose ethanol was more than five times that in the bulk system.

In 2001, in the study of Kim and Yoon [31], the adsorption of p-N,N'-dimethylaminobenzoic acid (DMABA) onto nanoscale pores of TiO_2/Y-zeolite and its spectroscopic properties have been studied and methyl orange selected as the probe molecule. UV-Vis, infrared (IR) and diffuse reflectance spectroscopies were performed to characterize each catalyst. Results showed that p-N,N'-dimethylaminobenzoic acid can be entrapped into the nanopores of TiO_2/Y-zeolite, playing an important role in enhancement of electron density on the conduction band of TiO_2 on the zeolite frame to enhance the photocatalytic activity of TiO_2/Y-zeolite for the reduction of organic compounds in water. Irradiation of TiO_2 on TiO_2/Y-zeolite by UV light, the conduction band electron can be

removed quickly from the TiO_2 site before charge recombination because the electron rich zeolite surface acts as a hole scavenger.

Zhang et al [32], carried out the preparation of mesaporous nanocrystalline titanium dioxide with narrow pore size distribution by a sol-gel technique. Butanediol mixed with tetrapropylorthotitanate was used as precursors. The aging time for the synthesis has an evident influence on the phase transition of TiO_2 and the nucleation process. A very fine network texture made from uniform nanoparticles was revealed by scanning electron microscopy (SEM) and transmission electron microscopy (TEM) analyses whose results indicated that aging time influences the phase transition and nucleation of the final products. With the increasing of the calcination temperature, the intensity of the anatase peaks became stronger and well-resolved, indicating that larger size particles are formed. When the calcination temperature continues to be increased, small rutile peaks were found, showing the beginning of the phase transformation of anatase to rutile. Results also showed that increasing the aging time decreases the anatase-rutile transformation temperature.

Durgakumari et al [33], studied the TiO_2 sample supported over HY, HZSM-5 and Hβ zeolites using various precursors like TiO_2 (Degussa P25), titanium isopropoxide for the photocatalytic degradation of aqueous phenol and p-chlorophenol. Characterization was carried out by X-ray diffraction (XRD), scanning electron microscopy (SEM) and BET surface area (N_2 adsorption). It may be seen from the results that combination of titania and HZSM-5 is working well in enhancing the photodegradation of pollutant. HZSM-5 is playing a role in pooling the pollutant molecules and thus facilitating the photodegradation activity on TiO_2 where it is totally free from interaction.

In the study of Anpo et al [5], the metal ion-implanted TiO_2 catalysts which were effective for various photocatalytic reactions were studied. Metal ion-implanted TiO_2 catalysts were found to be enabling the absorption of visible light up to wavelength of 400-600 nm. They successfully applied the metal ion-implantation method to modify the

electronic properties of the TiO_2 catalyst enabling the absorption of visible light even longer than 550 nm and initiating the photocatalytic reactions not only under UV but also under visible light irradiation. Characterization was carried out by UV-Vis spectroscopy and results showed that transition metal ion-implanted TiO_2 catalyst has several times higher efficiency than the un-implanted pure TiO_2 catalyst.

Francisco and Mastelaro [34] investigated the addition and effects of CeO_2 and CuO into TiO_2 lattice. Characterization was carried out by BET surface area, X-ray diffraction (XRD), and Raman analysis. It was found that the anatase-rutile phase transformation of titania was accelerated by CuO. However, the addition of CeO_2 to the CuO-TiO_2 inhibited the phase transformation; stabilize the anatase phase by surrounding the rare earth oxides through the formation of Ti-O-rare earth element bonds.

Zhang et al [35], carried out the Fe-doped TiO_2 because of its photocatalytic a property which is employed in devices for water detoxification, water splitting and air purification. Iron concentration of each sample varies between 0.2 % and 30 %. Transmission electron microscopy (TEM), BET surface area, energy dispersive X-ray analysis (EDX) and X-ray diffraction (XRD) results showed that for iron concentration less than 0.2 %, the temperature of the phase transition from anatase to rutile structure increases with increasing iron concentration. Above this concentration, the transition temperature remains approximately 600^oC-650^oC. Samples calcined at temperatures lower than 400^oC, show poor crystalline quality and contain amorphous phases. At low calcinations temperatures, the iron atoms are incorporated into the lattice of the anatase structure for Fe concentrations up to 30 %. In contrast, only up to 0.2 % Fe can be incorporated into rutile TiO_2.

In 2003, the degradation of Rhodamine B by using europium doped nanocrystalline TiO_2 was studied [36]. Lanthanide ions are known for their ability to form complexes with various Lewis bases in the interaction of these functional groups with the f-orbitals of lanthanides. It is expected that incorporation of lanthanide ions into a TiO_2 matrix could

enhance the photoactivity of titania. The rutile phase is observed until the temperature is increased to 1000^{o}C showing a strong inhibition effect for the phase transformation. The precise mechanism for this change is unclear but may be related to the formation of $Eu_2Ti_20_7$ and defects for high europium content samples. Characterization was carried out by X-ray diffraction (XRD) and transmission electron microscopy (TEM). Results indicated that the photoactivity gradually decreased with further increases in europium content and all of the doped materials showed better activity than undoped pure TiO_2 for the degradation of Rhodamine B. In addition, anatase-rutile transformation was postponed to higher calcination temperatures due to the presence of europium.

Noorjan et al [37] determined TiO_2-HZSM-5 combinate thin film as an efficient photocatalyst for the degradation of phenolic wastewaters than thin films without zeolite. Their methods involves the immobilization of performed TiO_2 and TiO_2-HZSM-5 combinate into flexible films by a simple spray technique using acrylic emulsion at ambient temperature. Characterization was performed with X-ray diffraction (XRD), and scanning electron microscopy (SEM) whose results showed that the presence of an adsorbent like HZSM-5 zeolite increases the photoactivity of TiO_2.

In 2004, Anipsitakis and Dionysiou [38], studied the effect of ultraviolet (UV) light radiation and/or transition metals (M) for the activation of common oxidants (Ox) with the objective of treating recalcitrant organic contaminants in water. Hydrogen peroxide, potassium peroxymonosulfate and potassium persulfate were combined with iron, cobalt and silver, respectively, and/or with UV light (254 nm) and were tested for the treatment of 2,4-dichlorophenol. From the combined use of UV, the oxidants and the transition metals, four general categories of advanced oxidation technologies were evaluated and compared for the degradation and mineralization of 2,4-dichlorophenol. Characterization was performed by a UV-Vis spectrometer. Results showed that transformation of 2,4-dichlorophenol and the extent of organic carbon removal led to the construction of the following order of efficiencies: $UV/K_2S_2O_8 > UV/KHSO_5 > UV/H_2O_2$ for the UV/Ox processes and $UV/Fe(III)/ H_2O_2 > UV/Fe(II)/ H_2O_2 > UV/Co(II)/ KHSO_5 > UV/Ag(I)/ K_2S_2O_8$.

The photocatalytic performance of the binary and ternary mixed oxide of Y/Fe/Ti with homogenous distribution of yttrium and iron oxides into TiO_2 were tested for the EDTA model compound [39]. The catalysts were prepared by using sol-gel technique. Characterizations were carried out by X-ray diffraction (XRD), Frourier infrared spectroscopy (FT-IR), scanning electron microscopy (SEM), atomic force microscopy (AFM), X-rays photoelectron spectroscopy (XPS) and BET surface area measurements. Results showed that the mixture of TiO_2/Fe_2O_3 or $Y_2O_3/ Fe_2O_3/ TiO_2$ have higher photocatalytic activity than pure TiO_2 for the oxidation of EDTA.

The novel photocatalytic materials were synthesized by incorporation of TiO_2, a transition metal and heteropolyacid (HPA) in the zeolite structure [40]. These materials were characterized by using X-ray diffraction (XRD), UV-Vis diffuse reflectance spectroscopy and elemental analysis. These materials were evaluated for the photoreduction of methyl orange. Results showed that zeolite Y-TiO_2-Co-HPA showed a better photocatalytic activity compared to zeolite Y-TiO_2-HPA and zeoliteY-TiO_2 indicating the role of transition metal ions which is responsible for the delaying electron-hole recombination reactions.

Liu and Sun [41] prepared Fe_2O_3-CeO_2-TiO_2/γ-Al_2O_3 catalyst by consecutive impregnation method. The characterization of this catalyst was done by using BET, SEM, XRF, XPS and chemical analysis techniques. The degradation of an azodye, methyl orange, in the presence of Fe_2O_3-CeO_2-TiO_2/γ-Al_2O_3 at room temperature and atmospheric pressure was investigated. The degradation pathway of methyl orange was analyzed by using UV–Vis and FT-IR techniques. The results of analysis show that the metal oxides are dispersed equally on the surface of catalyst and Fe exists on the surface of catalyst in the form of Fe_2O_3 and Ce and Ti in the form of complex oxides as Ce_2O_3-TiO_2. All the prepared catalysts exhibit excellent catalytic activity in the catalytic wet air oxidation process under experimental conditions and almost a complete degradation of methyl orange in wastewater can be achieved.

Takeuchi et al [5] prepared the TiO_2 catalyst with ZSM-5 by the impregnation of $(NH_4)_2[TiO(C_2O_4)_2]$ aqueous solution. The highly hydrophobic H-ZSM-5 with low Al_2O_3 content was effective as an adsorbent for acetaldehyde molecules. This study suggests the close relationship between the hyrophobicity of the zeolites and the high photocatalytic reactivity of TiO_2 prepared on zeolites compared with unloaded TiO_2 catalysts on the oxidation of acetaldehyde molecule. With this purpose adsorption of acetaldehyde molecules on H and Na type ZSM-5 zeolites of different SiO_2/ Al_2O_3 ratios (1880, 220, 68, 23.8) were investigated. Results showed that TiO_2 prepared on siliceous H-ZSM-5 showed higher photocatalytic reactivity compared with the commercial TiO_2 catalyst, because the zeolites worked as an affective adsorbent to condense acetaldehyde molecules. The photocatalytic reactivity of TiO_2-H-ZSM-5 was largely dependent on the interaction of the reactants with the adsorption sites of the zeolite. The acetaldehyde molecules interacting with the silanol groups of the hydrophobic H-ZSM-5(1880) can efficiently spill over onto the TiO_2 sites, producing high photocatalytic reactivity. In contrast, the H-ZSM-5(220 and 68) with high Al_2O_3 content do not work as suitable adsorbents for acetaldehyde, resulting in decreased photocatalytic reactivity. Because the acetaldehyde molecules strongly trapped on the Na+ sites of the zeolite could hardly transfer onto the TiO2 sites, TiO2/Na-ZSM-5(23.8) showed no reactivity.

3. EXPERIMENTAL

3.1. Reagents

The zeolite (ZSM-5) used as support in this study was obtained from Across (400 m^2/g surface area, 0.55 nm pore size, 2-5 μm crystal size). The support was characterized by XRD and SEM (EDAX) analysis and the chemical composition of ZSM-5 was found as fallows: 97.57 per cent SiO_2, 1.42 per cent Al_2O_3. Titanium tetrapropoxide ($Ti(OC_3H_7)_4$) (98 per cent Aldrich), lanthanum nitrate ($La(NO_3).6H_2O$) (99 per cent Merck), cerium nitrate ($Ce(NO_3).6H_2O$) (98.5 per cent Merck), yttrium nitrate ($Y(NO_3).6H_2O$) (99 per cent Merck), nitric acid (HNO_3) (65 per cent Merck), amonia (NH_3) (25 per cent Merck), acetic acid (CH_3COOH) (100 per cent Merck) and hydrogen peroxide (H_2O_2) (30 per cent Merck) were used as provided by the suppliers without further purification. Water was purified with an Elga-Pure Water Purification (UHQ II) system.

3.1.1. Methyl Orange

Waste waters produced from textile and other dyestuff industrial processes contain large quantities of organic dyes which are difficult to degrade with standart biological methods [42]. Within the overall category of dyestuffs, azodyes constitute a significant portion. Azodyes are an abundant class of synthetic, colored, organic compounds, which are characterized by the presence of one or more azo bonds (–N=N–). Large quantities of these dyes (about half of the textile dyestuffs) are manufactured worldwide and used in a variety of applications. Such colored dye effluents pose a major threat to the surrounding ecosystems since, apart from the environmental pollution; some of the dyes pose documented health hazards [43]. The toxicity and potentially carcinogenic nature of these substances and their manufacturing precursors represent an increasing danger in aquatic life. Several studies have been conducted on the issues of biological, physical and

chemical treatment of dye-containing effluents. Bio-treatment of azodyes is, in general, ineffective, due to their resistance to aerobic degradation. Furthermore, the azodyes that undergo reductive cleavage through anaerobic biological treatment potentially generate carcinogenic aromatic amines in the process. Physical methods such as flocculation, reverse osmosis, and absorption on activated charcoal are non destructive and merely transfer the pollutants to other media, thus causing secondary pollution. Chemical destruction of dyes may be accomplished using chlorine or ozone. These chemical treatments have yielded encouraging results of color and organics removal, but the required dosages are often too high to be economically feasible [44]. Methyl orange (MeO) is a well known azodye (Figure 3.1 inset). Its structure is also characterized by sulphonic groups, which are responsible for the high solubility of these dyes in water. Besides, methyl orange acts as an acid-base indicator in solution, by exhibiting orange color in basic medium and red in color in acidic medium. When dissolved in water, the UV–Vis (Shimadzu UV-1600) spectrum of methyl orange shows two absorption maxima; first band at 298 nm and a more intense second band at 464 nm (Figure 3.1).

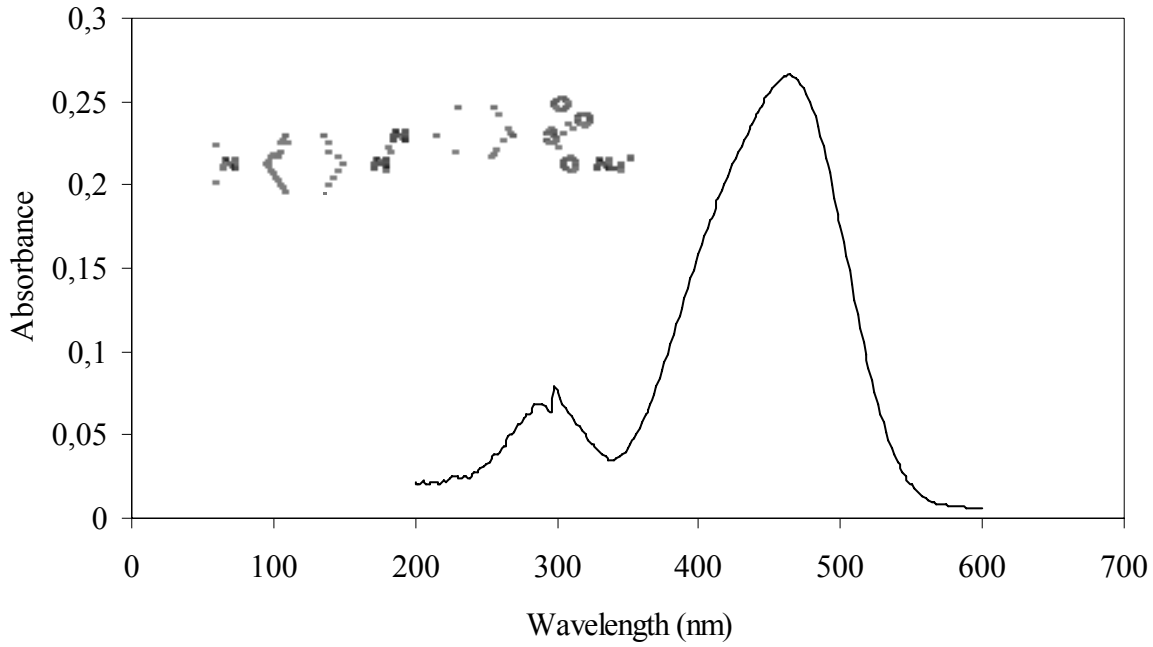

Figure 3.1. Electronic spectrum of methyl orange in aqueous solution.
Inset: Chemical structure of methyl orange

3.2. Preparation of Catalysts

3.2.1. Sol-Gel Method: Preparation of Titania-Sol and Bare TiO_2

Titanium tetrapropoxide ($Ti(OC_3H_7)_4$) (40 mL) was added to acetic acid (CH_3COOH-AcOH) solution of 80 wt per cent. A transparent sol was obtained at the end of 2h mixing at 50^oC.

Titanium tetrapropoxide reacted with the acetic acid and produced a polynuclear species according to equation (3.1).

$$2Ti(OC_3H_7)_4 + 2AcOH \rightarrow Ti_2(OC_3H_7)_6(OAc)_2 + 2C_3H_7OH \quad (3.1)$$

Two octahedral $Ti(OC_3H_7)_3(OAc)$ units linked together by both (OC_3H_7) and (OAc) bridges. Therefore, it is suggested that the reaction of titanium tetrapropoxide with AcOH takes place during the aging process of the titania-sol solution [45,46]. Bare TiO_2 without the support (ZSM-5) was prepared by drying the titania-sol at 100^oC about 12 h. Then, the obtained crystals were washed and centrifuged several times. Finally, the resulting material dried at 100^oC for 12 h and calcined at 400^oC for 12 h. The amount of titania content in the final catalyst was 40 wt per cent, thus the catalysts obtained after the calcination process were named as 40-TiO_2 (100^oC) and 40-TiO_2 (400^oC).

3.2.2. Preparation of TiO_2 Catalyst Supported on ZSM-5

2 g of the support, ZSM-5 was suspended in water about 2 h. Thus the hydrogenated form of ZSM-5 (HZSM-5) was obtained. Depending on the (wt per cent) loading of TiO_2 on the support, requisite amount of titania-sol as 10 wt per cent or 40 wt per cent or 60 wt per cent was added to the aqueous suspension of ZSM-5. The resulting mixed suspension was agitated by magnetic stirrer for 12 h at room temperature, followed by several centrifugations and washings with de-ionized water. The resulting supported TiO_2 catalysts were dried at 100^oC and subjected to calcination for 12 h at 400^oC. Finally the

products were ground into fine powder and stored in dark. The catalysts were hereafter named as, 10-TiO_2-ZSM-5, 40-TiO_2-ZSM-5, and 60-TiO_2-ZSM-5.

Our results indicated that the best photocatalytic degradation of methyl orange by TiO_2 supported catalysts occurred at TiO_2 content of 60 wt per cent. However, for metal ion incorporation (to have free Lewis base sites) and for the adsorption of more methyl orange in all supported catalysts, both adsorption and photodegradation experiments were conducted with a TiO_2 loading of 40 wt per cent, and only those characterization results related to 40 wt per cent TiO_2 loading are presented in this study.

3.2.3. Ion Exchange Process: Metal Incorporation on 40- TiO_2-ZSM-5 Catalyst

$La(NO_3)_3.6H_2O$, $Ce(NO_3)_3.6H_2O$, and $Y(NO_3)_3.6H_2O$ were used as metal-ion precursors. For the ion-exchange process, metal ions were regulated as 0.28 at per cent, 0.5 at per cent, 1.0 at per cent and 3.0 at per cent for cerium, lanthanum and yttrium by solving the requisite amount of metal precursors in water solutions. 1 g of 40-TiO_2-ZSM-5 catalyst was then added to each of these solutions and stirred overnight at room temperature. Then the obtained products were centrifuged at 4000 rpm and washed with de-ionized water several times. The exchange process was repeated four times and the resulting catalysts dried at 100^oC overnight and calcined at 400^oC for about 12 hours. The catalysts are hereafter named as "X" Metal-"Y" TiO_2-ZSM-5, where X represents metal ion content and Y represents TiO_2 content in the resulting materials. The following is the list of all supported catalysts incorporated with metal ions: 0.28 Y-40 TiO_2-ZSM-5, 0.5 Y-40 TiO_2-ZSM-5, 1 Y-40 TiO_2-ZSM-5, 3 Y-40 TiO_2-ZSM-5, 0.28 La-40 TiO_2-ZSM-5, 0.5 La-40 TiO_2-ZSM-5, 1 La-40 TiO_2-ZSM-5, 3 La-40 TiO_2-ZSM-5, 0.28 Ce-40 TiO_2-ZSM-5, 0.5 Ce-40 TiO_2-ZSM-5, 1 Ce-40 TiO_2-ZSM-5, 3 Ce-40 TiO_2-ZSM-5.

3.3. Analysis

3.3.1. Characterization Techniques

The surface morphology of the pure TiO_2 and supported catalysts was obtained by using Scanning Electron Microscopy (SEM) in combination with Energy Dispersive X-ray analysis on an ESEM-FEG/EDAX Philips XL-30 instrument operating at 20 kV using catalyst powders supported on carbon tape.

The X–ray powder diffraction (XRD) patterns of all catalysts were recorded on a Rigaku-D/MAX-Ultima diffractometer using Cu Kα radiation (λ = 1.54 Å) operating at 40 kV and 40 mA and scanning rate of 2^o min^{-1}. The scanning range 2θ=20-70^o was used to determine 40-TiO_2 catalysts prepared at different calcinations temperatures, and the ranges 2θ=0-20^o and 2θ=20-70^o were used to determine all supported catalysts.

The synthesized catalysts were characterized using different analytical techniques. The nitrogen adsorption/desorption isotherm was obtained at liquid nitrogen temperature 77 K by using Quantachrome Nova 2200e automated gas adsorption system. The specific surface area was determined by using multi-point BET plot. The pore size and pore volume were determined by the BJH desorption isotherm.

Microscopic feature of raw ZSM-5, 40-TiO_2-ZSM-5 and all the other metal incorporated catalysts; 0.28 Y-40 TiO_2-ZSM-5, 0.28 La-40 TiO_2-ZSM-5, 0.28 Ce-40 TiO_2-ZSM-5 were obtained by using Atomic Force Microscopy (AFM) at room temperature with an Universal Scanning Probe Microscope (USPM) (Queosent-Ambios Technology, Santa Cruz, CA). Contact mode imaging was performed using silicon nitride cantilever probe with a nominal tip radius of 5-10 nm. The thin films of the catalysts were deposited by dip-coating (KSV-LM) in an aqueous solution containing 0.1 wt per cent of the

catalysts. Glass microscope slides were used as substrates for reference cleaned for 2 h in an ultrasound bath with ethanol and dipped in the precursor solution bath and then pulled out with a constant speed to obtain the films of uniform thickness. The roughness value for the glass slides after the cleaning process was very low. A very thin film of catalysts that formed on the substrate dried in air at room temperature.

3.3.2. Photocatalytic Degradation of Methyl Orange

All experiments of photocatalytic degradation reaction were conducted in a laboratory constructed irradiation box (Figure 3.2). The box was equipped with eight-black light fluorescent lamps (8x15 W) that supply light of wavelength 320-440 nm (Figure 3.3). The incident photon flux for all lamps was measured as 7.8×10^{-9} einstein/s using potassium ferrioxalate actinometer [47]. A fan was placed at the back-side of the box to eliminate any heating effects of the lamps.

Reaction systems were set-up by adding 0.1 g of catalysts into 100 ml of 10 μM methyl orange aqueous solution at room temperature. A pyrex erlenmeyer flask was used for irradiation experiments. The flask has an inlet for the circulation of air and an outlet for the collection of aliquots. Air circulation was supplied by using a Cole-Parmer peristaltic pump. For all experiments, air circulation is regulated as flow rate rate in the conditions part of the figure captions. All connections were made with Tygon tubing. The lamps are positioned to surround the flask from two sides. Prior to photo-oxidation, the suspension with methyl orange and photocatalysts was magnetically stirred in the dark for 30 min to establish an adsorption equilibrium condition. All experiments were performed in continuous circulation mode, aliquots (about 5 ml) were retrieved from the flask-outlet at certain time intervals and analysed after filtering through Millipore filter (0.45 μm). Measuring the characteristic absorption intensity of methyl orange at 464 nm monitored the variation in concentration of methyl orange during the photocatalytic degradation runs.

Figure 3.2. Irradiation Box

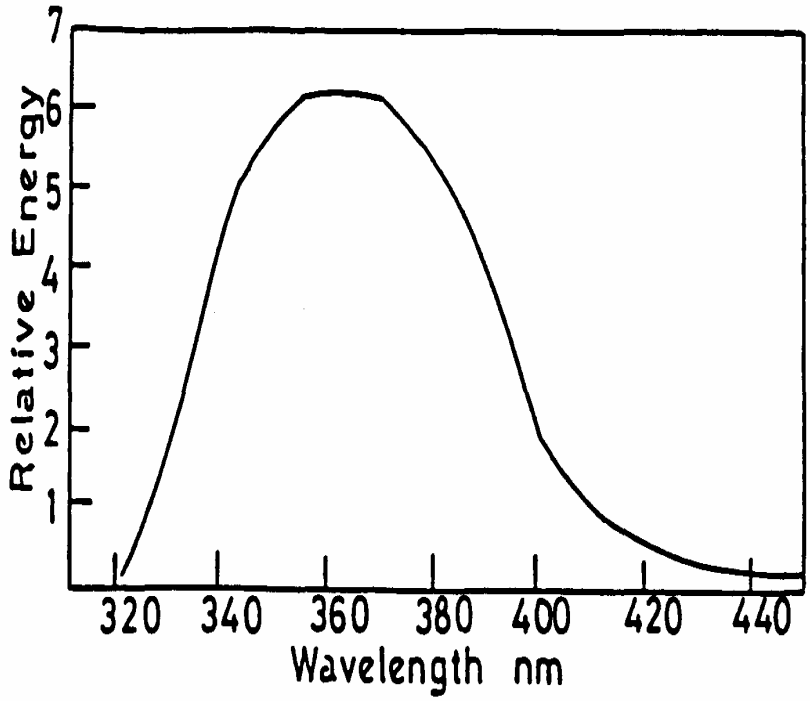

Figure 3.3. Emission spectrum of a black light fluorescent lamp

4. RESULTS and DISCUSSION

4.1. Characterization Results

4.1.1. Scanning Electron Microscopy (SEM) Analysis

Structural morphology of raw ZSM-5 and TiO_2 supported ZSM-5 catalysts were revealed by SEM micrographs. Raw ZSM-5 illustrated a kind of uniform morphology with similar rhombic crystals (Figure 4.1). 1.42 per cent Al_2O_3 and 97.57 per cent SiO_2 were found as the contents of raw ZSM-5 (Figure 4.1 inset). The EDX analysis of raw ZSM-5 did not exhibit titania peak. Figure 4.2 showed image of 40-TiO_2-ZSM-5 catalyst and evidently demonstrated destruction of the ZSM-5's structure with the adsorption of titania. A more random structure was obtained and formation of heterogeneously dispersed particles was detected. Within this new structure, sharp-edged, flat, irregularly localized particles with non-uniform diameters were also noticed. Since they were not obtained before, such agglomerates attributed to the formation of TiO_2 nanoparticles on the surface of ZSM-5 support. The EDX spectrum of such an aggregate exhibited 74.69 per cent of titania (Figure 4.2 inset). In the image of 0.28 La-40 TiO_2-ZSM-5 catalyst, similar sharp-edged aggregates observed scanning of one of these aggregates gave 64.69 per cent titania and 20.31 per cent lanthanum (as a shoulder) (Figure 4.3 and inset)

:

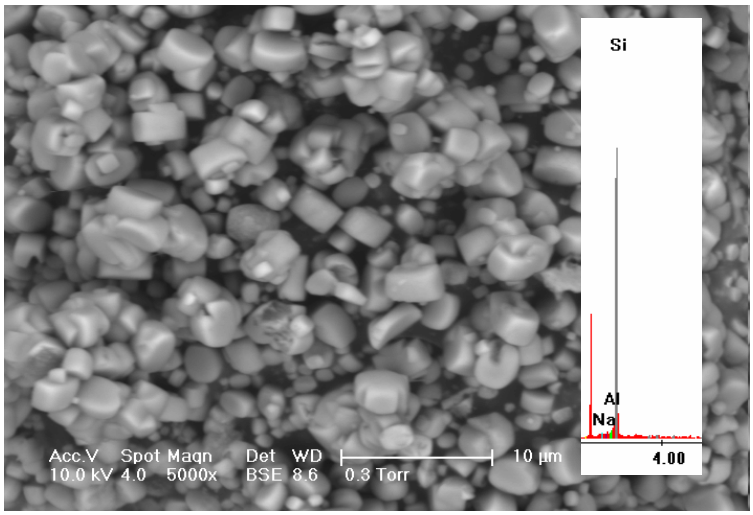

Figure 4.1. SEM image of raw ZSM-5. Inset: EDX spectrum of the whole surface

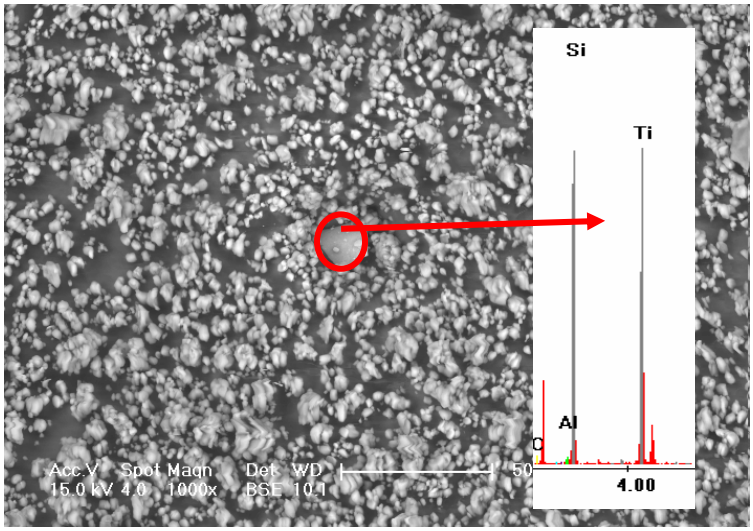

Figure 4.2. SEM image of 40-TiO_2-ZSM-5. Inset: EDX spectrum of the labeled sharp-edged aggregate

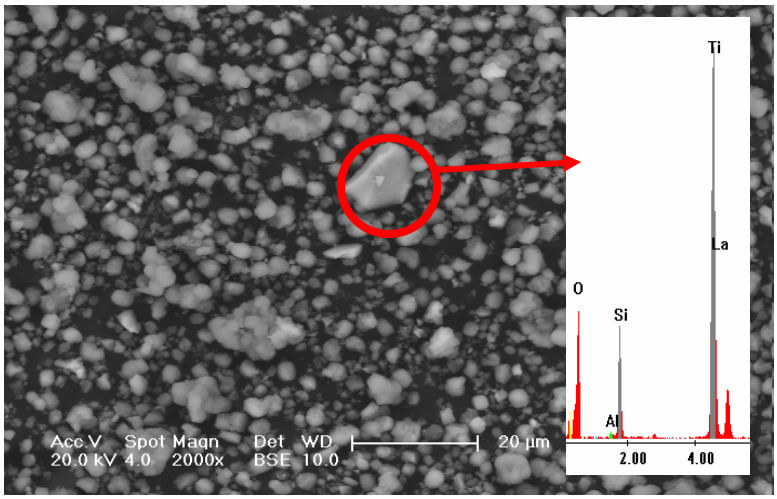

Figure 4.3. SEM image of 0.28 La-40 TiO_2-ZSM-5. Inset: EDX spectrum of the labeled distinct-edged aggregate

4.1.2. X-Ray Diffraction (XRD) Analysis

X-ray powder diffraction method was used to assess the crystallinity of the catalyst particles. Figure 4.4 illustrates XRD spectrums of 40-TiO_2 catalyst prepared at different temperatures. The characteristic anatase peak of diffraction (101) is detected at 25.18° (2θ) in the presence of 40-TiO_2 (400°C) (Figure 4.4 A). Other anatase diffractions of

(004), (200), (105) and (211) also appear at 37.87, 47.91, 53.76 and 55.02° (2θ), respectively. For 40-TiO_2 (600°C), (101), (004), (112), (200), (105) and (211) reflections are noticed at 25.09, 37.54, 38.38, 47.86, 53.62 and 54.76° (2θ), respectively (Figure 4.4 B). Relatively sharper and narrower X-ray peaks are observed for the catalyst prepared at 600°C due to the heat-induced growth of titania particles. This growth contributes to the increase of crystallinity and results in higher ordering in the structure of titania particles [48]. The crystalline size of anatase TiO_2 ($d_{anatase}$) is calculated from the (101) peak broadening by using Scherrer's equation as 12.41 nm for 40-TiO_2 (400^{o}C) and 19.34 nm for 40-TiO_2 (600^{o}C) (Table 4.1). Although anatase-rutile transition is known to occur at calcination temperatures above 400^{o}C [49,50], no rutile formation is observed in the catalyst calcined up to 600^{o}C, as exemplified by the absence of the main rutile (110) diffraction peak around 27^o (2θ).

The peak area of main anatase reflection (101) decreased with an increase in calcination temperature in the existence of 40-TiO_2 (800°C) catalyst and completely disappeared in the presence of 40-TiO_2 (1000°C) (Figure 4.4 C-D). Simultaneously, rutile reflections appear with respect to calcination temperature. For 40-TiO_2 (800°C), (110) main rutile reflection is observed at 27.08° (2θ) and others (101), (200), (111), (210), (211) and (220) are obtained at 35.68, 38.78, 40.76, 43.60, 53.82 and 56.12° (2θ), respectively. For 40-TiO_2 (1000°C), (110), (101), (200), (111), (210), (211) and (220) diffractions are detected at 27.06, 35.62, 38.74, 40.74, 43.58, 53.70 and 56.02° (2θ), respectively. It is found that the crystalline size of rutile particles is much bigger compared to that of anatase particles. d_{rutile} is estimated from the main (110) peak broadening as 34.33 nm for 40-TiO_2 (800^{o}C) and 37.87 nm for 40-TiO_2 (1000^{o}C).

Adsorption of TiO_2 nanoparticles on the surface of ZSM-5 creates variations in the XRD pattern of raw ZSM-5 (Figure 4.5). The basic differences are detected at low-angle range ($2\theta < 10^o$) for 7.86^o and 8.74^o (2θ) reflections and at high-angle ($20^o<2\theta<60^o$) range for 23.06 and 23.88^o reflections of ZSM-5. The intensities of these peaks decrease remarkably with the adsorption of TiO_2 nanoparticles. The other reflections remain essentially the same as that of raw ZSM-5.

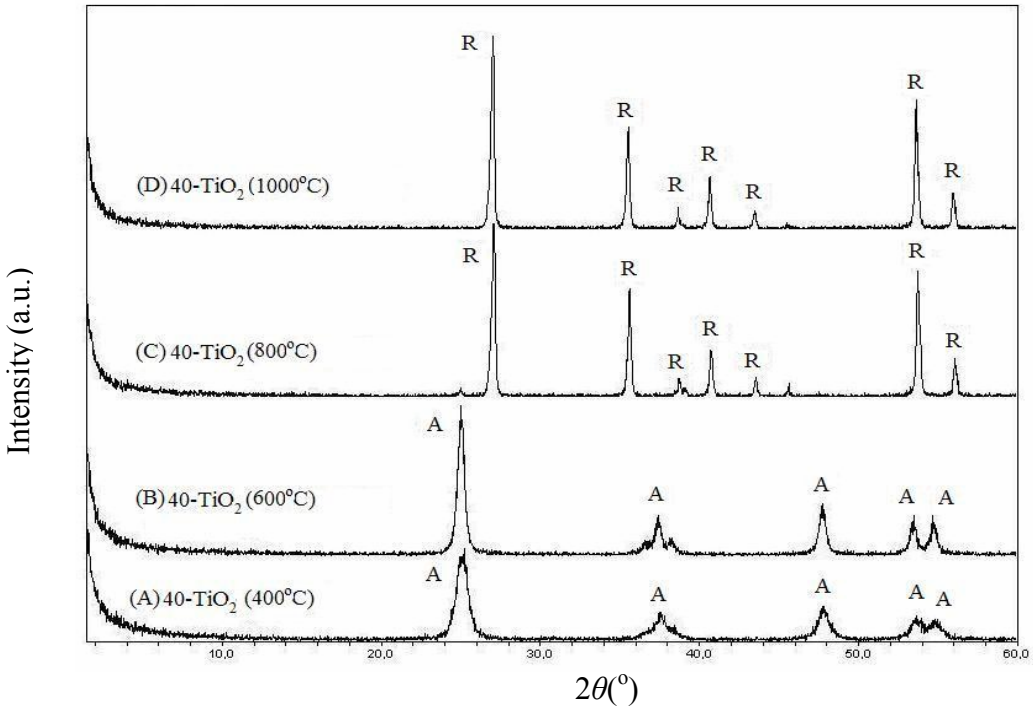

Figure 4.4. XRD patterns of 40-TiO_2 catalysts calcined at different temperatures.

Since the formation of crystalline phases on supported materials depends on loading, XRD patterns of catalysts are also investigated with respect to the content of TiO_2 in the final catalyst configuration at the same calcination temperature (400°C) (Figure 4.6). The low-angle and high-angle reflections of ZSM-5 support obviously decrease with the addition of titania in the resulting slurry. At lower concentration of titania, in the presence of 5-TiO_2-ZSM-5, we assume that the 5 per cent titania content is below the monolayer coverage. Thus, TiO_2 nanoparticles are well dispersed on the support and does not show a perfect phase transition (Figure 4.6 A). On the other hand, at higher loadings, (over the monolayer coverage) in the presence of 40-TiO_2-ZSM-5 and 60-TiO_2-ZSM-5catalysts, the increase of TiO_2 amount makes the diffusion on the surface easier and crystallization may occur sufficiently (Figure 4.6 B-C). Therefore, TiO_2 reflections are much more evident in the XRD pattern of 60-TiO_2-ZSM-5 catalyst (Figure 4.6 C). The crystalline sizes are calculated as 16.77 nm for 5-TiO_2-ZSM-5, 12.41 nm for 40-TiO_2-ZSM-5 and 15.18 nm for 60-TiO_2-ZSM-5.

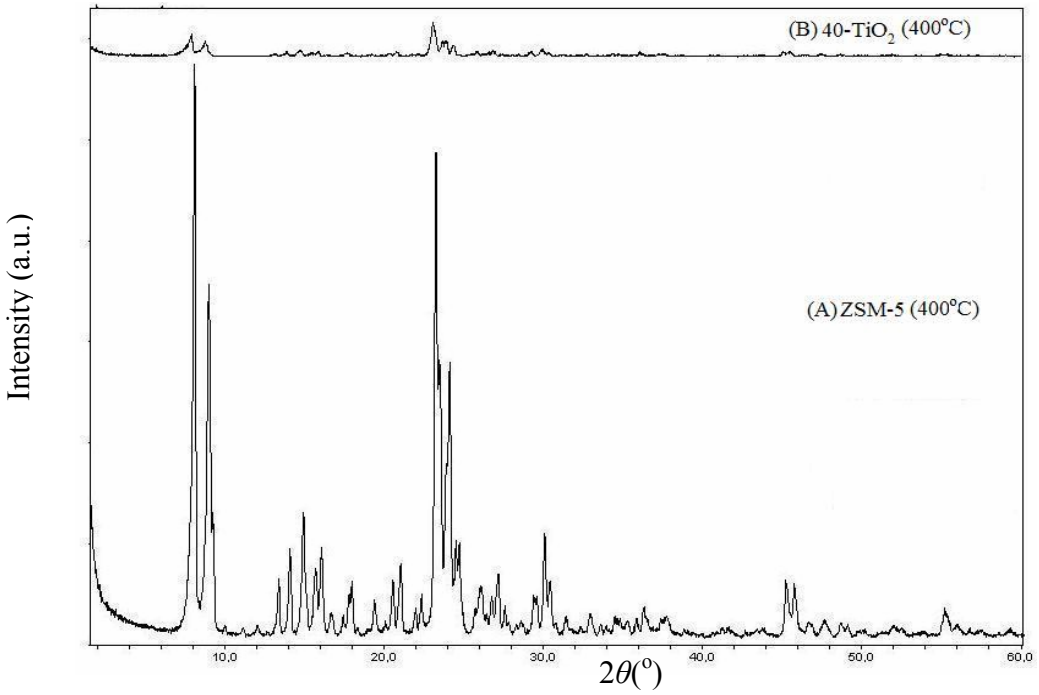

Figure 4.5. XRD patterns of (A) ZSM-5 and (B) 40-TiO_2-ZSM-5 (400°C)

The XRD patterns of 40-TiO_2-ZSM-5 catalysts calcined at different temperatures are revealed in Figure 4.7. In the high-angle diffractions ($20^o<2\theta<60^o$), XRD patterns of all the catalysts are complicated because of overlapping of diffraction peaks attributed to TiO_2 and those of ZSM-5. 40-TiO_2-ZSM-5 (400°C) and 40-TiO_2-ZSM-5 (600°C) catalysts exhibit main anatase reflection (101) at 25.78° and 25.52° (2θ), respectively. The intensities of these diffractions are much lower compared to that of catalysts prepared in the absence of the support (Table 4.1). The decrease in peak intensities and thus the decrease in full-width-half-maximum values of these peaks results in an increase in $d_{anatase}$ values as being 35.88 nm for 40-TiO_2-ZSM-5 (400°C) and for 43.04 nm for 40-TiO_2-ZSM-5 (600°C) (Table 4.1). Also, no peak assigned to rutile phase is observed in the XRD diffractograms of 40-TiO_2-ZSM-5 catalysts prepared at 400°C and 600°C. This confirms that TiO_2 nanoparticles formed on the surface of ZSM-5 is in the stable anatase phase. However, supported catalysts calcined at 800°C and 1000°C exhibit only rutile phase. Main rutile diffraction (110) at around 27.43° and 27.42° (2θ) in the presence of 40-TiO_2-ZSM-5 (800°C) and 40-TiO_2-ZSM-5 (1000°C), overlaps 26.90° and 26.92° (2θ) reflections of the ZSM-5, thus not clearly detectable in the XRD patterns shown in Figure 4.7 C and D. Likewise anatase phase, intensities of these rutile peaks are much lower compared to

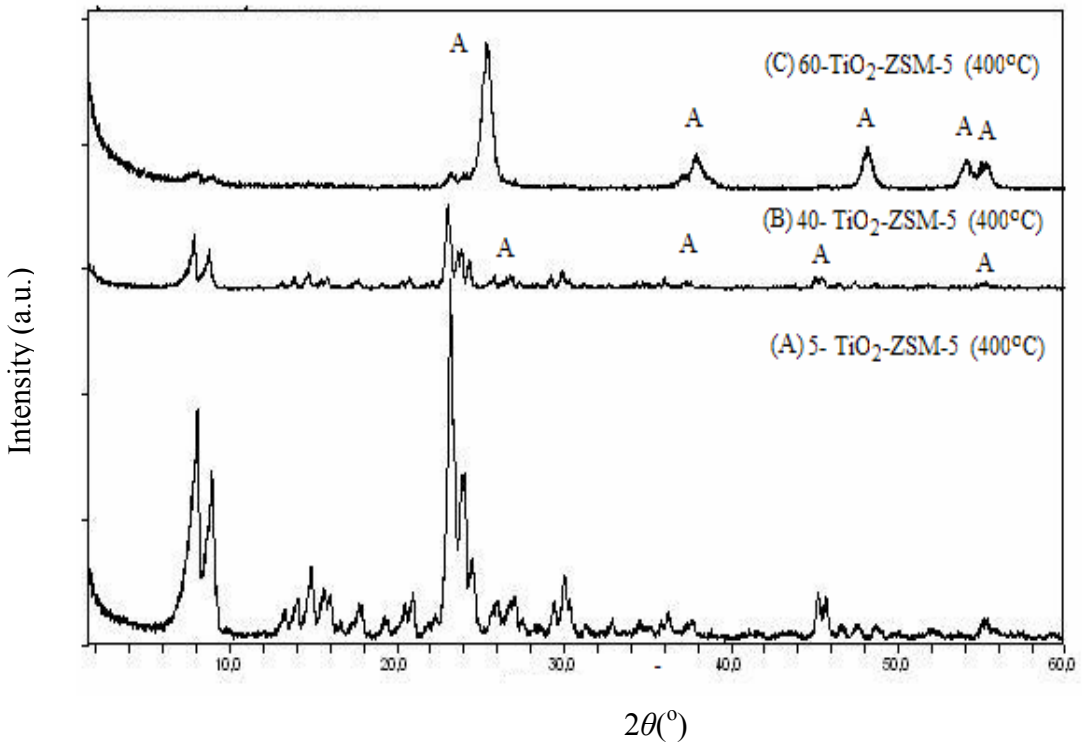

Figure 4.6. XRD patterns of (A) 5-TiO_2-ZSM-5 (400°C), (B) 40-TiO_2-ZSM-5 (400°C) and (C) 60-TiO_2-ZSM-5 (400°C)

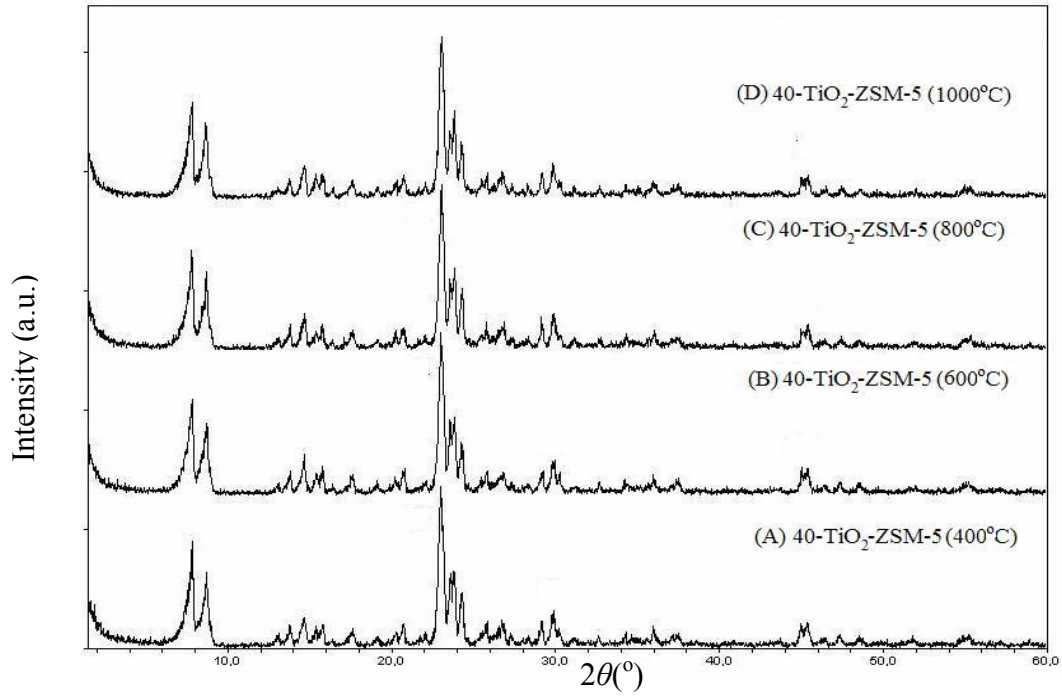

Figure 4.7. XRD patterns of 40-TiO_2-ZSM-5 catalyst calcined at different temperatures

that of catalysts prepared without the support. Table 4.1 shows main anatase and rutile reflections, their 2θ values, their intensities (I), full-width-half-maximum (FWHM)values and diameters of anatase and rutile (d). For other reflections, only specific 2θ values and their peak intensities are presented. As a result of decrease in full-width-half-maximum values of these peaks, d_{rutile} is found as 191.81 nm for 40-TiO_2 -ZSM-5 (800^oC) and 126.05 nm for 40-TiO_2 -ZSM-5 (1000^oC).

Adsorption of metal ions on the free-acidic sites of 40-TiO_2-ZSM-5 (400°C) catalysts is demonstrated in the XRD spectrums of corresponding catalysts by the formation of La_2O_3, Y_2O_3 and Ce_2O_3 reflections (Figure 4.8–4.10). In addition to ZSM-5 and anatase peaks, for 0.28 La-40 TiO_2-ZSM-5 (400°C) catalyst, specific La_2O_3 diffractions of (002), (011), (012), (110), (111), (112), (201) are observed at 29.20, 29.98, 39.44, 45.87, 48.59, 55.39 and 55.88° (2θ), respectively (Figure 4.8). Similarly, for 0.28 Y-40 TiO_2-ZSM-5 (400°C) catalyst, specific Y_2O_3 diffractions of (211), (222), (400), (411), (134), (440), (026) are obtained at 20.54, 29.24, 33.76, 36.13, 43.74, 48.90 and 55.03° (2θ), respectively (Figure 4.9). Also, 0.28 Ce-40 TiO_2-ZSM-5 (400°C) catalyst exhibits specific Ce_2O_3 diffractions of (100), (002), (011), (003), (110), (112) at 26.40, 29.29, 30.40, 45.08, 46.68 and 56.10° (2θ), respectively (Figure 4.10).

XRD spectrums of 0.28 La-40 TiO_2-ZSM-5, 0.28 Y-40 TiO_2-ZSM-5 and 0.28 Ce-40 TiO_2-ZSM-5 catalysts are also analyzed at different calcination temperatures (Figure 4.11 – Figure 4.13). All anatase-rutile peak intensities, main reflection's ((101) for anatase and (110) for rutile), full-width-half-maximum values and the corresponding "$d_{anatase}$" and "d_{rutile}" diameters are given in Table 4.2. In general, intensities decrease when the calcination temperatures of the catalysts increase. However, full-width-half-maximum-values of main reflections and also diameters of anatase and rutile do not exhibit a similar trend. Table 4.3 supplies information about the metal-oxides including main reflection's of each metal, their full-width-half-maximum values and the corresponding "d_{metal}" dimeters. According to the main (011) reflection of La_2O_3, d_{La2O3} is approximately found as 27 nm for 0.28 La-40 TiO_2-ZSM-5 at each temperature value. For 0.28 Ce-40 TiO_2-ZSM-5, d_{Ce2O3} with respect to (011) reflection is evaluated as 25 nm. In contrast to 0.28 La-40

TiO_2-ZSM-5 and 0.28 Ce-40 TiO_2-ZSM-5, 0.28 Y-40 TiO_2-ZSM-5 catalyst exhibits d_{Y2O3} approximately as 43 nm for the main reflection of (222). For each of these catalysts, almost no change is noticed in the specific metal-oxide peak reflections at different calcination temperatures.

Table 4.1. XRD data of 40-TiO_2- and 40-TiO_2-ZSM-5 catalysts at different temperatures.

40-TiO_2	2θ	I/FWHM/d	40-TiO_2-ZSM-5	2θ	I/FWHM/d
	25.18	**157/0.711/12.41***		**25.78**	**33/0.246/35.88***
	37.88	33		37.59	21
400°C	47.92	64	400°C	48.60	18
	53.76	42		54.98	16
	55.02	37		-	-
	25.06	**278/0.456/19.34***		**25.52**	**25/0.205/43.04***
	37.54	50		37.58	26
600°C	38.38	19	600°C	48.64	20
	47.86	97		54.76	8
	53.62	45		-	-
	27.08	**347/0.257/34.33****		**27.43**	**13/0.046/191.81****
	35.68	214		36.11	32
	38.78	33		41.06	7
800°C	40.76	91	800°C	43.84	12
	43.60	36		56.54	3
	56.12	75		-	-
	27.06	**386/0.233/37.86****		**27.42**	**19/0.070/126.05****
	35.62	202		36.04	26
	38.74	41		41.03	7
1000°C	40.74	104	1000°C	43.82	7
	43.58	35		54.44	2
	56.02	69		-	-

*: $d_{anatase}$

**: d_{rutile}

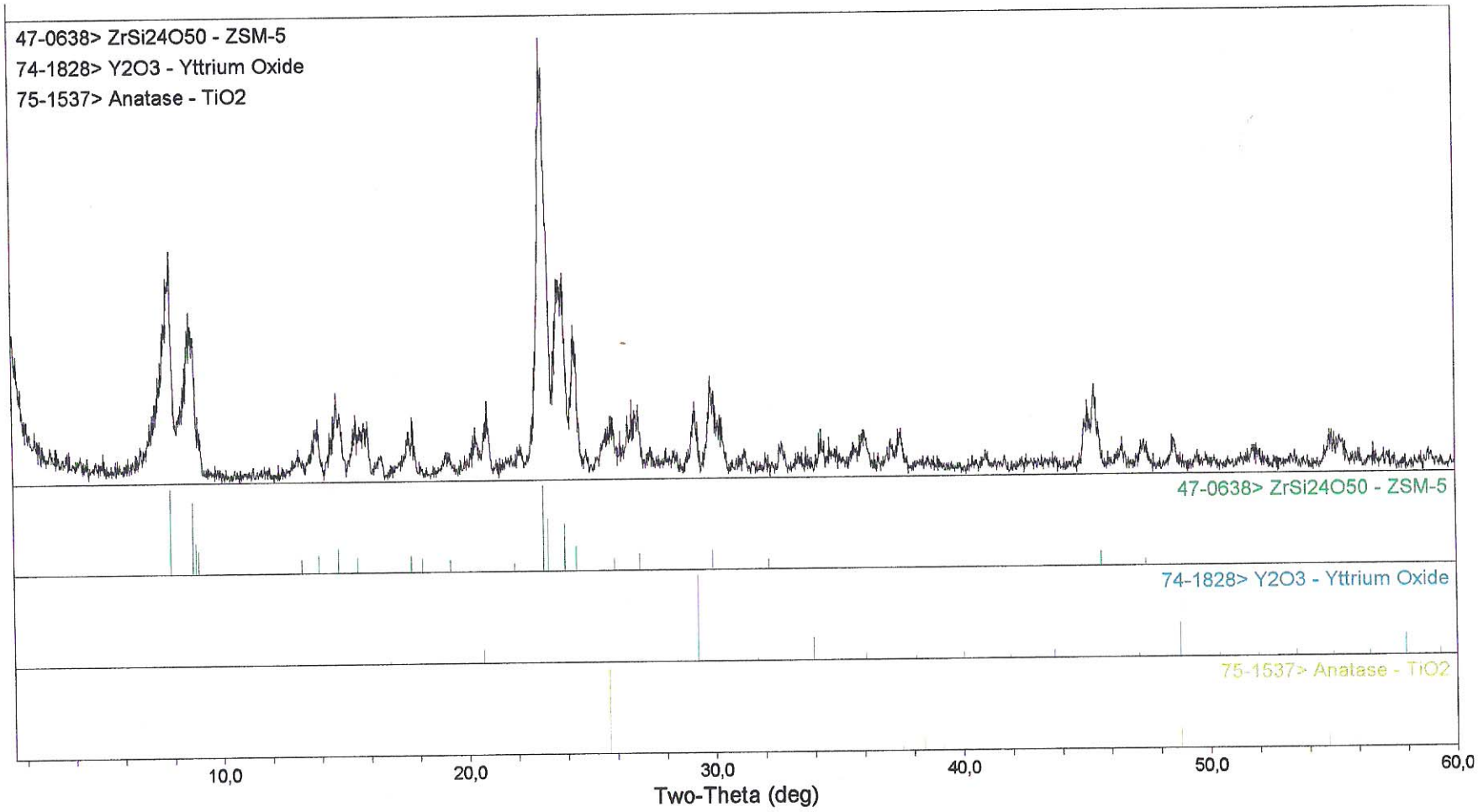
47-0638> ZrSi24O50 - ZSM-5
74-1828> Y2O3 - Yttrium Oxide
75-1537> Anatase - TiO2
47-0638> ZrSi24O50 - ZSM-5
74-1828> Y2O3 - Yttrium Oxide
75-1537> Anatase - TiO2
10,0
20,0
30,0
40,0
50,0
60,0
Two-Theta (deg)

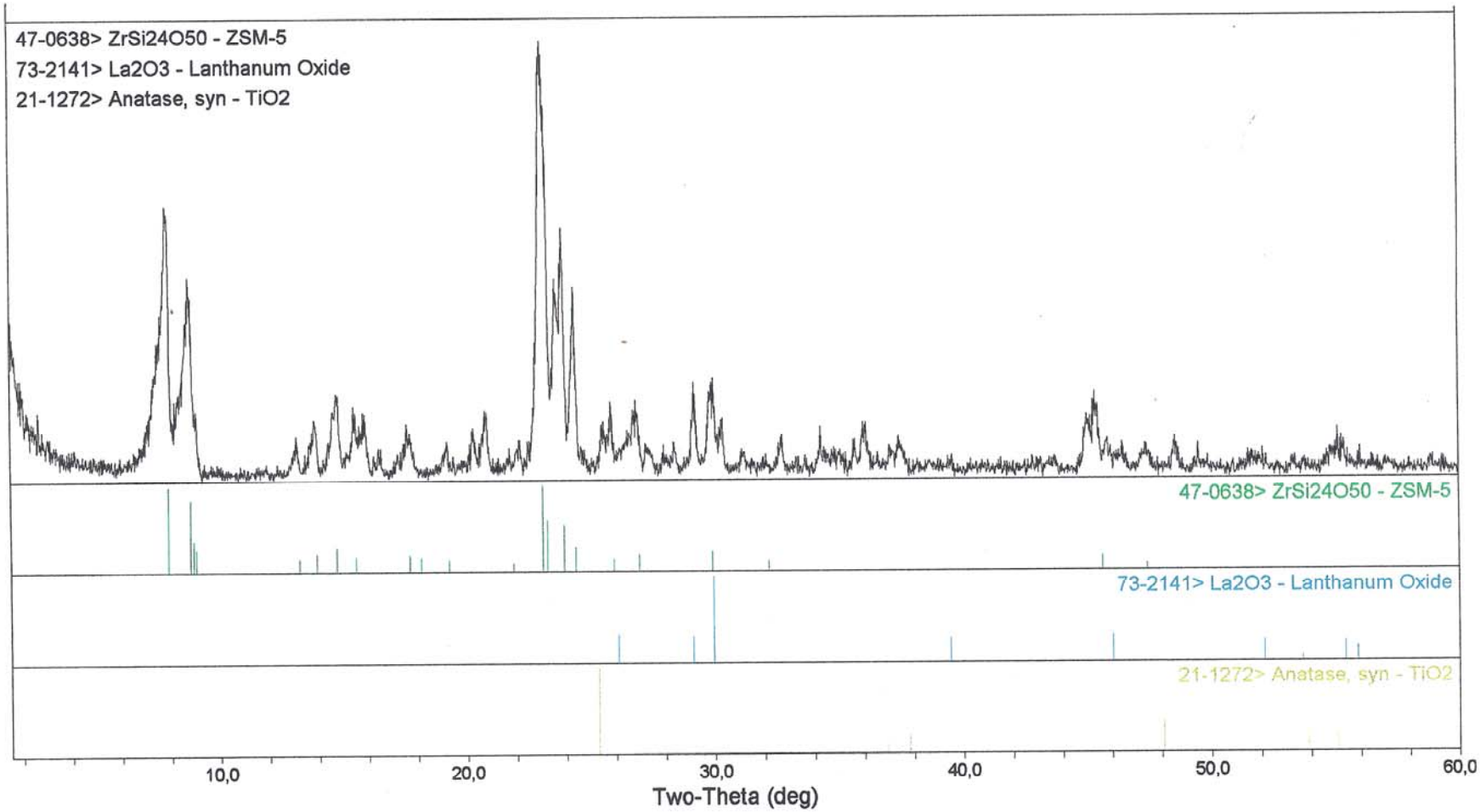
47-0638> ZrSi24O50 - ZSM-5
73-2141> La2O3 - Lanthanum Oxide
21-1272> Anatase, syn - TiO2
47-0638> ZrSi24O50 - ZSM-5
73-2141> La2O3 - Lanthanum Oxide
21-1272> Anatase, syn - TiO2
10,0
20,0
30,0
40,0
50,0
60,0
Two-Theta (deg)

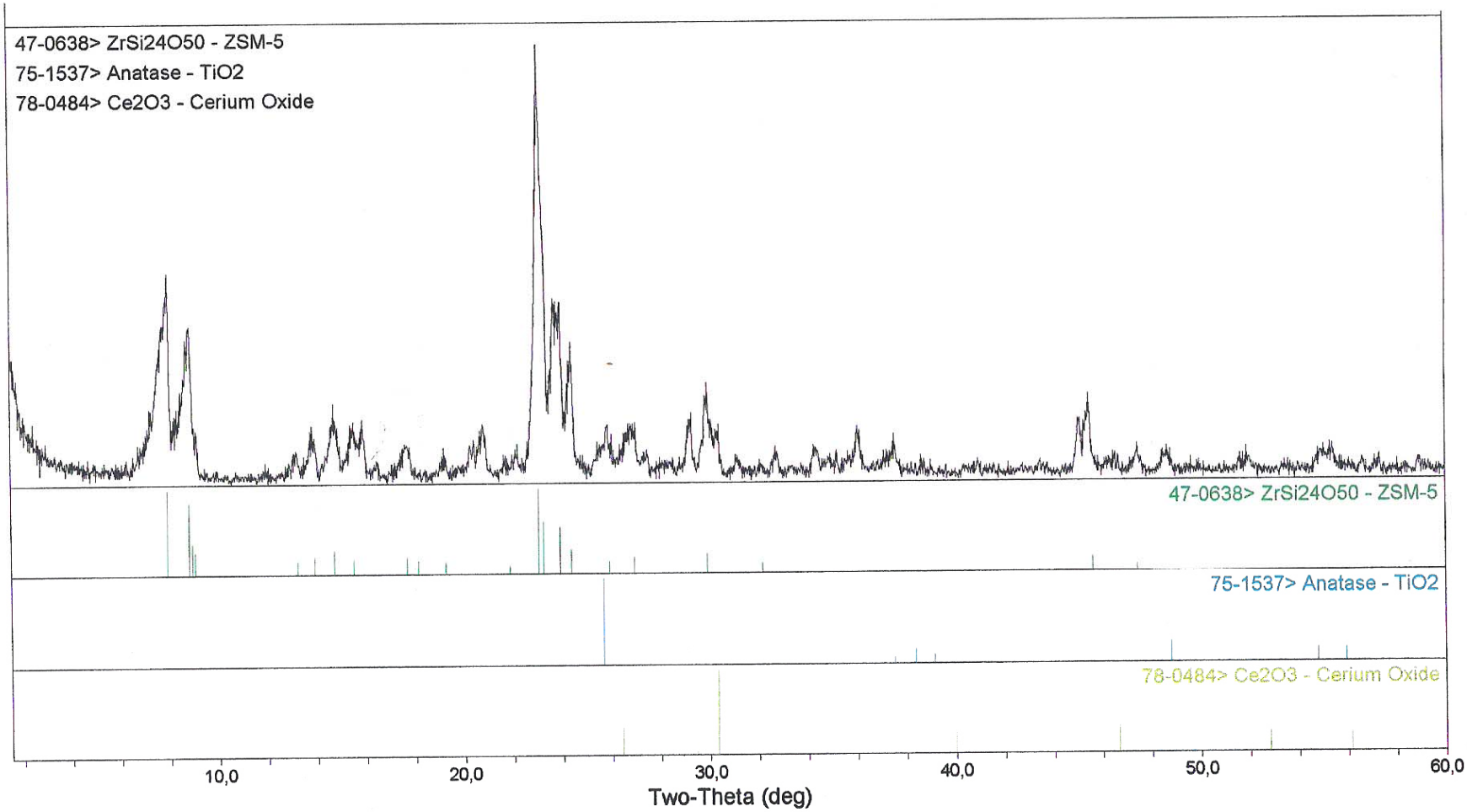
47-0638> ZrSi24O50 - ZSM-5
75-1537> Anatase - TiO2
78-0484> Ce2O3 - Cerium Oxide
47-0638> ZrSi24O50 - ZSM-5
75-1537> Anatase - TiO2
78-0484> Ce2O3 - Cerium Oxide
10,0
20,0
30,0
40,0
50,0
60,0
Two-Theta (deg)

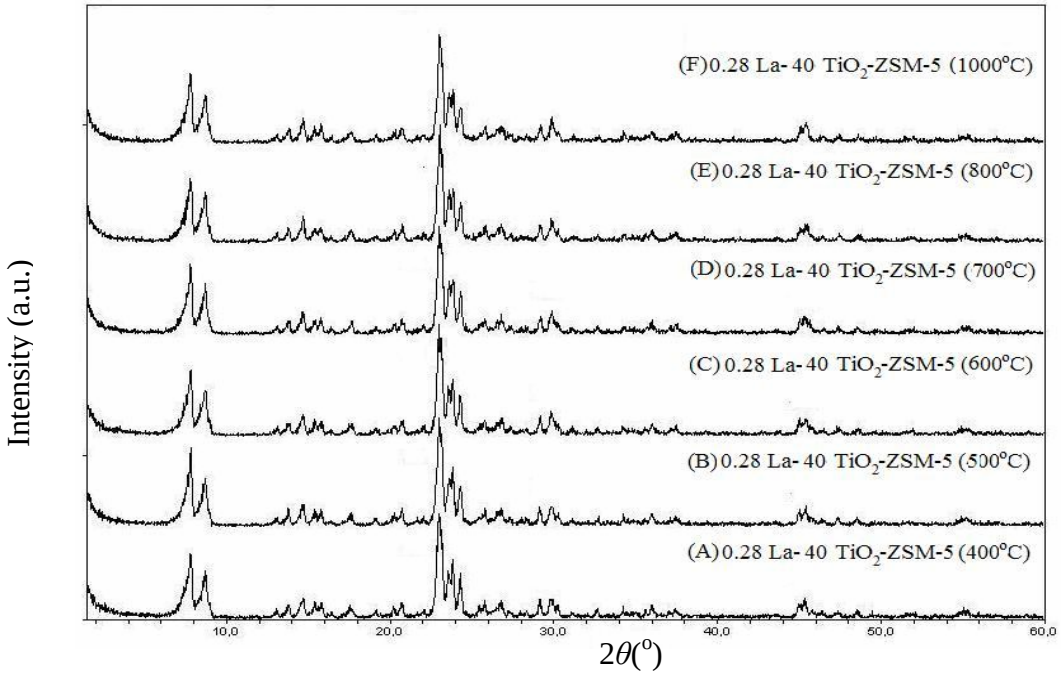

Figure 4.11. XRD patterns of 0.28 La-40 TiO_2-ZSM-5 catalysts calcined at different temperatures.

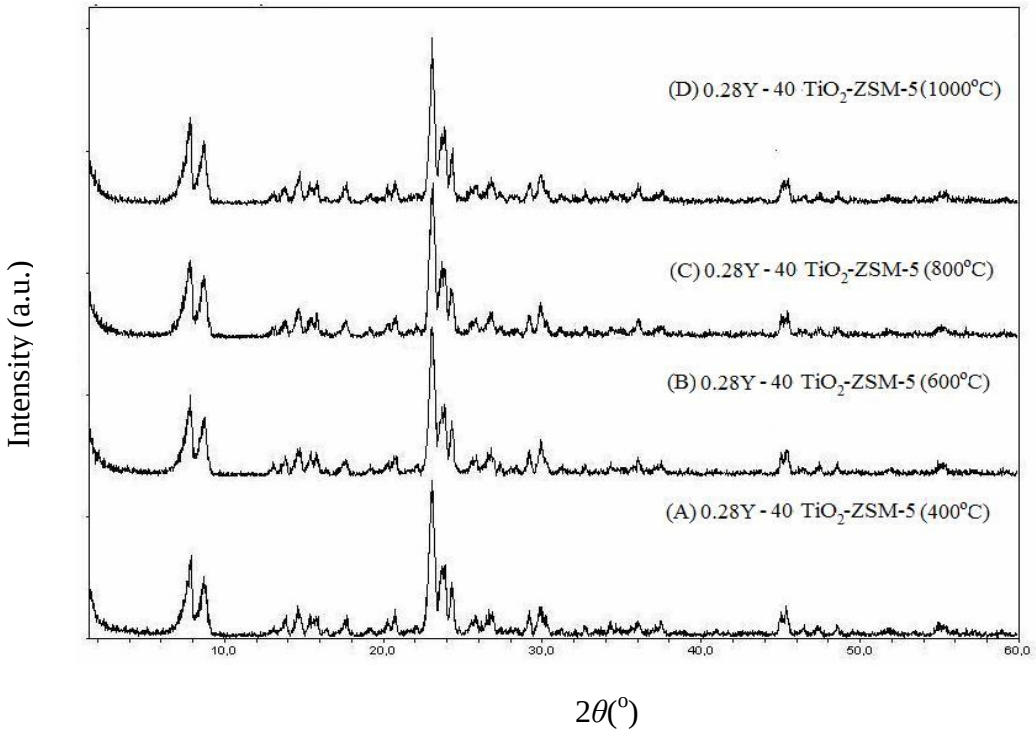

Figure 4.12. XRD patterns of 0.28 Y-40 TiO_2-ZSM-5 catalysts calcined

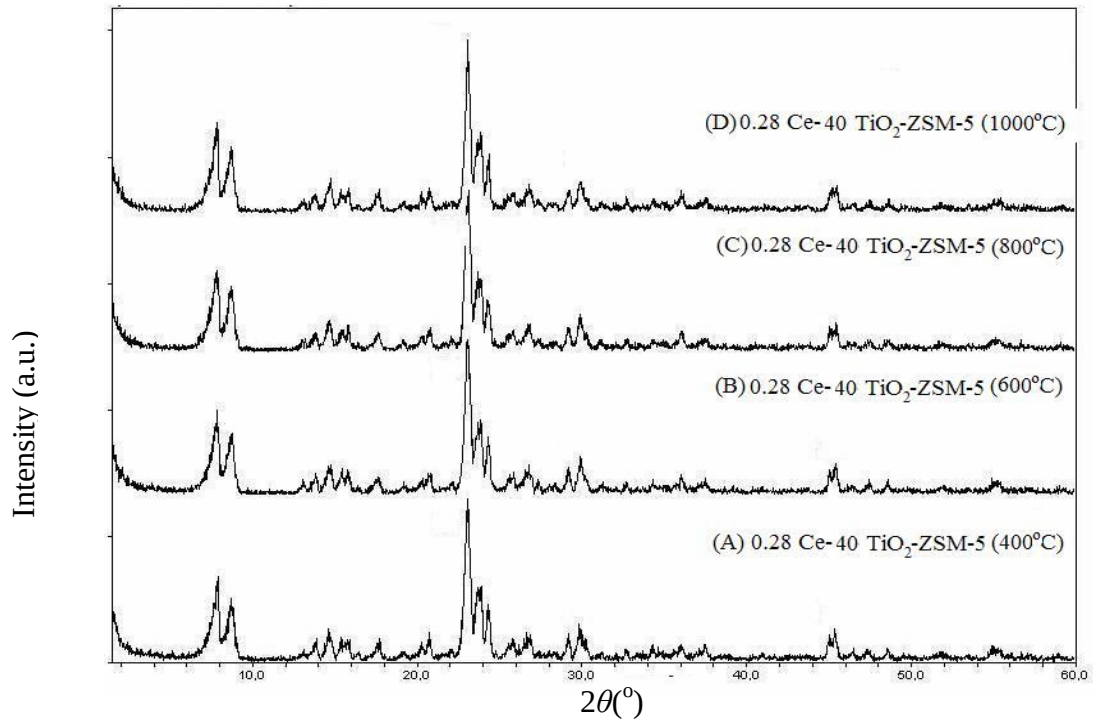

Figure 4.13. XRD patterns of 0.28 Ce-40 TiO_2-ZSM-5 catalysts calcined at different temperatures.

The variation in the metal percentage is also examined following the XRD patterns of La-40 TiO_2-ZSM-5 catalysts at different temperatures. In Table 4.4 all anatase-rutile peak intensities, main reflection's ((101) for anatase and (110) for rutile) full-width-half-maximum values and the corresponding "$d_{anatase}$" and "d_{rutile}" diameters of 0.5 La-40 TiO_2-ZSM-5, 1.0 La-40 TiO_2-ZSM-5 and 3.0 La-40 TiO_2-ZSM-5 are given. An increase is detected both in anatase and rutile crystalline sizes in between 0.5 La-40 TiO_2-ZSM-5 and 1.0 La-40 TiO_2-ZSM-5. However, in the case of 3 per cent loading, anatase crystalline sizes are a bit lower than the others. Thus, we expect that there is an optimum amount for the metal ion to be adsorbed on the surface of TiO_2-ZSM-5 catalysts, and beyond which adsorption decreases. In addition to these data, La_2O_3 reflections are followed in the presence of 0.5 La-40 TiO_2-ZSM-5, 1.0 La-40 TiO_2-ZSM-5 and 3.0 La-40 TiO_2-ZSM-5 (Table 4.5). Main (011) reflection of La_2O_3 results in similar d_{La2O3} sizes for all calcination temperatures studied.

Table 4.2. XRD data of 0.28 La-40 TiO_2-ZSM-5 (1), 0.28 Y-40 TiO_2-ZSM-5 (2) and 0.28 Ce-40 TiO_2-ZSM-5 (3) catalysts.

(1)	2θ	I/FWHM/d	(2)	2θ	I/FWHM/d	(3)	2θ	I/FWHM/d
400°C	**25.54**	**27/0.193/45.72***	400°C	**25.73**	**22/0.295/29.91***	400°C	**25.46**	**14/0.331/26.66***
	37.61	12		37.60	27		37.56	29
	54.99	13		55.91	5		55.73	6
600°C	**25.56**	**23/0.280/31.51***	600°C	**25.71**	**27/0.286/30.85***	600°C	**25.61**	**23/0.197/44.79***
	37.54	27		35.60	19		37.58	20
	54.98	20		55.90	25		55.83	21
800°C	**27.44**	**18/0.129/68.40****	800°C	**27.41**	**9/0.020/441****	800°C	**27.49**	**15/0.062/142.32****
	36.10	30		36.04	24		36.11	28
	38.78	33		56.78	16		56.78	4
	56.74	4		-	-		-	-
1000°C	**27.51**	**18/0.288/30.64****	1000°C	**28.39**	**14/0.137/64.41****	1000°C	**27.48**	**16/0.150/58.82****
	36.08	24		36.07	28		36.09	30
	41.04	16		56.58	7		56.81	7
	56.70	3		-	-		-	-

*: $d_{anatase}$

**: d_{rutile}

Table 4.3. XRD data of 0.28 La-40 TiO_2-ZSM-5 (1), 0.28 Y-40 TiO_2-ZSM-5 (2) and 0.28 Ce-40 TiO_2-ZSM-5 (3).

(1)	2θ	I/FWHM/d	(2)	2θ	I/FWHM/d	(3)	2θ	I/FWHM/d
	29.98	**63/0.326/27.07**		**29.24**	**46/0.179/49.29**		**30.41**	**34/0.347/25.42**
400°C	39.45	9	400°C	33.76	15	400°C	45.08	40
	45.87	19		36.14	21		46.68	12
	29.94	**57/0.339/26.03**		**29.28**	**44/0.205/43.04**		**30.37**	**25/0.321/27**
600°C	39.57	8	600°C	36.12	30	600°C	45.03	26
	45.86	18		43.74	6		46.50	12
	48.66	19		-	-		56.19	5
	29.94	**61/0.368/27.07**		**29.27**	**37/0.208/42.42**		**30.38**	**32/0.299/29.51**
800°C	39.41	5	800°C	33.84	5	800°C	45.05	14
	45.90	13		43.79	8		46.61	17
	48.54	14		48.75	17		56.10	3
	29.95	**50/0.323/27.32**		**29.30**	**29/0.204/43.25**		**30.40**	**25/0.551/16**
1000°C	39.61	7	1000°C	33.96	8	1000°C	45.08	17
	46.10	7		43.72	8		46.6	13
	48.67	19		48.72	22		56.18	7
	55.47	16		55.10	19		-	-

Table 4.4. XRD data of 0.5 La-40 TiO_2-ZSM-5 (1), 1.0 La-40 TiO_2-ZSM-5 (2) and 3.0 La-40 TiO_2-ZSM-5 (3).

(1)	2θ	I/FWHM/d	(2)	2θ	I/FWHM/d	(3)	2θ	I/FWHM/d
400°C	**25.75**	**29/0.275/32***	400°C	**25.52**	**24/0.144/61.67***	400°C	**25.76**	**21/0.334/26.42***
	37.53	17		37.50	22		37.50	18
	48.66	14		48.60	19		48.63	15
	54.93	13		54.75	14		54.73	10
600°C	**25.70**	**21/0.279/31.6***	600°C	**25.80**	**30/0.202/43.68***	600°C	**25.82**	**24/0.280/31.51***
	37.44	25		37.47	21		37.54	20
	48.69	18		48.68	15		48.78	19
	54.90	21		54.90	17		54.77	11
800°C	**27.41**	**10/0.133/66****	800°C	**27.39**	**16/0.113/78.08****	800°C	**27.44**	**12/0.152/58.05****
	36.00	22		36.08	20		36.18	20
	56.66	7		56.68	8		56.72	8
1000°C	**27.35**	**21/0.0941/94****	1000°C	**27.38**	**9/0.110/80.21****	1000°C	**27.40**	**22/0.083/106****
	36.04	24		36.04	25		36.11	25
	56.61	16		56.76	15		56.74	9

*: $d_{anatase}$

**: d_{rutile}

Table 4.5. XRD data of 0.5 La -40 TiO_2-ZSM-5 (1), 1.0 La -40 TiO_2-ZSM-5 (2), 3.0 La -40 TiO_2-ZSM-5 (3) catalysts at different calcination temperatures. For main La_2O_3 reflections, 2θ values, their corresponding intensities (I), full-width-half-maximum values (FWHM) and diameters of La_2O_3 (d) are given. For other reflections, only specific 2θ values and their peak intensities are presented.

(1)	2θ	I/FWHM/d	(2)	2θ	I/FWHM/d	(3)	2θ	I/FWHM/d
400°C	**30.00**	**37/0.459/19.22**	400°C	**30.02**	**42/0.413/21.36**	400°C	**29.94**	**46/0.323/27.32**
	39.70	6		39.36	7		39.4	6
	45.98	2		46.28	13		46.23	8
600°C	**29.99**	**36/0.478/18.46**	600°C	**29.94**	**48/0.410/21.52**	600°C	**29.94**	**48/0.369/23.91**
	39.5	3		39.55	5		39.52	4
	46.28	6		46.35	11		46.32	7
800°C	**29.96**	**43/0.390/22.62**	800°C	**29.94**	**49/0.410/24.64**	800°C	**29.96**	**58/0.369/30.62**
	39.46	8		39.44	6		39.5	4
	45.98	4		45.96	4		46.14	9
1000°C	**29.99**	**42/0.384/22.98**	1000°C	**29.94**	**53/0.292/30.22**	1000°C	**29.94**	**55/0.328/26.90**
	39.48	7		39.44	2		39.4	3
	45.98	7		46.07	5		46.19	12

A general remark concerning the XRD patterns of ZSM-5 and all supported catalysts, intensity of raw zeolite peaks decreases remarkably with the adsorption TiO_2 and metal-oxide nanoparticles. For raw zeolite, main reflections (101), (020), (051) and (033) appear at 8.08, 8.96, 23.23 and 24.08° (2θ), respectively. The intensities of these peaks are in given in Table 4.6. The obvious decrements in the intensities of these peaks observed in the presence of 40-TiO_2-ZSM-5, 0.28 Y -40 TiO_2-ZSM-5, 0.28 Ce-40 TiO_2-ZSM-5 at different temperatures (Table 4.7). Besides, variation in the metal percentages also results in decrements of raw ZSM-5 peak intensities (Table 4.8). A relatively high intensity of 7.90° (2θ) in the presence of 3.0 La-40 TiO_2-ZSM-5 in comparison to 0.28 La-40 TiO_2-ZSM-5, 0.5 La-40 TiO_2-ZSM-5 and 1.0 La-40 TiO_2-ZSM-5 again underlines the limit of adsorption on the surface of 40-TiO_2-ZSM-5.

Table 4.6. Main peak diffractions (2θ) of ZSM-5 and their corresponding intensities (I)

	2θ	I
ZSM-5	8.08	5601
	8.96	3444
	23.23	4697
	24.08	2664

4.1.3. Atomic Force Microscopy (AFM) Analysis

The morphology of raw ZSM-5, 40-TiO_2, 40-TiO_2-ZSM-5, 0.28 Y-40 TiO_2-ZSM-5, 0.28 La-40 TiO_2-ZSM-5 and 0.28 Ce-40 TiO_2-ZSM-5 at 400^{o}C are analyzed using AFM technique. The three-dimensional (3-D) AFM image of ZSM-5 is shown in Figure 4.14 A. The data obtained from this image (not shown) is the average roughness value (R_a) of the sample. This value is approximately equal to 0.119 nm for raw ZSM-5 indicating the presence of a smooth surface. In Figure 4.14 B, 3-D image of 40-TiO_2 (400^{o}C) is revealed. This image has a roughness value of 0.36 nm. Two-dimensional (2-D) image (top-view) and underneath this image particle size distribution plot (Figure 4.14 C) of 40-TiO_2

Table 4.7. Decrements in the peak intensities of ZSM-5 support in the presence of 40-TiO_2-ZSM-5 (1), 0.28 Y 40-TiO_2-ZSM-5 (2) and 0.28 Ce-40 TiO_2-ZSM-5 (3).

(1)	2θ	(I)	(2)	2θ	(I)	(3)	2θ	(I)
	7.86	**183**		**7.93**	**132**		**7.94**	**120**
400°C	8.74	153	400°C	8.74	118	400°C	8.84	113
	23.06	328		23.08	311		23.08	318
	23.88	151		23.93	140		23.96	126
	7.86	**168**		**7.89**	**130**		**7.90**	**120**
600°C	8.74	146	600°C	8.74	117	600°C	8.80	131
	23.04	331		23.08	299		23.14	277
	23.89	150		23.92	140		23.89	125
	7.84	**175**		**7.87**	**122**		**7.92**	**131**
800°C	8.76	159	800°C	8.74	123	800°C	8.84	126
	23.06	330		23.16	306		23.14	306
	23.88	160		23.96	130		23.90	120
	7.86	**167**		**7.86**	**145**		**7.94**	**143**
1000°C	8.74	157	1000°C	8.74	126	1000°C	8.76	129
	23.06	328		23.06	329		23.16	296
	23.88	169		23.88	142		23.94	146

Table 4.8. Decrements in the peak intensities of ZSM-5 support in the presence of 0.28 La 40-TiO_2-ZSM-5 (1), 0.5 La 40-TiO_2-ZSM-5 (2), 1.0 La-40 TiO_2-ZSM-5 (3) and 3.0 La-40 TiO_2-ZSM-5 (4).

(1)	2θ	(I)	(2)	2θ	(I)	(3)	2θ	(I)	(4)	2θ	(I)
	7.82	**164**		**7.76**	**118**		**7.84**	**84**		**7.90**	**149**
400°C	8.74	143	400°C	8.68	113	400°C	8.76	90	400°C	8.80	110
	23.06	307		23.04	271		23.08	234		23.04	260
	23.86	171		23.82	118		23.88	114		23.86	143
	7.88	**159**		**7.80**	**132**		**7.84**	**112**		**7.84**	**132**
600°C	8.74	134	600°C	8.72	119	600°C	8.72	97	600°C	8.76	126
	23.04	329		23.04	284		23.08	238		23.06	254
	23.89	159		23.86	141		23.84	116		23.90	135
	7.84	**154**		**7.80**	**144**		**7.80**	**115**		**7.84**	**143**
800°C	8.78	150	800°C	8.72	120	800°C	8.72	118	800°C	8.68	125
	23.08	346		23.04	266		23.06	262		23.08	268
	23.90	150		23.82	132		23.86	120		23.88	127
	7.84	**177**		**7.82**	**168**		**7.80**	**117**		**7.86**	**150**
1000°C	8.74	142	1000°C	8.70	131	1000°C	8.70	118	1000°C	8.74	134
	23.06	318		23.02	276		23.06	266		23.08	297
	23.90	149		23.88	127		23.84	123		23.92	126

(400°C) are also exhibited. The average particle diameter from the 2-D image in 40-TiO_2 (400°C) is found as 75 nm. In the distribution plot, a particle (more than that seems a kind of aggregate) with 87.81 nm diameter is labeled as an example. For 40-TiO_2-ZSM-5 (400°C) catalyst, both the increase in R_a value to 0.6 nm and the notification of unordered domes may indicate deposition of TiO_2 nanoparticles on the surface of ZSM-5 structure (Figure 4.15 A). An average particle size value is found as 128 nm for this catalyst and an aggregate of 121.3 nm is labeled (Figure 4.15 B). In the presence of 0.28 Y-40 TiO_2-ZSM-5 catalyst, a uniform protrusion like structure is observed (Figure 4.15 C) with R_a value of 0.33 nm. The decrement in the R_a value of this catalyst in comparison to that obtained in 40-TiO_2-ZSM-5 (400°C) may suggest more homogenous localization of TiO_2 and Y_2O_3 nanoparticles. From 2-D image of 0.28 Y-40 TiO_2-ZSM-5 (400°C), (Figure 4.15 D), an average diameter of 53 nm is labeled in the distribution plot. A more careful examination of 2-D image of this catalyst ends up with the observation of much smaller sized aggregates. The morphology and R_a value (0.27 nm) of 0.28 La-40 TiO_2-ZSM-5 (400°C) (Figure 4.16 A) is similar to that of 0.28 Y-40 TiO_2-ZSM-5 (400°C). However, aggregate sizes are bigger (average value of 63 nm). An aggregate with 65.29 nm diameter is labeled in the distribution plot of 0.28 La-40 TiO_2-ZSM-5 (400°C) (Figure 4.16 B). Among the metal oxide incorporated catalysts, 0.28 Ce-40 TiO_2-ZSM-5 (400°C) shows the highest particle sizes (with an average value of 115 nm) and the highest R_a value of 0.59 nm. Also, creation of spherical domes illustrates the variation in surface morphology of this catalyst in comparison to 0.28 Y-40 TiO_2-ZSM-5 (400°C) and 0.28 La-40 TiO_2-ZSM-5 (400°C) (Figure 4.16 C-D). The particle size of each catalyst extremely different from the XRD calculated sizes. In the XRD analysis, both TiO_2 nanoparticles and metal oxide nanoparticles are evaluated according to the main diffraction angles of anatase, Y_2O_3, La_2O_3 and Ce_20_3 reflections by the application of Scherer's equation. However, in the AFM studies, separation of TiO_2 nanoparticles from the metal oxide nanoparticles is not possible. Also, the technique for the preparation of AFM samples is different. Agglomeration of particles in local regions of the support is highly probable and detectable in the AFM images. Therefore, the measured values by AFM are the size of aggregates in contrast to the size of single crystallites calculated by XRD.

(A) ZSM-5

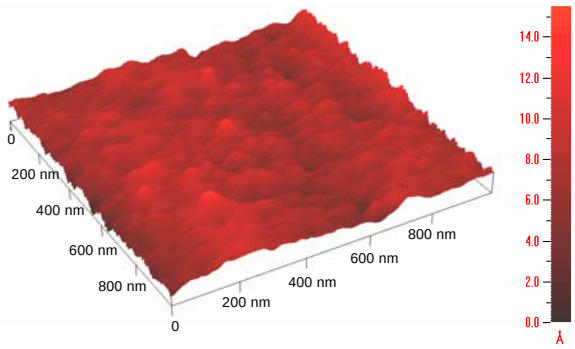

(B) 40-TiO_2 (400°C)

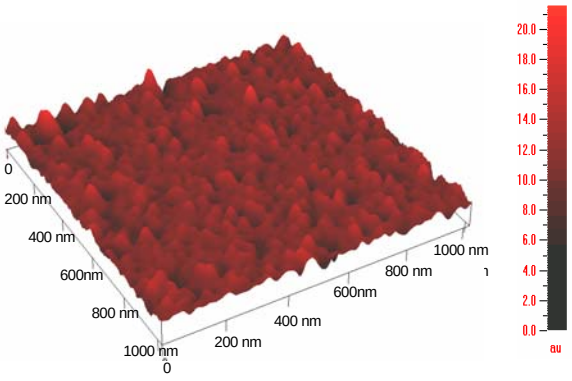

(C) 40-TiO_2 (400°C)

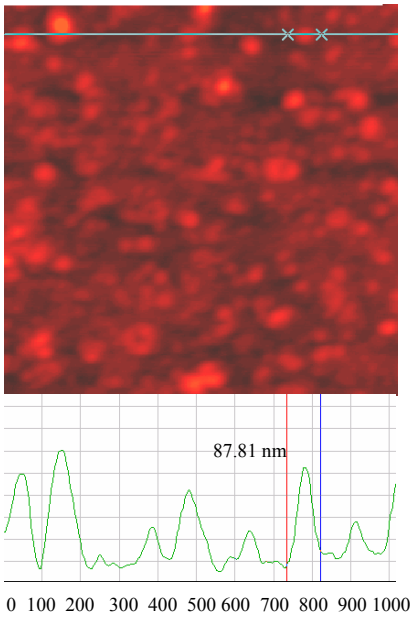

Figure 4.14. Three-dimensional AFM images of (A) ZSM-5, (B) 40 TiO_2 (400°C) and two-dimensional (top-view) image of (C) 40-TiO_2 (400°C

(A) 40 -TiO_2-ZSM-5 (400°C)

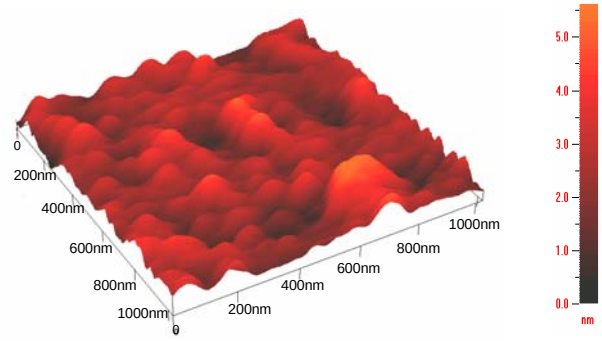

(B) 40 -TiO_2-ZSM-5 (400°C)

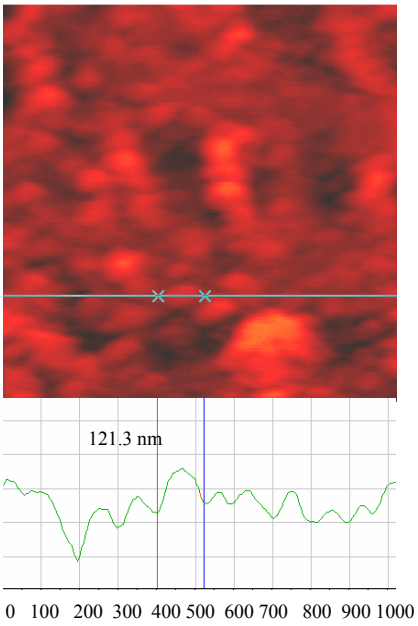

(C) 0.28 Y-40 TiO_2-ZSM-5 (400°C)

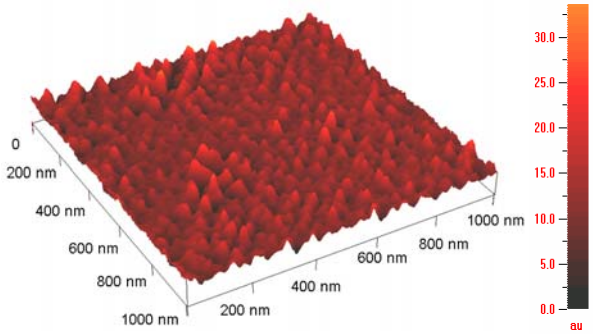

(D) 0.28 Y-40 TiO_2-ZSM-5 (400°C)

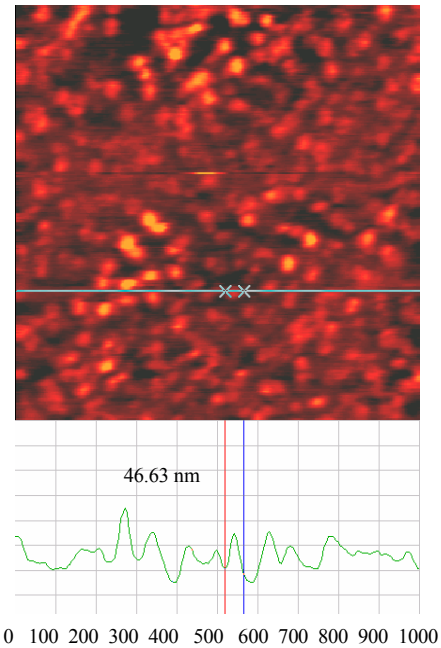

Figure 4.15. Three-dimensional images of (A) 40-TiO_2-ZSM-5 (400°C), (B) 0.28 Y-40 TiO_2-ZSM-5 (400°C) and two-dimensional (top-view) images of (C) 40-TiO_2-ZSM-5 (400°C) and (D) 0.28 Y-40 TiO_2-ZSM-5 (400°C)

(A) 0.28 La-40 TiO_2-ZSM-5 (400°C)

(B) 0.28 La-40 TiO_2-ZSM-5 (400°C)

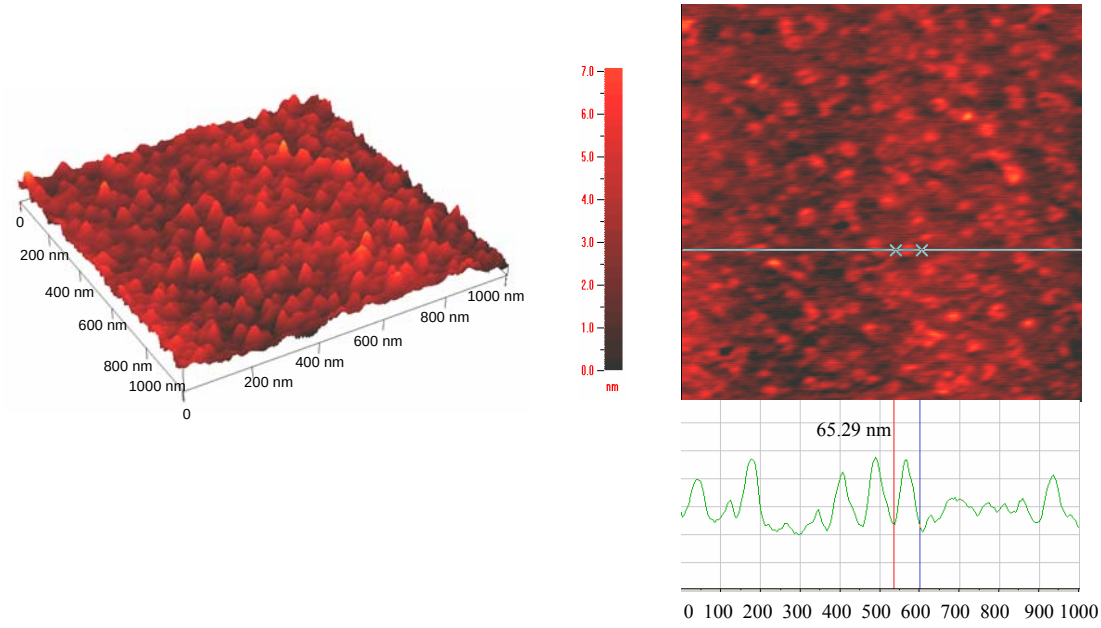

(C) 0.28 Ce-40 TiO_2-ZSM-5 (400°C)

(D) 0.28 Ce-40 TiO_2-ZSM-5 (400°C)

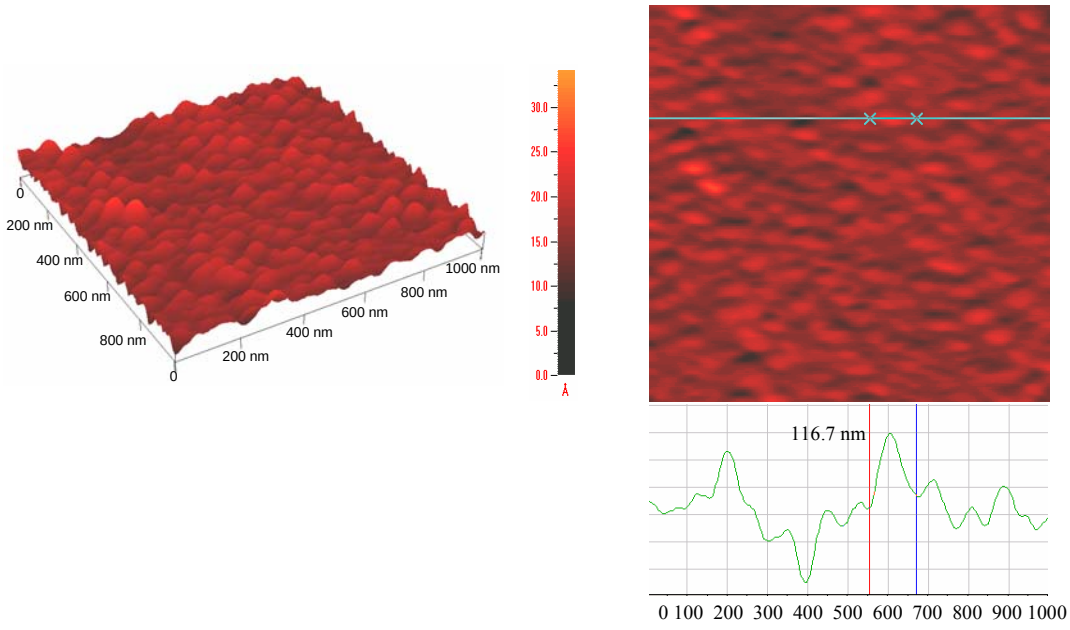

Figure 4.16. Three-dimensional images of (A) 0.28 La-40 TiO_2-ZSM-5 (400°C), (B) 0.28 Ce-40 TiO_2-ZSM-5 (400°C) and two-dimensional (top-view) images of (C) 0.28 La-40 TiO_2-ZSM-5 (400°C) and (D) 0.28 Ce-40 TiO_2-ZSM-5 (400°C)

4.1.4. BET Analysis

The specific surface area is determined from multi-point BET analysis. Table 4.9 shows surface areas of TiO_2 (Degussa P-25), ZSM-5 (Aldrich), 10-TiO_2 (400°C), 40-TiO_2 (400°C) and all supported catalysts prepared at 400°C. After loading TiO_2 on ZSM-5, the surface area of all supported catalysts decreased compared to raw ZSM-5. Incorporation of metal oxides on the surface of 40-TiO_2-ZSM-5 results in further decrements. However, variation in metal ion percentage, in the case of La-40 TiO_2-ZSM-5 catalyst, does not induce a remarkable change and presents almost similar BET values. This observation is consistent with the XRD analysis of the same catalysts, indicating an optimum value of metal oxide adsorption on the corresponding supports.

Table 4. 9. Surface areas (BET) of TiO_2 (Degussa P-25), ZSM-5 (Aldrich), 10-TiO_2 (400°C), 40-TiO_2 (400°C) and all supported catalysts prepared at 400°C.

Catalysts	Surface Area (m^2/g)
TiO_2[a]	50
ZSM-5[b]	400
10-TiO_2	118.3
40-TiO_2	119.2
40-TiO_2-ZSM-5	121.1
0.28 Y-40 TiO_2-ZSM-5	88.24
0.28 Ce-40 TiO_2-ZSM-5	107.9
0.28 La-40 TiO_2-ZSM-5	108.8
0.5 La-40 TiO_2-ZSM-5	119.1
1.0 La-40 TiO_2-ZSM-5	118.5
3.0 La-40 TiO_2-ZSM-5	117.6

[a]: Reported BET of Degussa P-25

[b]: Reported BET of ZSM-5 (Across)

4.2. Photolytic Degradation of MeO

The photolytic degradation of methyl orange at 464 nm is followed at different initial concentrations; 32.7, 16.3, 8.17, 3.27 and 1.63 mg/L about 90 min irradiation time (Figure 4.17). For each of these concentrations, the amount of MeO remaining in solution does not exhibit a significant variation (Table 4.10). The inset in Figure 4.17 represents UV-Vis spectrum of 3.27 mg/L sample.

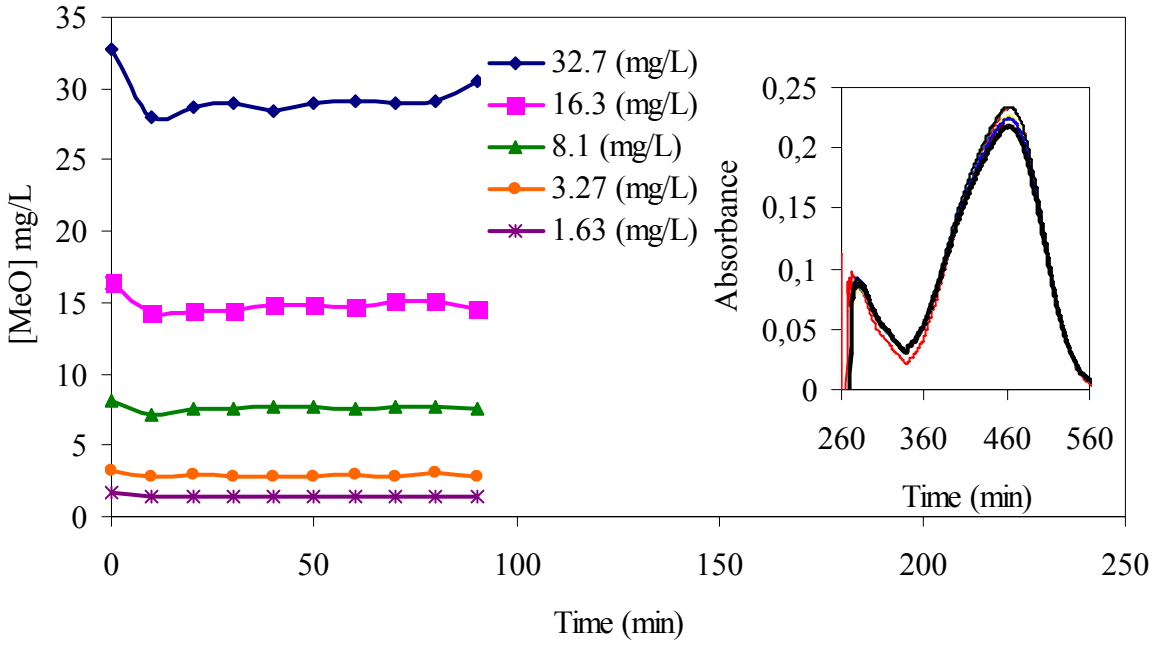

Figure 4.17. Photolytic degradation of MeO at different concentrations. Inset: UV-Vis spectrum of 3.27 mg/L sample. Conditions: pH= 5.85 (Natural), I= 4.7×10^{15} photons/s, T=298 K, Flow rate= 2000 rpm.

Table 4.10. Photolytic degradation of MeO at different initial concentrations.

Time (min)	[MeO] (mg/L)				
0	32.70	16.35	8.17	3.27	1.63
10	27.98	14.25	7.15	2.85	1.36
20	28.66	14.40	7.54	2.89	1.38
30	28.92	14.40	7.55	2.85	1.38
40	28.38	14.86	7.74	2.78	1.41
50	29.04	14.78	7.66	2.85	1.37
60	29.16	14.74	7.50	2.98	1.38
70	29.04	15.12	7.63	2.82	1.38
80	29.12	15.05	7.68	3.10	1.37
90	30.49	14.61	7.51	2.74	1.41

4.3. Photocatalytic Degradation of MeO in the Presence of TiO_2 (Degussa P-25) and 40-TiO_2 (400^oC)

Photocatalytic activities of TiO_2 (Degussa P-25) and 40-TiO_2 (400^oC) are controlled under UV-irradiation. Degussa seems to work more efficiently (Figure 4.18). The reported anatase size is 30 nm for Degussa. However, from Scherer's equation, it is calculated as around 140 nm. For 40-TiO_2 (400^oC) catalyst prepared in this study, the size of anatase particles is evaluated as around 12.4 nm.

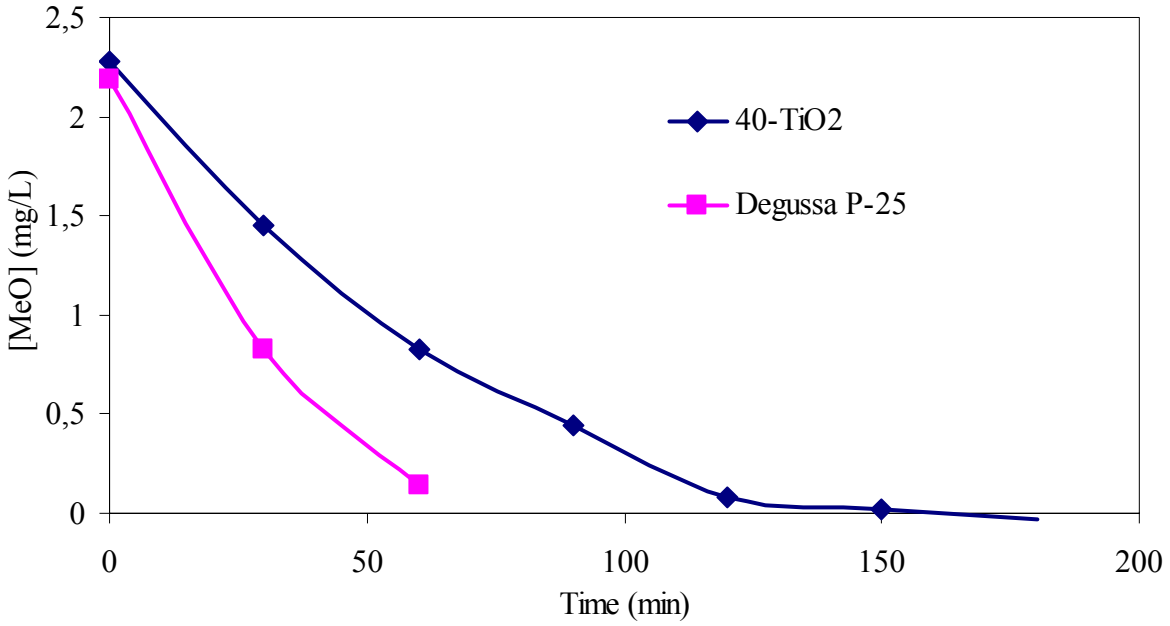

Figure 4.18. Photocatalytic activities of TiO_2 (Degussa P-25) and 40-TiO_2 (400°C)

4.4. Photocatalytic Degradation of MeO in the Presence of Supported Catalysts

4.4.1. Effect of TiO_2 Loading on ZSM-5

The TiO_2 content is important for the supported catalysts to decide for the degradation efficiencies. Therefore, the amount of titania-sol addition into the ZSM-5 suspension is regulated as being 10 per cent, 40 per cent and 60 per cent in the final catalyst configuration. After 30 min dark adsorption, MeO concentration remaining in solution is found to be correlated with the TiO_2 loading, i.e., 10-TiO_2-ZSM-5 catalyst adsorbs the lowest amount of MeO whereas 60-TiO_2-ZSM-5 catalyst adsorbs the maximum amount of MeO (Table 4.11). In accordance with these results, the highest degradation is achieved in the existence of 60-TiO_2-ZSM-5 catalyst after 90 min irradiation as seen in Figure 4.20. 10-TiO_2-ZSM-5 and 40-TiO_2-ZSM-5 catalysts, in contrast to 60-TiO_2-ZSM-5, need longer illumination periods. However, since we also want to introduce metal ions into the TiO_2-ZSM-5 system (by

expecting metal incorporations from the available Lewis acid-sites; which are also the sites of titania addition on the ZSM-5 surface), we perform all degradation experiments with 40 per cent TiO_2 loading. Figure 4.19 shows UV-Vis spectrum of MeO degradation in the presence of 40-TiO_2-ZSM-5. For all the time intervals applied, the maxima of the absorption spectra undergo a vertical shift toward the low values of the absorbance with decreasing the concentration of MeO.

Table 4.11. Concentration of MeO before dark adsorption (C_i) and after dark adsorption (C_0)

Catalysts	C_i (mg/L)	C_0 (mg/L)
10-TiO_2-ZSM-5	3.27	2.59
40-TiO_2-ZSM-5	3.27	2.61
60-TiO_2-ZSM-5	3.27	2.76

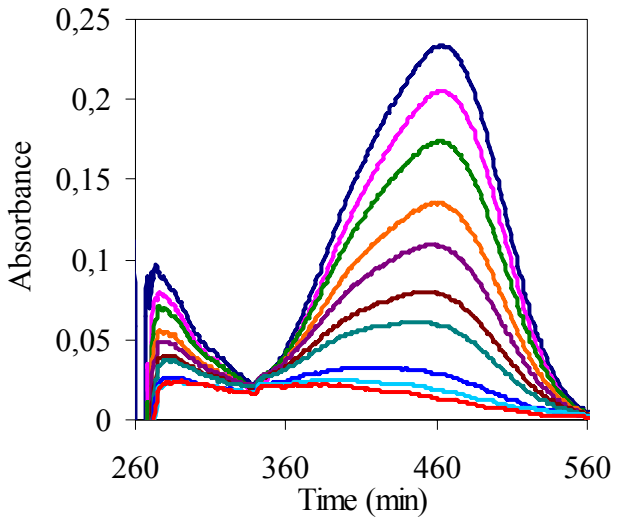

Figure 4.19. UV-Vis spectrum of MeO degradation in the presence of 40-TiO_2-ZSM-5. Conditions: pH= 5.85 (Natural), [MeO]= 3.27 mg/L, I= 4.7×10^{15} photons/s, T=298 K, Flow rate= 2000 rpm

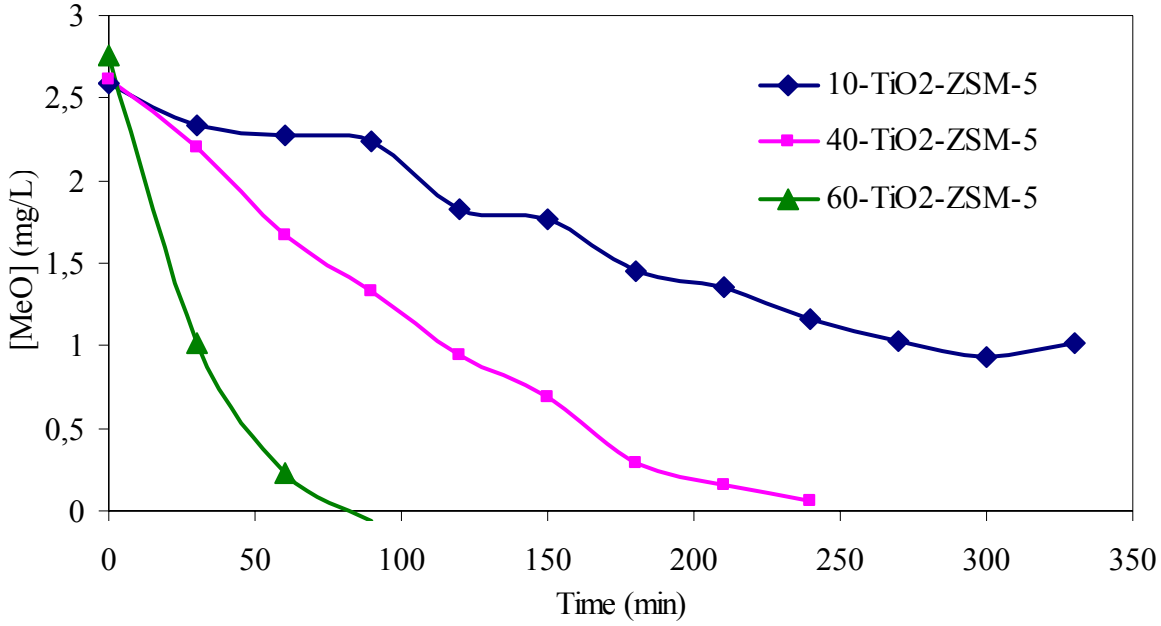

Figure 4.20. Effect of TiO_2 loading on the photocatalytic degradation of MeO. Conditions: pH= 5.85 (Natural), [MeO]= 3.27 mg/L, I= $4.7x10^{15}$ photons/s, T=298 K, Flow rate= 2000 rpm

4.4.2. Effect of Metal Ion Incorporation on 40-TiO_2-ZSM-5

The photocatalytic degradation of MeO has also been investigated in the presence of metal ion incorporated catalysts. With this purpose; two sets of experiments are designed. In the first set, the amount of metal concentrations is fixed, as being 0.28 at. per cent in the final catalyst configurations. Then, a comparison is made among the catalysts prepared in the presence of this fixed amount of metal ions. The second set of experiments examines the effect of metal ion content for the degradation process of MeO.

For the first set, decrease in MeO concentration is followed in the presence of 0.28 Y-40 TiO_2-ZSM-5, 0.28 La-40 TiO_2-ZSM-5 and 0.28 Ce-40 TiO_2-ZSM-5 about 330 min irradiation time (Figure 4.21). Initial concentrations of MeO in the figure belong to the values

after the dark adsorption (Table 4.11). UV-Vis spectrums of MeO degradation in the existence of these catalysts are also given in Figure 4.22. The results of these experiments apparently exhibited the following sequence for the efficiencies of these catalysts:

0.28 Y-40 TiO_2-ZSM-5> 0.28 La-40 TiO_2-ZSM-5 > 0.28 Ce-40 TiO_2-ZSM-5

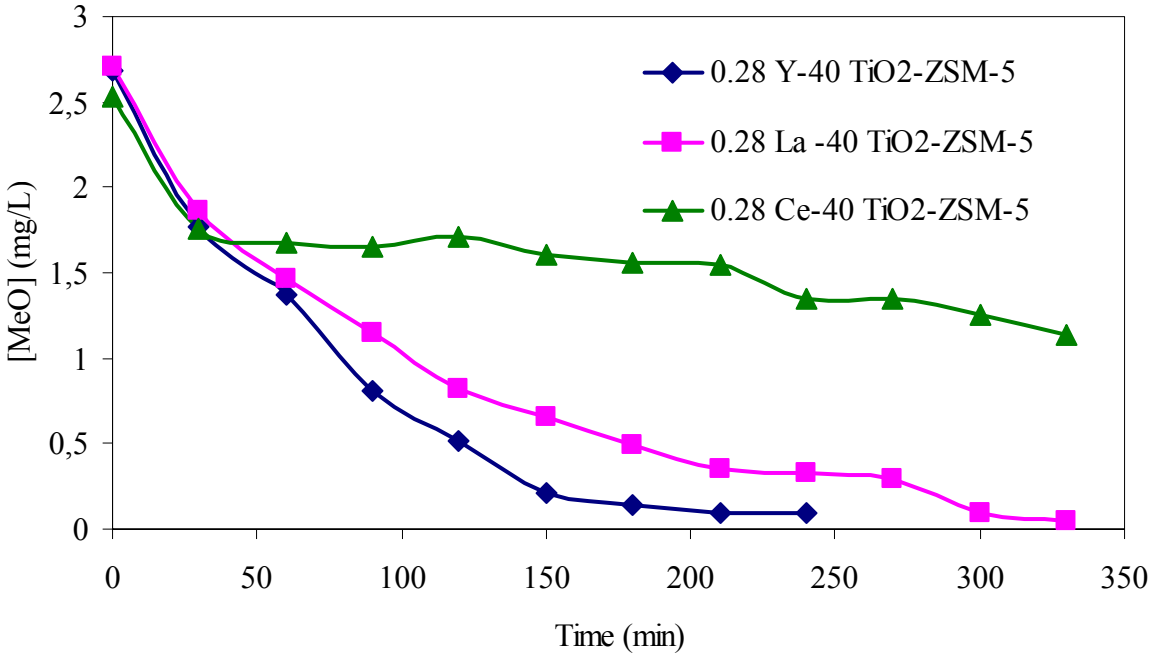

Figure 4.21. Effect of metal ion incorporation on 40-TiO_2-ZSM-5 for the photocatalytic degradation of MeO. Conditions: pH= 5.85 (Natural), [MeO]= 3.27 mg/L, I= 4.7×10^{15} photons/s, T=298 K, Flow rate= 2000 rpm

In the second set, the optimum amount of metal ion incorporation on 40 TiO_2-ZSM-5 catalyst (for each of the metal ions studied) is determined by changing the metal content as 0.28 at. per cent, 0.50 at. per cent, 1.00 at. per cent and 3.00 at. per cent in the resulting catalyst configuration. After checking MeO concentration in the dark (Table 4.12), degradation performances of these catalysts are examined for 330 min irradiation time (Figure 4.23, Figure 4.24, Figure 4.25). The highest degradation of MeO is observed in the presence

of catalysts including the lowest metal ion content. A further increase of in the metal ion loading results in a decrease of degradation rate. In such a condition, part of the catalyst surface probably becomes unavailable for the dye molecule adsorption and photon absorption. Thus, in the following sections, experiments are followed in the presence of 0.28 Y-40 TiO_2-ZSM-5, 0.28 La-40 TiO_2-ZSM-5 and 0.28 Ce-40 TiO_2-ZSM-5.

Table 4.12. Concentration of MeO before dark adsorption (C_i) and after dark adsorption (C_0)

Catalysts	C_i (mg/L)	C_0 (mg/L)
0.28 Y-40 TiO_2-ZSM-5	3.27	2.68
0.50 Y-40 TiO_2-ZSM-5	3.27	2.79
1.00 Y-40 TiO_2-ZSM-5	3.27	2.93
3.00 Y-40 TiO_2-ZSM-5	3.27	2.93
0.28 La-40 TiO_2-ZSM-5	3.27	2.46
0.50 La-40 TiO_2-ZSM-5	3.27	2.56
1.00 La-40 TiO_2-ZSM-5	3.27	2.69
3.00 La-40 TiO_2-ZSM-5	3.27	2.69
0.28 Ce-40 TiO_2-ZSM-5	3.27	2.52
0.50 Ce-40 TiO_2-ZSM-5	3.27	2.75
1.00 Ce-40 TiO_2-ZSM-5	3.27	2.90
3.00 Ce-40 TiO_2-ZSM-5	3.27	3.10

4.4.3. Effect of pH

The solution pH is known to play an important role in the photocatalytic process of various pollutants **[**51**]**. Before investigating the effect of pH on the photodegradation of MeO, the UV-Vis spectrophotometer is calibrated in the pH range of 2.7-11 (Figure 4.26).

Since there is a strong dependence of adsorption capacity on pH, dark adsorption in the presence of raw

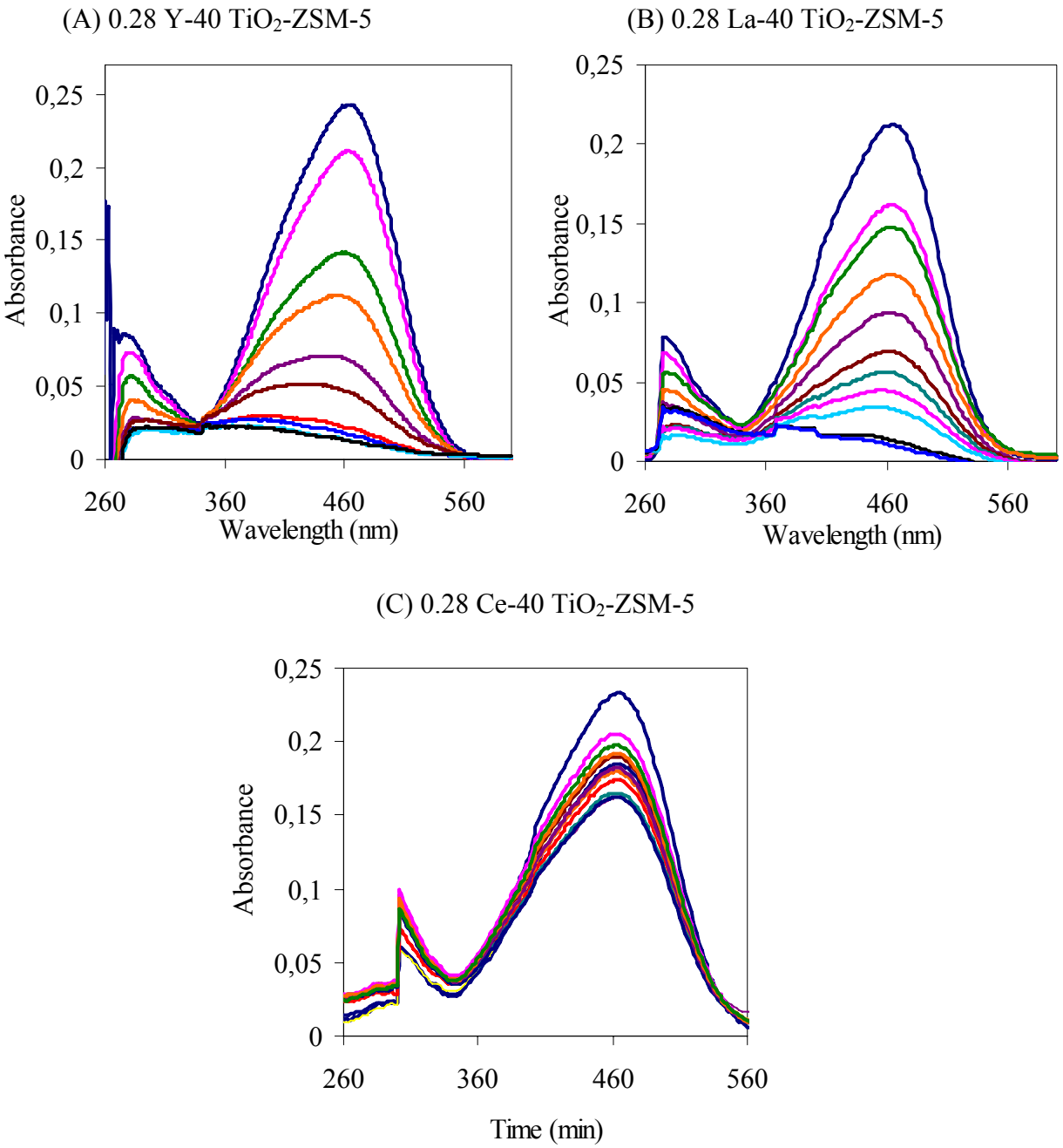

Figure 4.22. UV-Vis spectrum of MeO degradation in the presence of (A) 0.28 Y-40 TiO_2-ZSM-5, (B) 0.28 La-40 TiO_2-ZSM-5, (C) 0.28 Ce-40 TiO_2-ZSM-5. Conditions: pH= 5.85 (Natural), [MeO]= 3.27 mg/L, I= 4.7×10^{15} photons/s, T=298 K, Flow rate= 2000 rpm.

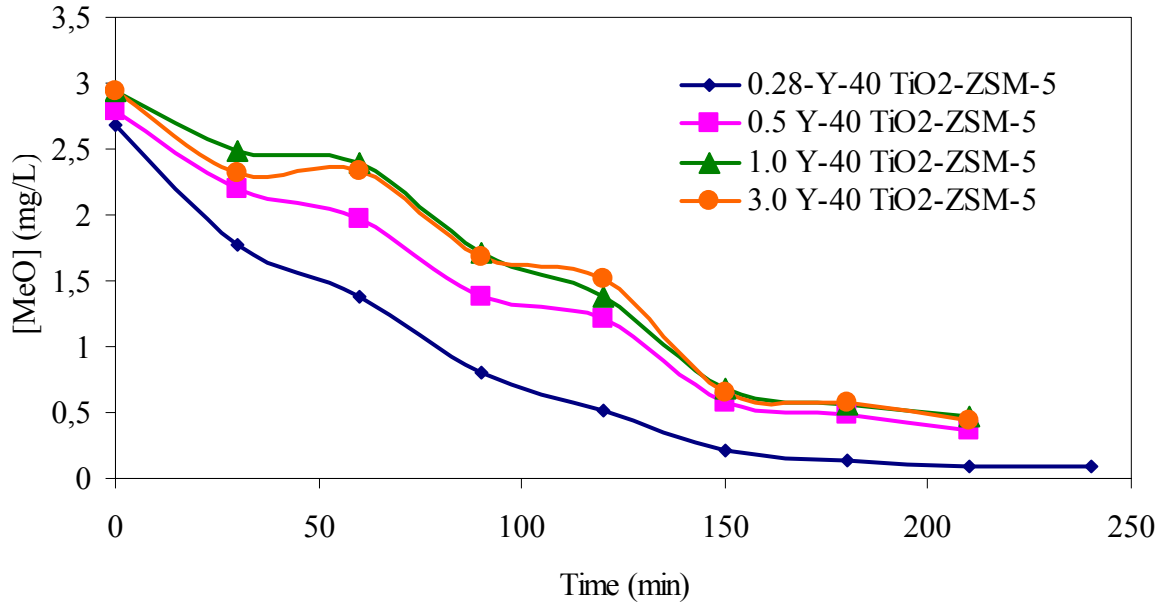

Figure 4.23. Photocatalytic degradation of MeO in the presence of 0.28 Y-40 TiO_2-ZSM-5, 0.50 Y-40 TiO_2-ZSM-5, 1.00 Y-40 TiO_2-ZSM-5 and 3.00 Y-40 TiO_2-ZSM-5 catalysts. Conditions: pH= 5.85 (Natural), [MeO]= 3.27 mg/L, I= $4.7x10^{15}$ photons/s, T=298 K, Flow rate= 2000rpm

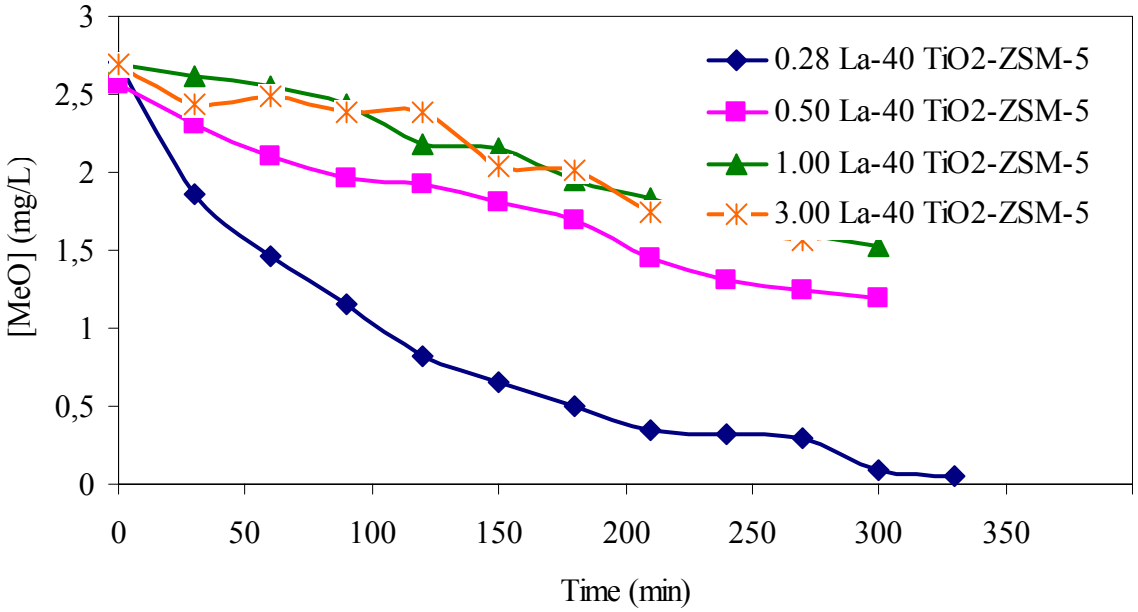

Figure 4.24. Photocatalytic degradation of MeO in the presence of 0.28 La-40 TiO_2-ZSM-5, 0.50 Y-40 TiO_2-ZSM-5, 1.00 Y-40 TiO_2-ZSM-5 and 3.00 Y-40 TiO_2-ZSM-5 catalysts. Conditions: pH= 5.85 (Natural), [MeO]= 3.27 mg/L, I= $4.7x10^{15}$ photons/s, T=298 K, Flow rate= 2000 rpm

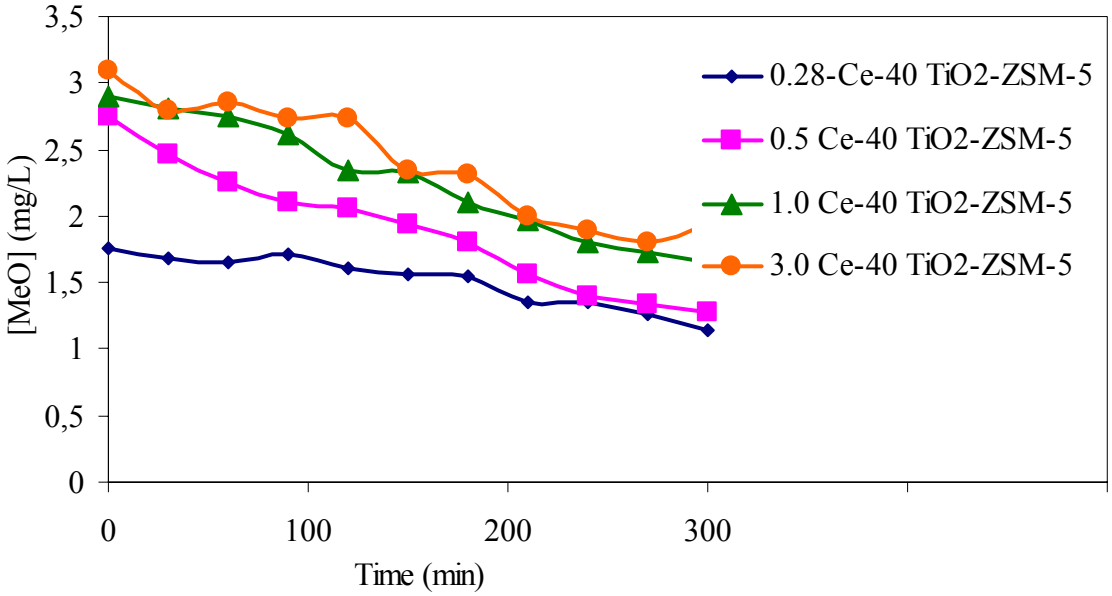

Figure 4.25. Photocatalytic degradation of MeO in the presence of 0.28 Ce-40 TiO_2-ZSM-5, 0.50 Ce-40 TiO_2-ZSM-5, 1.00 Ce-40 TiO_2-ZSM-5 and 3.00 Ce-40 TiO_2-ZSM-5 catalysts. Conditions: pH= 5.85 (Natural), [MeO]= 3.27 mg/L, I= $4.7x10^{15}$ photons/s, T=298 K, Flow rate= 2000 rpm

ZSM-5 and all supported catalysts are controlled at different pH values for 2 h at 10 min intervals (Figure 4.27 - Figure 4.31). It is observed that MeO concentrations remaining in the solution, after 30 min., do not reveal a significant variation for all pH values studied. Also, for ZSM-5 and for all supported catalysts, at acidic pH values (pH=2.7, 4.5 and 5.85 (Natural)) adsorption of MeO is found to be higher compared to that adsorbed at basic pH values (pH=9.0 and 11.0).

For all catalysts at different pH values, MeO concentration values before and after 30 min. dark adsorption are given in Table 4.13 and Table 4.14. Figure 4.32 - Figure 4.36 show photodegradation of MeO after 30 min. dark adsorption in the presence of ZSM-5, 40-TiO_2-ZSM-5, 0.28 Y-40-TiO_2-ZSM-5, 0.28 La-40-TiO_2-ZSM-5 and 0.28 Ce-40-TiO_2-ZSM-5. It is noticed that raw ZSM-5 alone does not participate in the photodegradation of MeO. Catalysts that contain TiO_2 nanoparticles and also Y_2O_3, La_2O_3 or Ce_2O_3 nanoparticles reveal higher

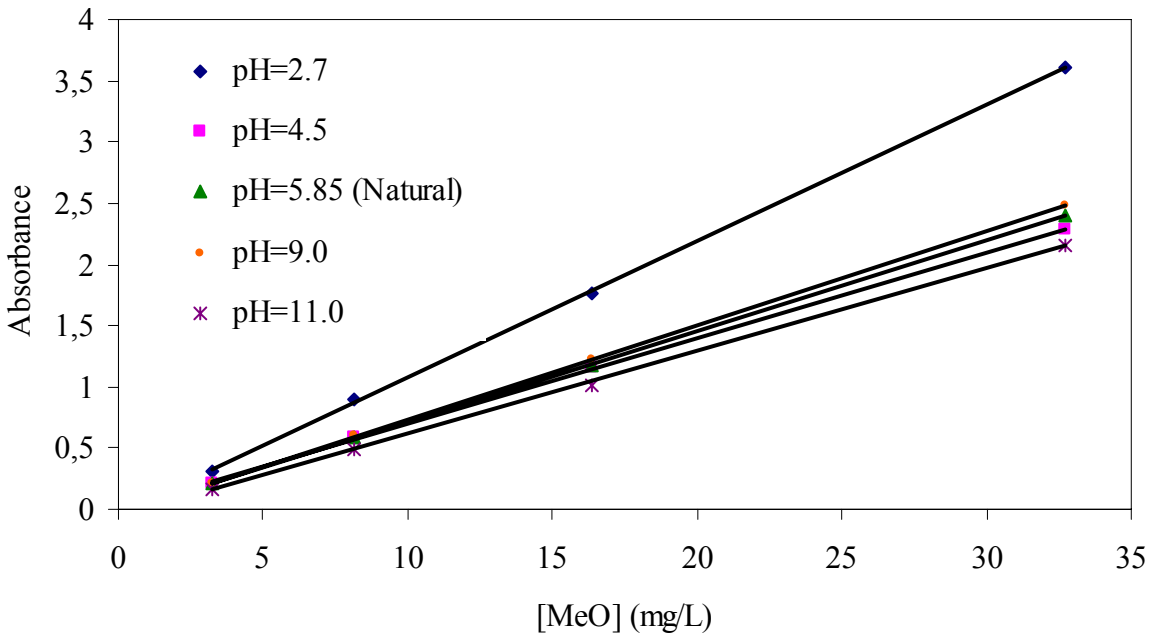

Figure 4.26. Calibration of UV-Vis spectroscopy in the pH range of 2.7-11.
Conditions: [MeO]= 3.27 mg/L, I= 4.7×10^{15} photons/s, T=298 K,
Flow rate= 2000 rpm

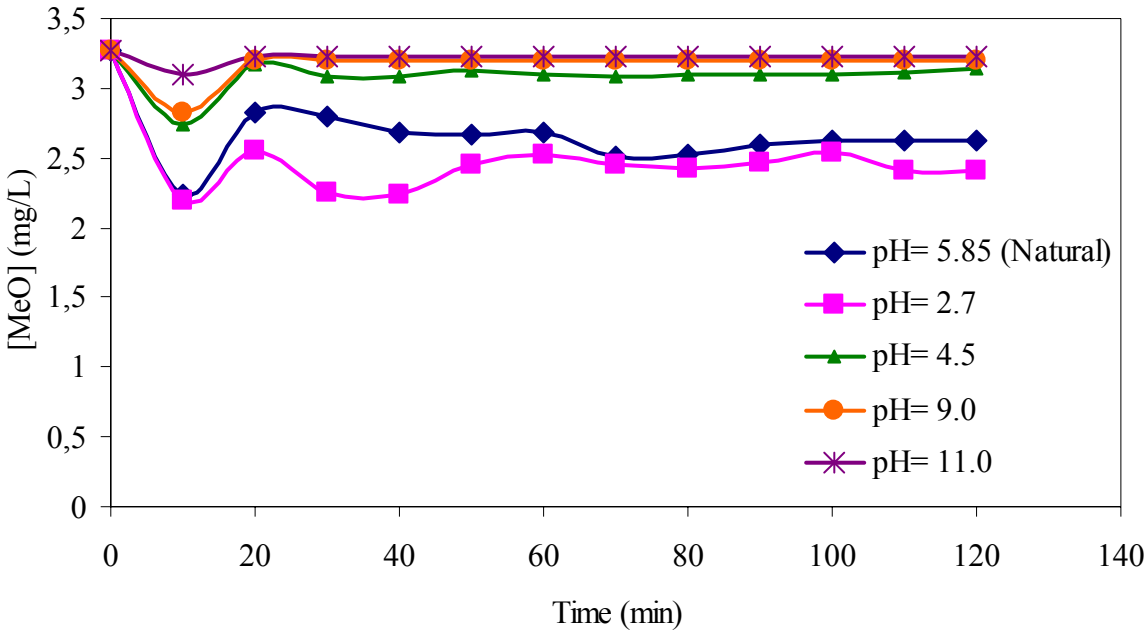

Figure 4.27. Dark adsorption of MeO in the presence of ZSM-5.
Conditions: [MeO]= 3.27 mg/L, I= 4.7×10^{15} photons/s, T=298 K,
Flow rate= 2000 rpm

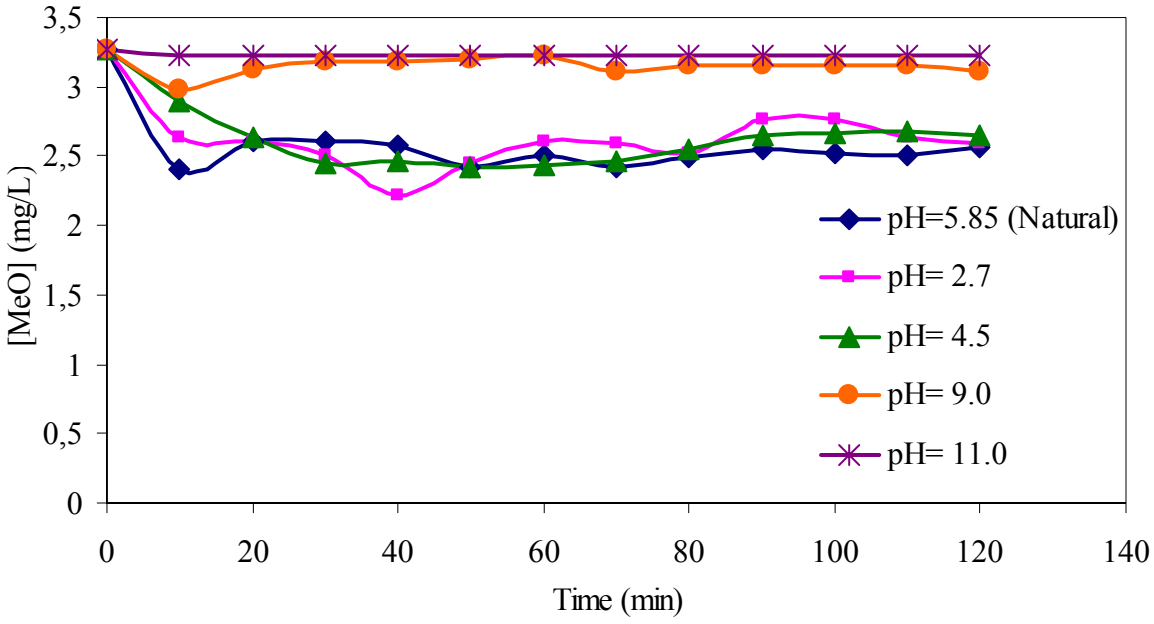

Figure 4.28. Dark adsorption of MeO in the presence of 40-TiO_2-ZSM-5.
Conditions: [MeO]= 3.27 mg/L, I= $4.7x10^{15}$ photons/s, T=298 K,
Flow rate= 2000 rpm

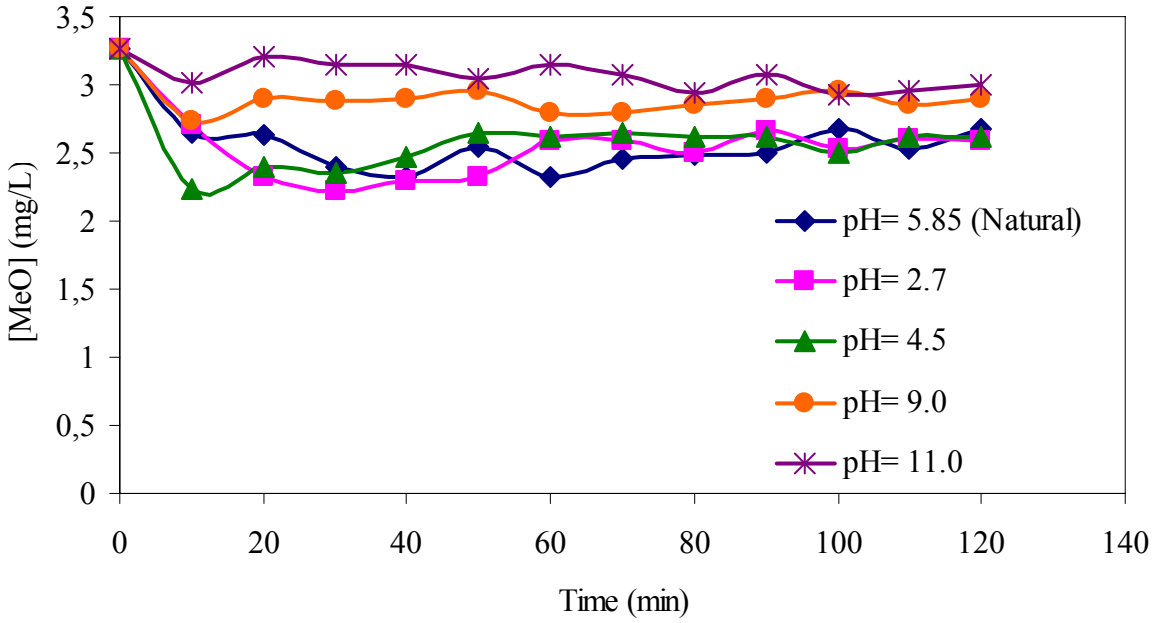

Figure 4.29. Dark adsorption of MeO in the presence of 0.28 Y-40-TiO_2-ZSM-5.
Conditions: [MeO]= 3.27 mg/L, I= $4.7x10^{15}$ photons/s, T=298 K,
Flow rate= 2000 rpm

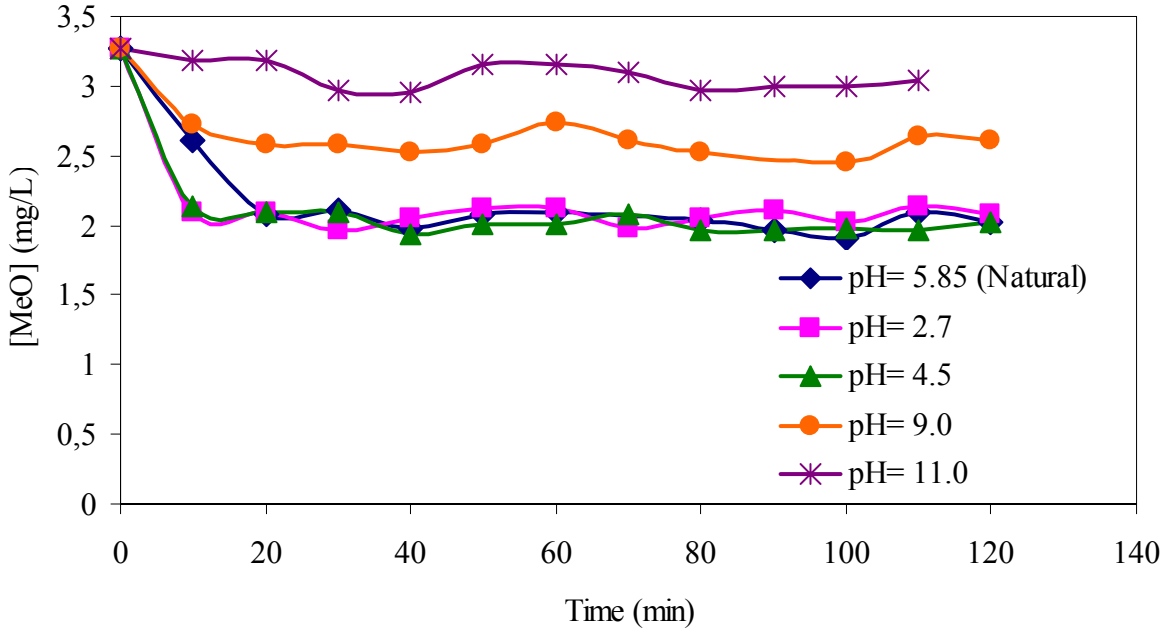

Figure 4.30. Dark adsorption of MeO in the presence of 0.28 La-40-TiO_2-ZSM-5. Conditions: [MeO]= 3.27 mg/L, I= $4.7x10^{15}$ photons/s, T=298 K, Flow rate= 2000 rpm

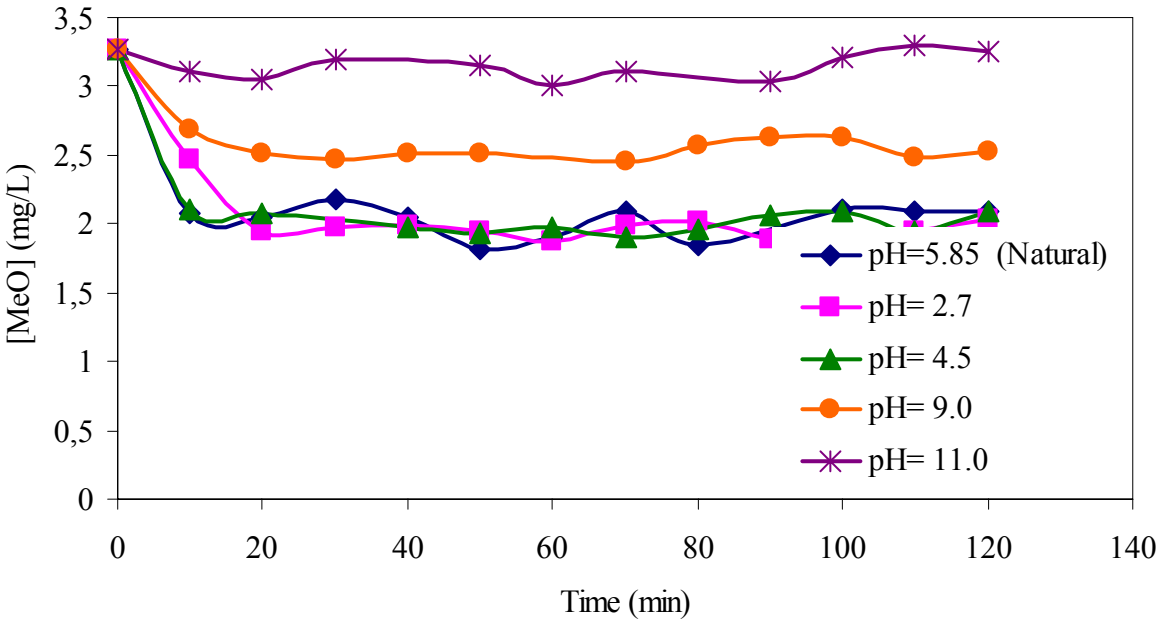

Figure 4.31. Dark adsorption of MeO in the presence of 0.28 Ce-40-TiO_2-ZSM-5. Conditions: [MeO]= 3.27 mg/L, I= $4.7x10^{15}$ photons/s, T=298 K, Flow rate= 2000 rpm

efficiencies for the photodegradation of MeO. In addition, maximum degradation of MeO is achieved at acidic pH values. This result is being in consistency with the dark adsorption experiments.

Table 4.13. Concentration of MeO before dark adsorption (C_i) and after dark adsorption (C_0) in the presence of ZSM-5 and 40 TiO_2-ZSM-5at different pH values

Catalysts	C_i (mg/L)	C_0 (mg/L)
ZSM-5		
pH= 2.7	3.27	2.20
pH= 4.5	3.27	2.74
pH= 5.85	3.27	2.24
pH= 9.0	3.27	2.82
pH= 11.0	3.27	3.09
40 TiO_2-ZSM-5		
pH= 2.7	3.27	2.63
pH= 4.5	3.27	2.90
pH= 5.85	3.27	2.40
pH= 9.0	3.27	2.98
pH= 11.0	3.27	3.23

Table 4.14. Concentration of MeO before dark adsorption (C_i) and after dark adsorption (C_0) in the presence of 0.28 Y-40 TiO_2-ZSM-5, 0.28 La-40 TiO_2-ZSM-5 and 0.28 Ce-40 TiO_2-ZSM-5 at different pH values

Catalysts	C_i (mg/L)	C_0 (mg/L)
0.28 Y-40 TiO_2-ZSM-5		
pH= 2.7	3.27	2.21
pH= 4.5	3.27	2.23
pH= 5.85	3.27	2.65
pH= 9.0	3.27	2.66
pH= 11.0	3.27	3.02
0.28 La-40 TiO_2-ZSM-5		
pH= 2.7	3.27	2.10
pH= 4.5	3.27	2.14
pH= 5.85	3.27	2.60
pH= 9.0	3.27	2.73
pH= 11.0	3.27	3.18
0.28 Ce-40 TiO_2-ZSM-5		
pH= 2.7	3.27	2.30
pH= 4.5	3.27	2.34
pH= 5.85	3.27	2.60
pH= 9.0	3.27	2.73
pH= 11.0	3.27	3.10

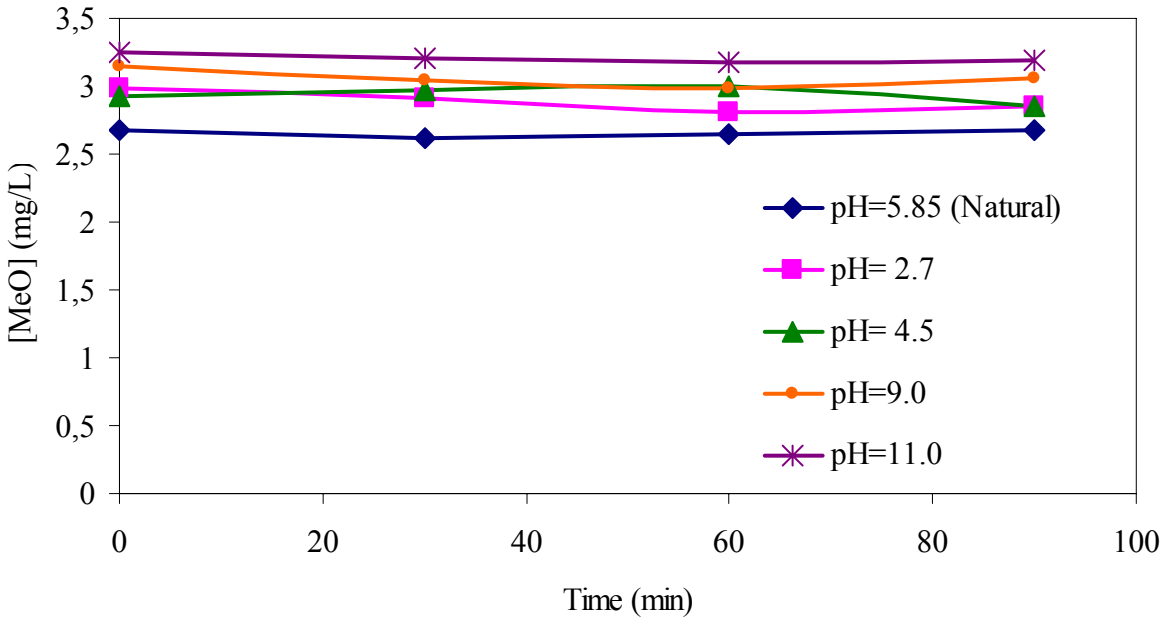

Figure 4.32. Photodegradation of MeO in the presence of ZSM-5 at different pH values Conditions: [MeO]= 3.27 mg/L, I= 4.7×10^{15} photons/s, T=298 K, Flow rate= 2000 rpm

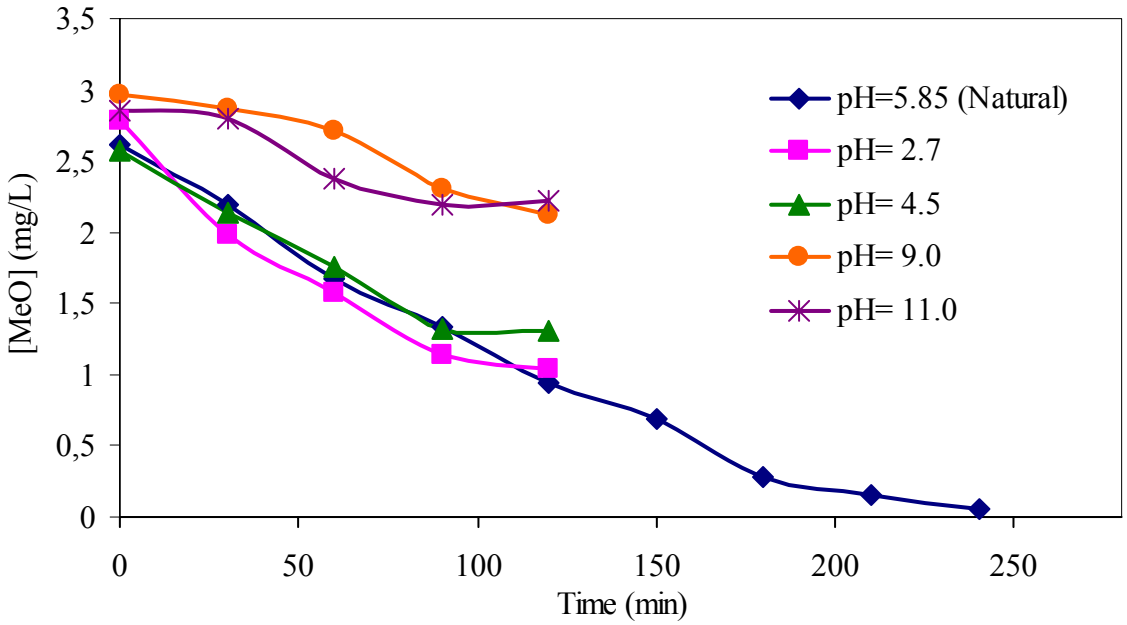

Figure 4.33. Photodegradation of MeO in the presence of 40-TiO_2-ZSM-5 at different pH values. Conditions: [MeO]= 3.27 mg/L, I= 4.7×10^{15} photons/s, T=298 K, Flow rate= 2000 rpm

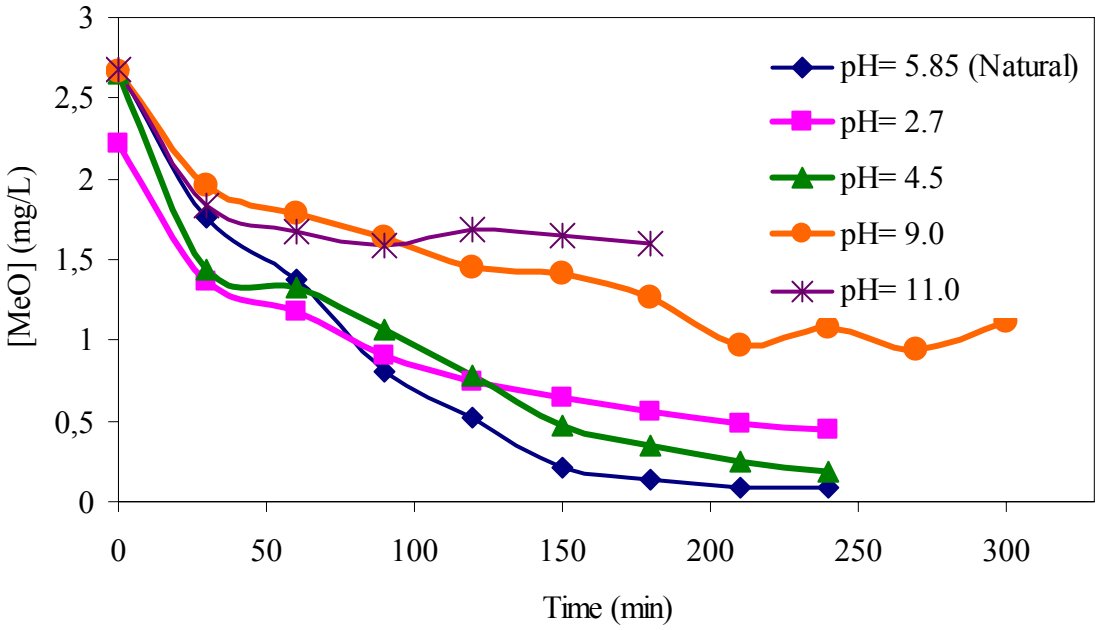

Figure 4.34. Photodegradation of MeO in the presence of 0.28 Y-40 TiO_2-ZSM-5 at different pH values. Conditions: [MeO]= 3.27 mg/L, I= $4.7x10^{15}$ photons/s, T=298 K, Flow rate= 2000 rpm

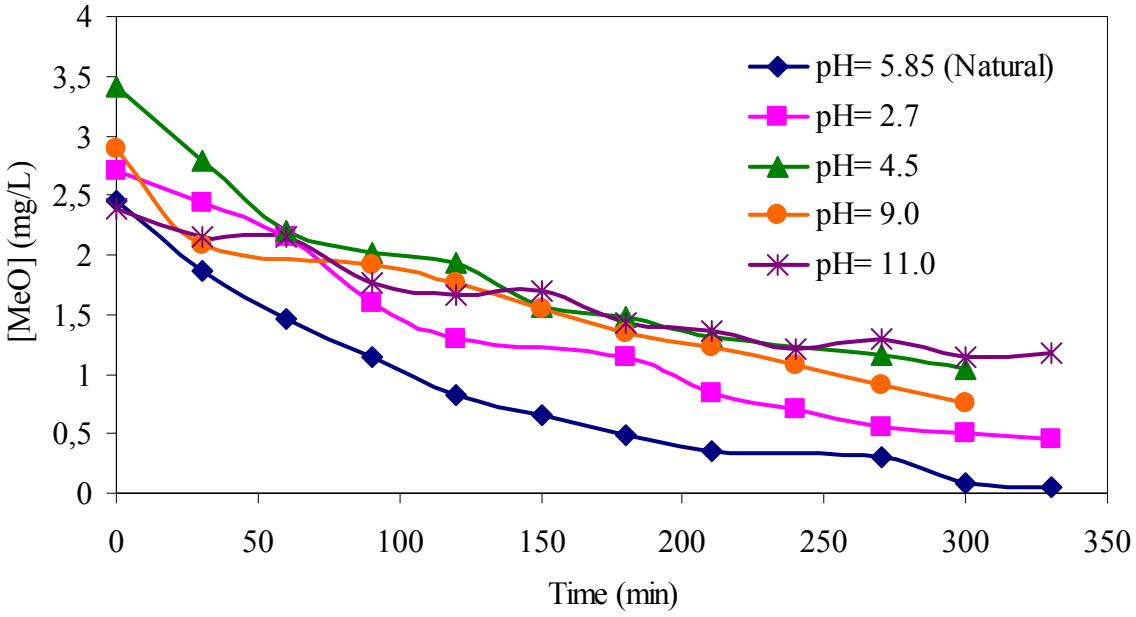

Figure 4.35. Photodegradation of MeO in the presence of 0.28 La-40 TiO_2-ZSM-5 at different pH values. Conditions: [MeO]= 3.27 mg/L, I= $4.7x10^{15}$ photons/s, T=298 K, Flow rate= 2000 rpm

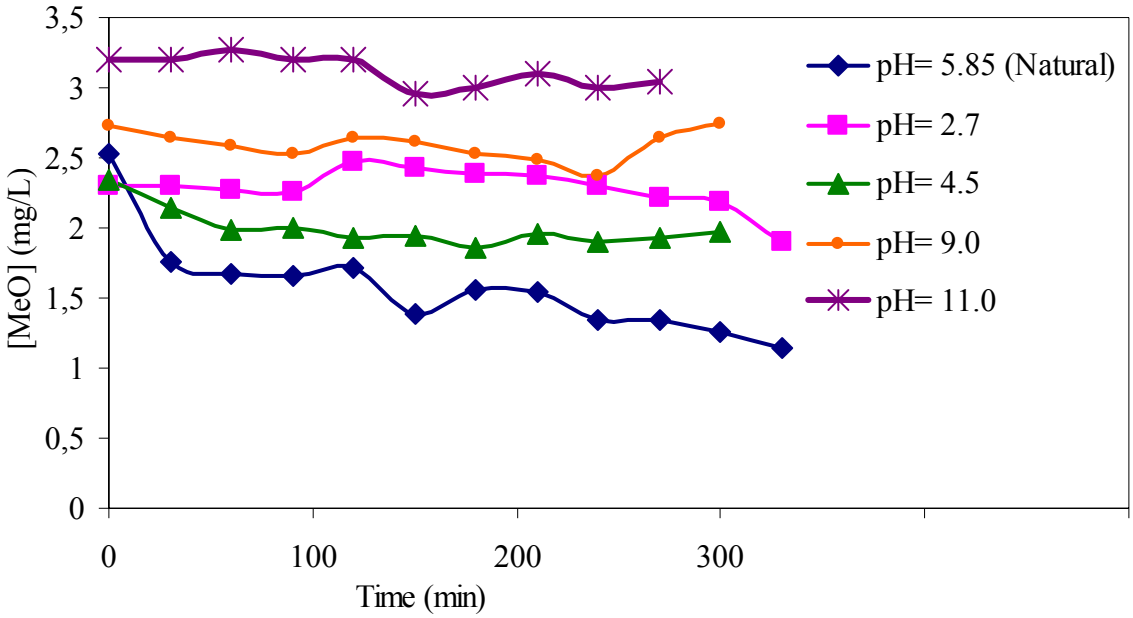

Figure 4.36. Photodegradation of MeO in the presence of 0.28 Ce-40 TiO_2-ZSM-5 at different pH values. Conditions: [MeO]= 3.27 mg/L, I= $4.7x10^{15}$ photons/s, T=298 K, Flow rate= 2000 rpm

All these results indicate that there is a strong dependence on the pH of zero point-charge (pH_{zpc}) of TiO_2 for all supported catalysts. It is known that (pH_{zpc}) for TiO_2 is equal to 6.80 [52]. At pH < pH_{zpc} and at pH > pH_{zpc}, adsorption capacity of the catalysts varies and this can be attributed both to the surface ionization of TiO_2 particles in water and negatively charged sulfonic group existing on the MeO structure. The following surface reactions for the supported catalysts are expected to occur at different pH values:

$$\text{at } pH<pH_{zpc}: \qquad TiOH + H^+ \rightarrow TiOH_2^+ \tag{4.1}$$

$$\text{at } pH>pH_{zpc}: \qquad TiOH + OH^- \rightarrow TiO^- + H_2O \tag{4.2}$$

where TiOH is the surface 'titanol' group. Thus, at pH<pH_{zpc}, attractive forces between the TiO_2 surface and the dye will favour adsorption. Accordingly, all catalysts show a rather good photocatalytic activity at low pH values. On the other hand, at pH>pH_{zpc}, the TiO_2 surface is

negatively charged and repulsive forces between the TiO_2 surface and the dye lead to a lower adsorption. The decrease in degradation efficiency of the catalysts is as a result of this poor adsorption at high pH values.

4.4.4. Effect of MeO Concentration

The effect of initial MeO concentration on the photocatalytic degradation has been investigated from 32.7 mg/L to 0.81 mg/L in the presence of 0.28 Y-40 TiO_2-ZSM-5, 0.28 La-40 TiO_2-ZSM-5 and 0.28 Ce-40 TiO_2-ZSM-5 (Figure 4.37-Figure 4.39). For each of the catalysts, it is noticed that degradation rate increases with the increase of MeO concentration to a certain concentration and a further increase leads to a decrease in the MeO degradation rate. The decrease of degradation as the MeO concentration increases due to the fact that the latter gets adsorbed on the supported catalysts. This adsorbed MeO blocks photocatalytically active centers and prevents their interaction with photons of the light, thus resulting in a decrease in efficiency of degradation.

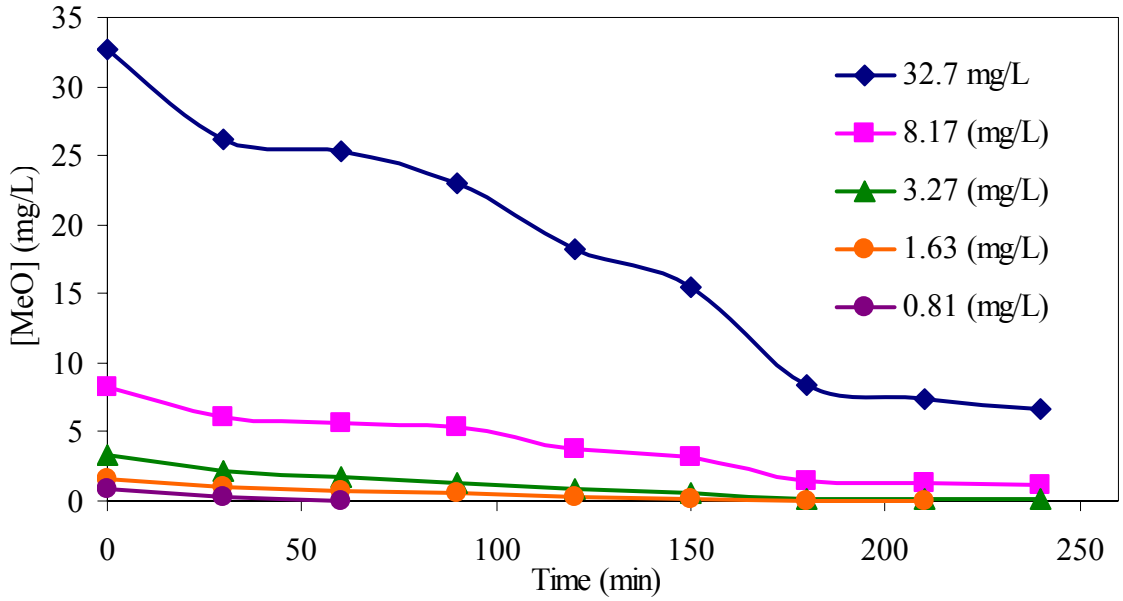

Figure 4.37. Photodegradation of MeO in the presence of 0.28 Y-40 TiO_2-ZSM-5 at different initial MeO concentrations. Conditions: pH= 5.85 (Natural), I= 4.7×10^{15} photons/s, T=298 K, Flow rate= 2000 rpm

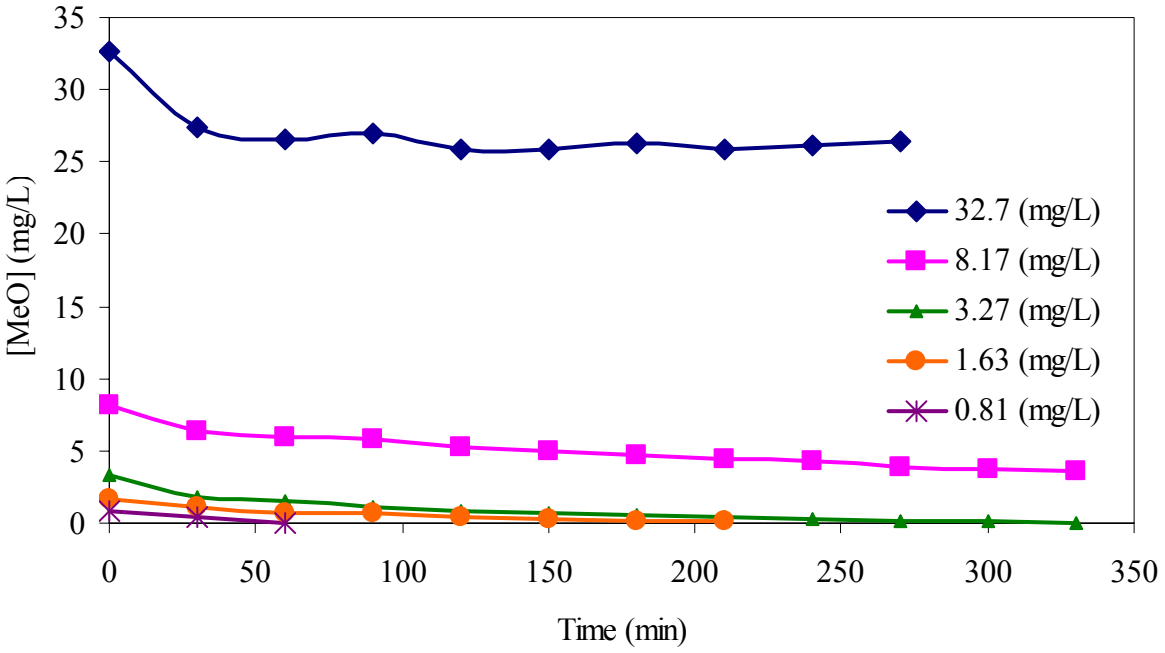

Figure 4.38. Photodegradation of MeO in the presence of 0.28 La-40 TiO_2-ZSM-5 at different initial MeO concentrations. Conditions: pH= 5.85 (Natural), I= $4.7x10^{15}$ photons/s, T=298 K, Flow rate= 2000 rpm

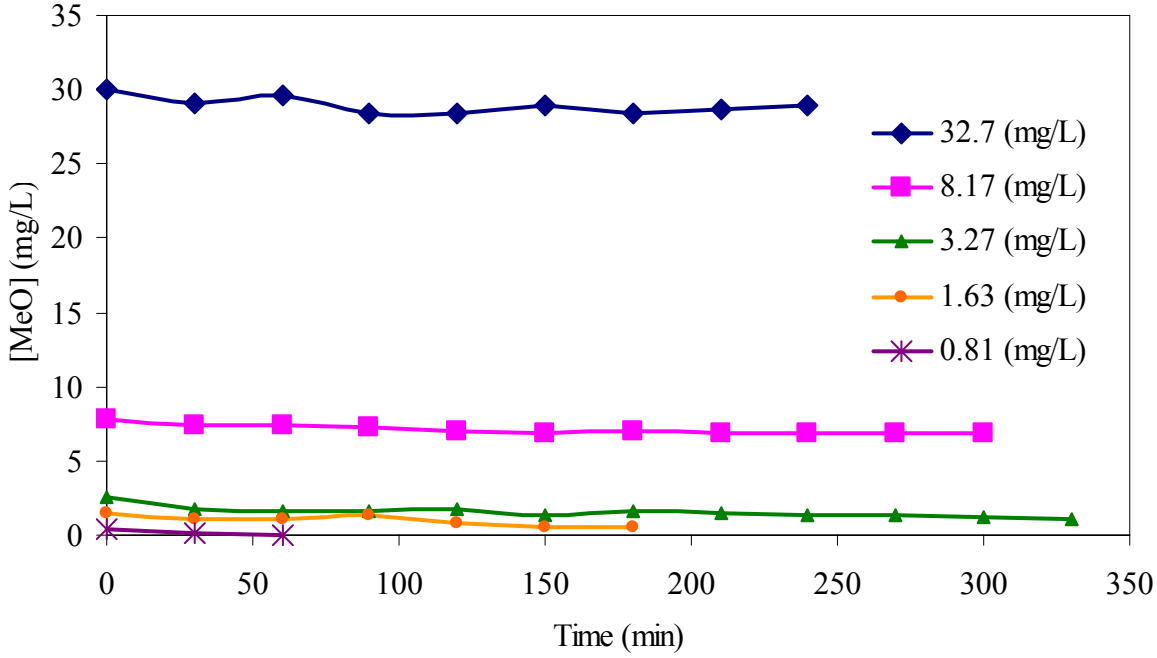

Figure 4.39. Photodegradation of MeO in the presence of 0.28 Ce-40 TiO_2-ZSM-5 at different initial MeO concentrations. Conditions: pH= 5.85 (Natural), I= $4.7x10^{15}$ photons/s, T=298 K, Flow rate= 2000 rpm

The photocatalytic degradation of MeO is examined by following the rate expression given in equation (4.3).

$$\text{Rate} = \frac{-dC}{dt} = k_{app} C \tag{4.3}$$

where k_{app} is the apparent rate constant. The integration of the equation yields equation (4.4):

$$\ln\left(\frac{C_0}{C}\right) = k_{app} t \tag{4.4}$$

where C_0 is the equilibrium concentration of MeO after dark adsorption, C is the remaining concentration in solution by time and k_{app} is the apparent rate constant The linear trend observed in Figure 4.40, Figure 4.41 and Figure 4.42 proves that initial the photocatalytic degradation of MeO at the conditions of reactions follows first order kinetics. The apparent rate-constants hence calculated (slopes of the lines) and regression values are also shown in Table 4.15.

The kinetics of heterogeneous photocatalytic processes are also analyzed by using Langmuir-Hinshelwood model [53]. The following assumptions are accepted for Langmuir-Hinshelwood model: (i) Adsorption cannot proceed beyond monolayer coverage, (ii) All sites are equivalent and the surface is uniform, (iii) The ability of a molecule to adsorb at a given site is independent of the occupation of neighboring sites (that is, there are no interactions between adsorbed molecules) [17].

Table 4.15. Apparent first order rate constants (k_{app}) for the photocatalytic degradation of MeO at different initial concentrations after dark adsorption (C_0) and linear regression values

Catalysts	C_0 (mg/L)	k_{app} (min^{-1})	R
0.28 Y-40 TiO_2-ZSM-5			
32.7 (mg/L)	26.12	2.5x10^{-}3	0.9825
8.17 (mg/L)	6.11	0.0093	0.9346
3.27 (mg/L)	2.11	0.0177	0.9833
1.63 (mg/L)	1.07	0.0241	0.9444
0.81 (mg/L)	0.33	0.0286	1.0000
0.28 La-40 TiO_2-ZSM-5			
32.7 (mg/L)	27.35	5.88x10^{-}4	0.9765
8.17 (mg/L)	6.40	0.0020	0.9943
3.27 (mg/L)	2.21	0.0051	0.9583
1.63 (mg/L)	1.12	0.0123	0.9052
0.81 (mg/L)	0.35	0.0186	1.000
0.28 Ce-40 TiO_2-ZSM-5			
32.7 (mg/L)	30.00	5.17x10^{-}4	0.9870
8.17 (mg/L)	8.00	0.0023	0.9904
3.27 (mg/L)	2.17	0.0052	0.9642
1.63 (mg/L)	1.47	0.0053	0.6167
0.81 (mg/L)	0.46	0.0125	1.000

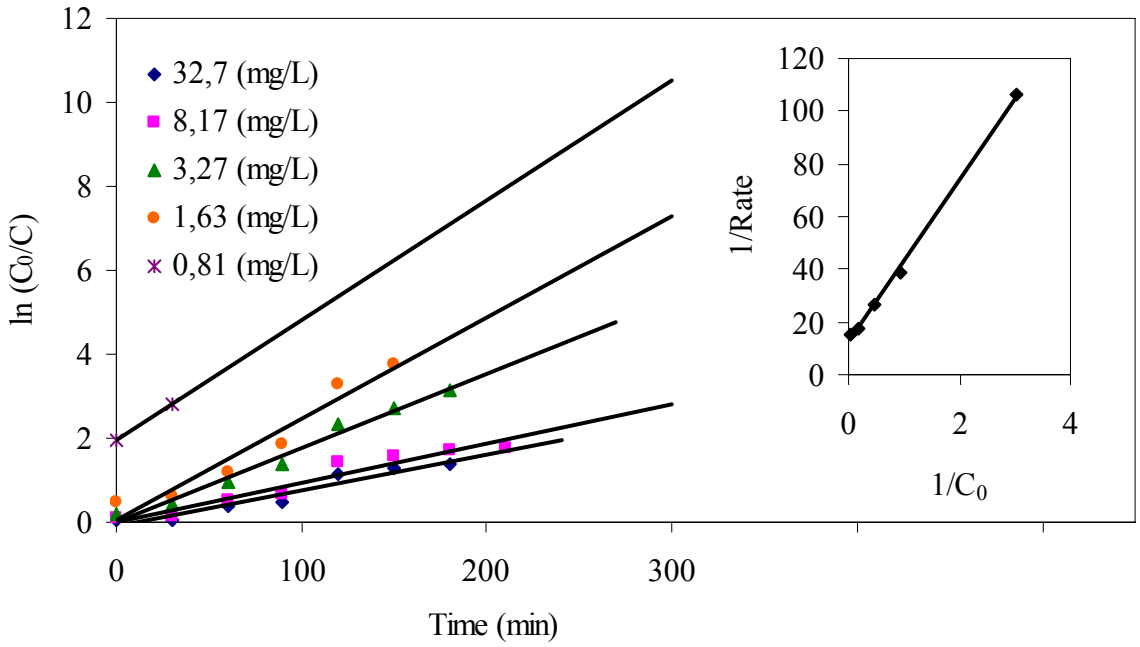

Figure 4.40. ln (C_o/C) vs. time plot in the presence of 0.28 Y-40 TiO_2-ZSM-5. Inset: 1/R vs. $1/C_o$ plot in the presence of 0.28 Y-40 TiO_2-ZSM-5. Conditions: pH= 5.85 (Natural), I= $4.7x10^{15}$ photons/s, T=298 K, Flow rate= 2000 rpm

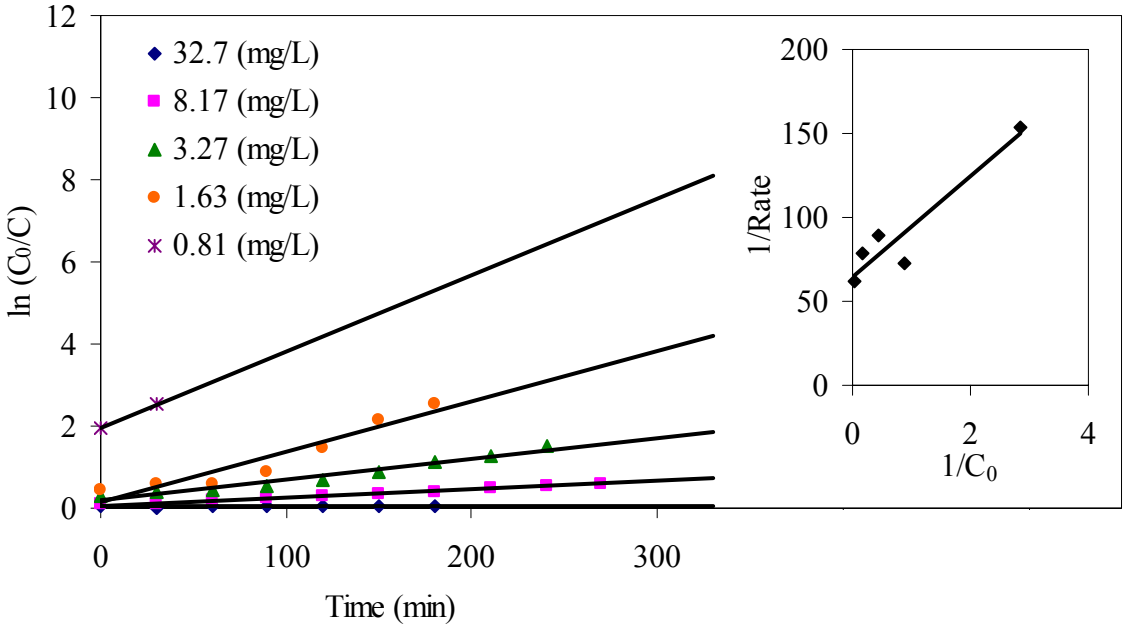

Figure 4.41. ln (C_o/C) vs. time plot in the presence of 0.28 La-40 TiO_2-ZSM-5. Inset: 1/R vs. $1/C_o$ plot in the presence of 0.28 La-40 TiO_2-ZSM-5.Conditions: pH= 5.85 (Natural), I= $4.7x10^{15}$ photons/s, T=298 K, Flow rate= 2000 rpm

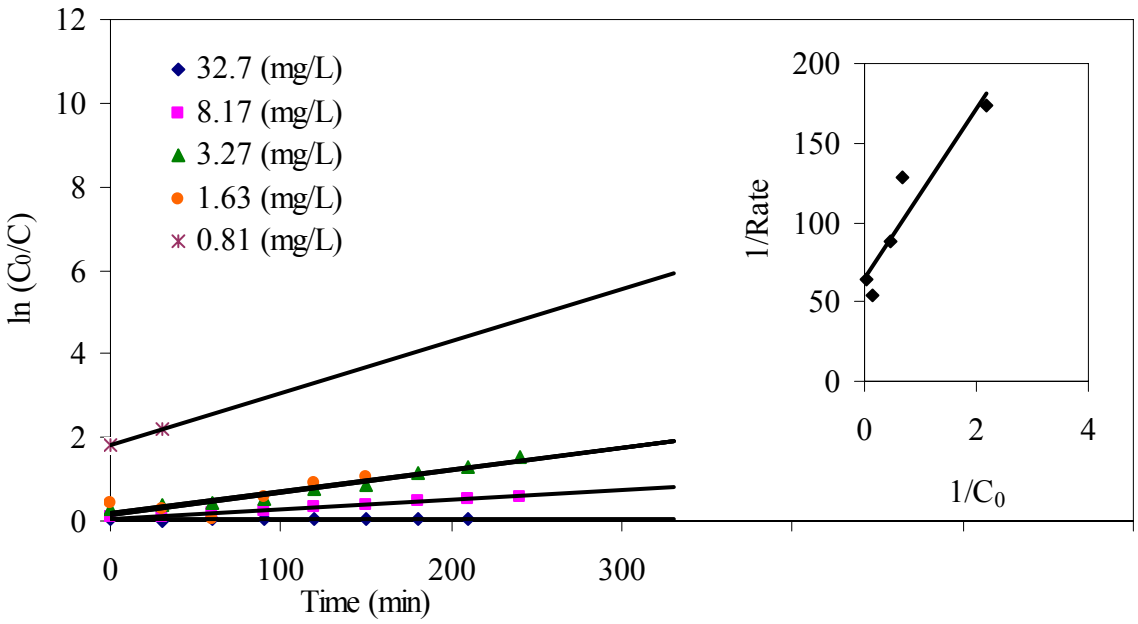

Figure 4.42. ln (C_o/C) vs. time plot in the presence of 0.28 Ce-40 TiO_2-ZSM-5. Inset: 1/R vs. $1/C_o$ plot in the presence of 0.28 Ce-40 TiO_2-ZSM-5. Conditions: pH= 5.85 (Natural), I= 4.7×10^{15} photons/s, T=298 K, Flow rate= 2000 rpm

The model is also rationalized for our experimental results. The surface coverage (θ) of catalysts is given by the following equation (4.5):

$$\theta = \frac{KC_t}{1 + KC_t + \sum_i K_i C_i} \qquad (4.5)$$

where *i* refers to the each of various intermediates during MeO degradation, C_t is the remaining concentration of MeO in solution by time, *t* is the time of reaction, *k* is the reaction constant, *K* and K_i are adsorption constants of MeO and intermediates, respectively. If it is assumed that the adsorption constants for all organic intermediate molecules present in the reacting mixture are equal, the following assumption can be made and given in equation (4.6):

$$KC_t + \sum_i K_i C_i = K\,C_t \tag{4.6}$$

Thus, rate expression becomes

$$\text{Rate} = k_r\theta = \frac{k_r K C_t}{1 + K C_t} = k_{app} C_t \tag{4.7}$$

From equation 4.7, the rate (R) can be written as

$$\frac{1}{\mathrm{R}} = \frac{1 + \mathrm{KC_t}}{\mathrm{k_r KC_t}} \tag{4.8}$$

This equation can be rearranged as

$$\frac{1}{\mathrm{k_{app} C_t}} = \frac{\mathrm{KC_t}}{\mathrm{KC_t k_r}} + \frac{1}{\mathrm{k_r C_t K}} \tag{4.9}$$

And finally, equation 4.10 is obtained by substitution of C_o in place of C_t as the equilibrium concentration of MeO after dark adsorption.

$$\frac{1}{R} = \frac{1}{k_{app} C_0} = \frac{1}{\mathrm{k_r KC_0}} + \frac{1}{\mathrm{k_r}} \tag{4.10}$$

Thus, the applicability of Langmuir-Hinshelwood equation for the degradation has been confirmed by the linear plot obtained by plotting the reciprocal of 1/R against $1/C_0$ as shown in the insets of Figure 4.40, Figure 4.41 and Figure 4.42. Table 4.16 shows adsorption rate constants (K) and reaction rate constants (k_r) of the supported catalysts.

Table 4.16. Adsorption constants (K) and rate constants (k_r) of the supported catalysts

Catalysts	K_{ads} ($mg^{-1}L$)	k_r (mg/L min)
0.28 Y-40 TiO_2-ZSM-5	0.407	0.0800
0.28 La-40 TiO_2-ZSM-5	2.188	0.0150
0.28 Ce-40 TiO_2-ZSM-5	1.204	0.0150

4.4.5. Effect of Heat Treatment

In order to investigate the effect of higher calcination temperatures, degradation experiments are also followed in the presence of 40-TiO_2 (1000^{o}C), 40-TiO_2-ZSM-5 (1000^{o}C), 0.28 Y-40 TiO_2-ZSM-5 (1000^{o}C), 0.28 La-40 TiO_2-ZSM-5 (1000^{o}C), 0.28 Ce-40 TiO_2-ZSM-5 (1000^{o}C) (Figure 4.43 -Figure 4.47). Table 4.17 represents MeO concentration remaining in solution after 30 min dark adsorption. It is noticed that for the catalysts prepared at 400^{o}C, lower concentration of MeO remain in solution, i.e., MeO molecules are adsorbed more on the surfaces of these catalysts. Accordingly, degradation performances of the catalysts prepared at 400^{o}C is higher than the ones prepared at 1000^{o}C. This observation is consistent with the results of XRD analysis, where complete conversion of anatase to rutile is observed for catalysts prepared at 1000^{o}C. For degradation processes, rutile phase is not favorable, due to the higher recombination rate of electrons and holes, limited number of hydroxyl groups on the surface and the limited number of oxygen sites.

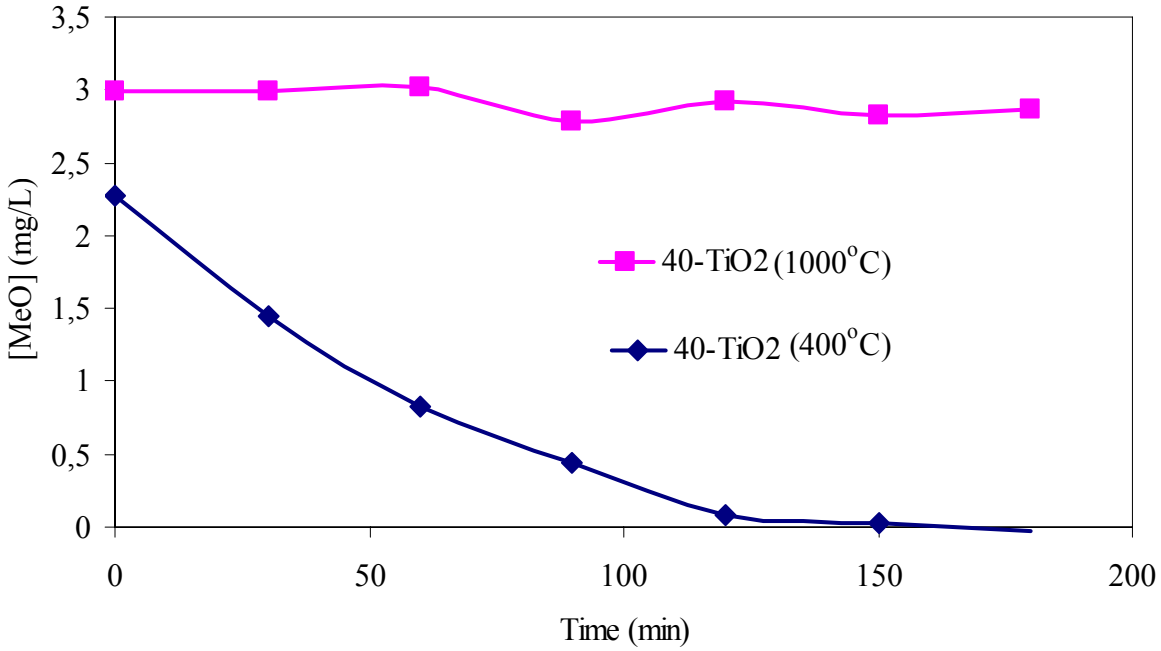

Figure 4.43. Photocatalytic degradation of MeO in the presence of 40-TiO_2 at 400 °C and 1000 °C, Conditions: pH= 5.85 (Natural), [MeO]= 3.27 mg/L, I= $4.7x10^{15}$ photons/s, T=298 K, Flow rate= 2000 rpm

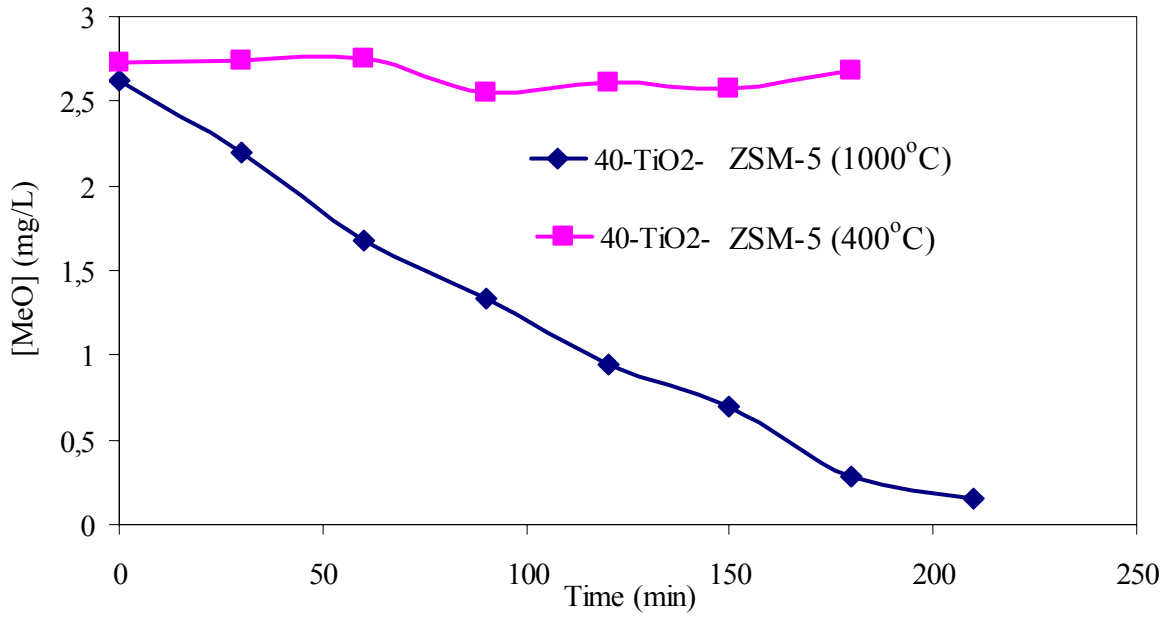

Figure 4.44. Photocatalytic degradation of MeO in the presence of 40-TiO_2-ZSM-5 at 400 °C and 1000 °C, Conditions: pH= 5.85 (Natural), [MeO]= 3.27 mg/L, I= $4.7x10^{15}$ photons/s, T=298 K, Flow rate= 2000 rpm

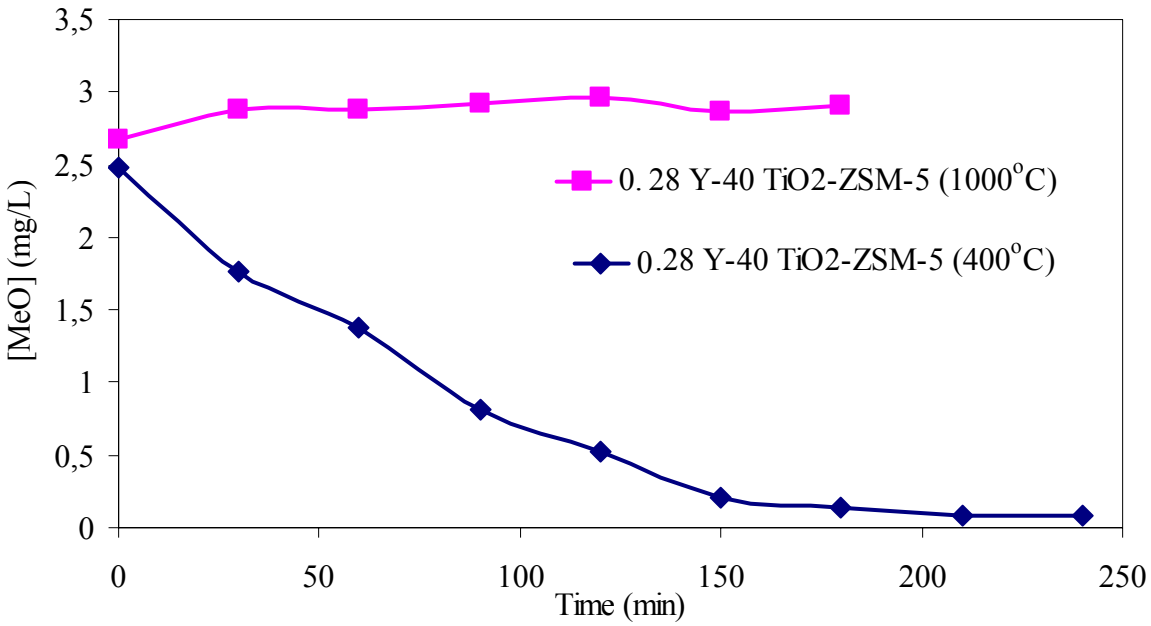

Figure 4.45. Photocatalytic degradation of MeO in the presence of 0.28 Y-40 TiO_2-ZSM-5 at 400 °C and 1000 °C, Conditions: pH= 5.85 (Natural), [MeO]= 3.27 mg/L, I= $4.7x10^{15}$ photons/s, T=298 K, Flow rate= 2000 rpm

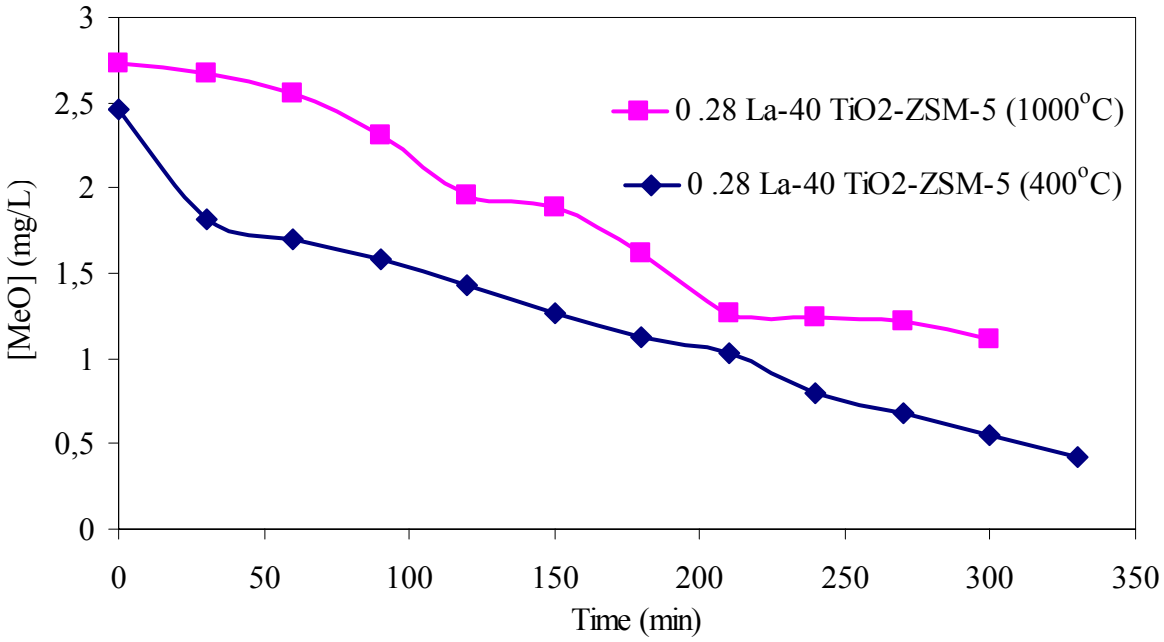

Figure 4.46. Photocatalytic degradation of MeO in the presence of 0.28 La-40 TiO_2-ZSM-5 at 400 °C and 1000 °C, Conditions: pH= 5.85 (Natural), [MeO]= 3.27 mg/L, I= $4.7x10^{15}$ photons/s, T=298 K, Flow rate= 2000 rpm

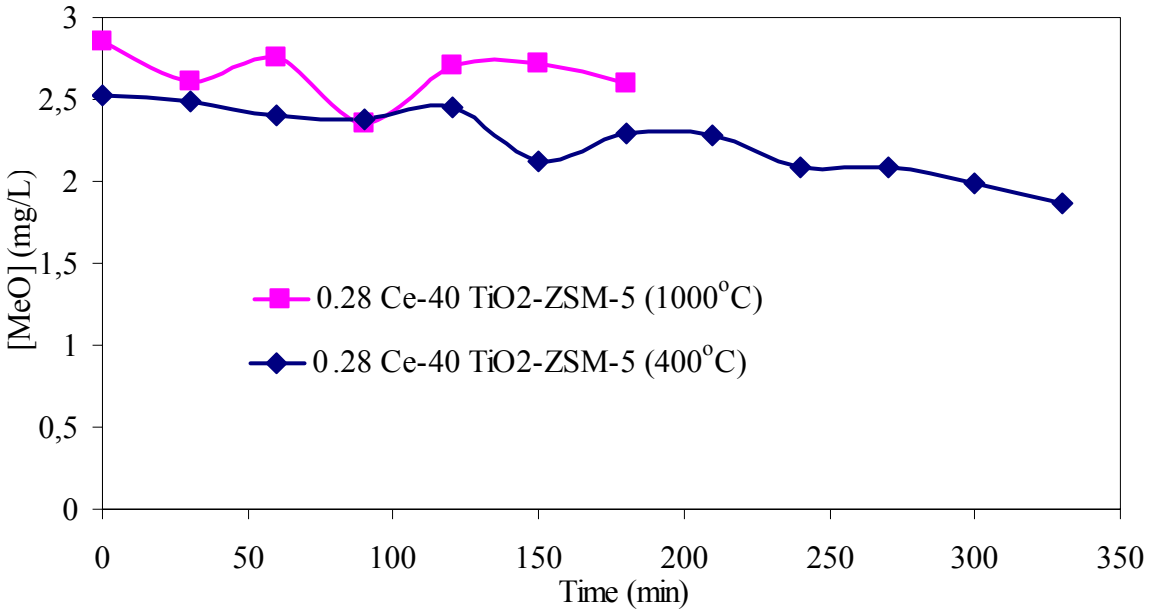

Figure 4.47. Photocatalytic degradation of MeO in the presence of 0.28 Ce-40 TiO_2-ZSM-5 at 400 °C and 1000 °C, Conditions: pH= 5.85 (Natural), [MeO]= 3.27 mg/L, I= $4.7x10^{15}$ photons/s, T=298 K, Flow rate= 2000 rpm

Table 4.17. Concentration of MeO before dark adsorption (C_i) and after dark adsorption (C_0)

Catalysts	C_i (mg/L)	C_0 (mg/L)
40-TiO_2 (400°C)	3.27	2.27
40-TiO_2 (1000°C)	3.27	2.98
40-TiO_2-ZSM-5 (400°C)	3.27	2.61
40-TiO_2-ZSM-5 (1000°C)	3.27	2.72
0.28 Y-40 TiO_2-ZSM-5 (400°C)	3.27	2.48
0.28 Y-40 TiO_2-ZSM-5 (1000°C)	3.27	2.68
0.28 La-40 TiO_2-ZSM-5 (400°C)	3.27	2.46
0.28 La-40 TiO_2-ZSM-5 (1000°C)	3.27	2.73
0.28 Ce-40 TiO_2-ZSM-5 (400°C)	3.27	2.53
0.28 Ce-40 TiO_2-ZSM-5 (1000°C)	3.27	2.85

4.4.6. Postulated Mechanism for MeO Degradation

Oxidative degradation of azo dyes occurs generally by hydroxyl radicals, known as highly reactive electrophilic oxidants. Main reactions of hydroxyl radicals with these compounds can be addition to the chromophore, addition to the aryl rings, hydrogen abstraction or one electron oxidation [54]. Experimentally proposed degradation mechanisms focus on the cleavage of either the N-N bond resulting in nitrosoaryl intermediates or the C-N bond as shown in Figure 4.48 [55,56].

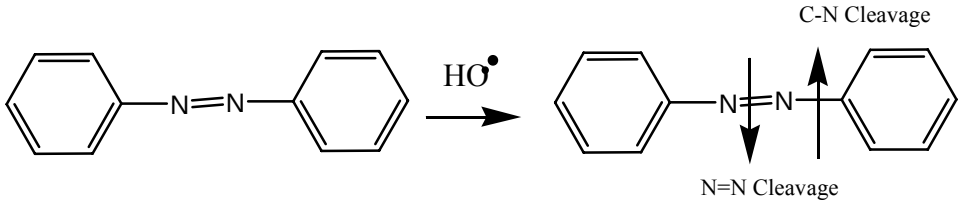

Figure 4.48. Proposed degradation mechanisms of azo dyes

Generally, the sites near the azo bond is the attack area in photocatalytic degradation process, whilst the TiO_2 destruction of the C-N= bond and the N-N bonds leads to fading of the dyes. The identified adducts are either aromatic amine or phenolic compounds. Based on these, though intermediates forming in the photocatalytic degradation process of MeO cannot be identified, the following mechanism is postulated (Figure 4.49).

As an initial hydroxyl attack to the carbon atom bearing the azo bond, benzenesulfonic acid (I), dimethyl aniline (II) and N_2 gas may arise. The electron withdrawing sulphonate group inhibits reactivity towards •OH of the ring that carried it. Thus, the ring with the amino group is the first target for the hydroxyl radicals due to the electron withdrawing effect of sulphonate group and steric hindrance [57]. The reaction proceeds with subsequent attacks of hydroxyl radicals and formation of aniline molecule (IV). The ortho-para directing character of $^{-}NH_2$ produces 4-hydroxyaniline (V). Further hydroxyl radical attacks result in the

formation of molecules VI and VII. MeO and most of the intermediates, benzene derivatives, disappeared during the discolouration stage [58]. Moreover, in the course of the degradation small molecules and inorganic anions are also progressively formed. Although bleaching reaction is very fast, complete mineralization of the dye to yield small molecules, such as CO_2, H_2O and the inorganic anions such as SO_4^{2-} and NH_4^+ takes much longer.

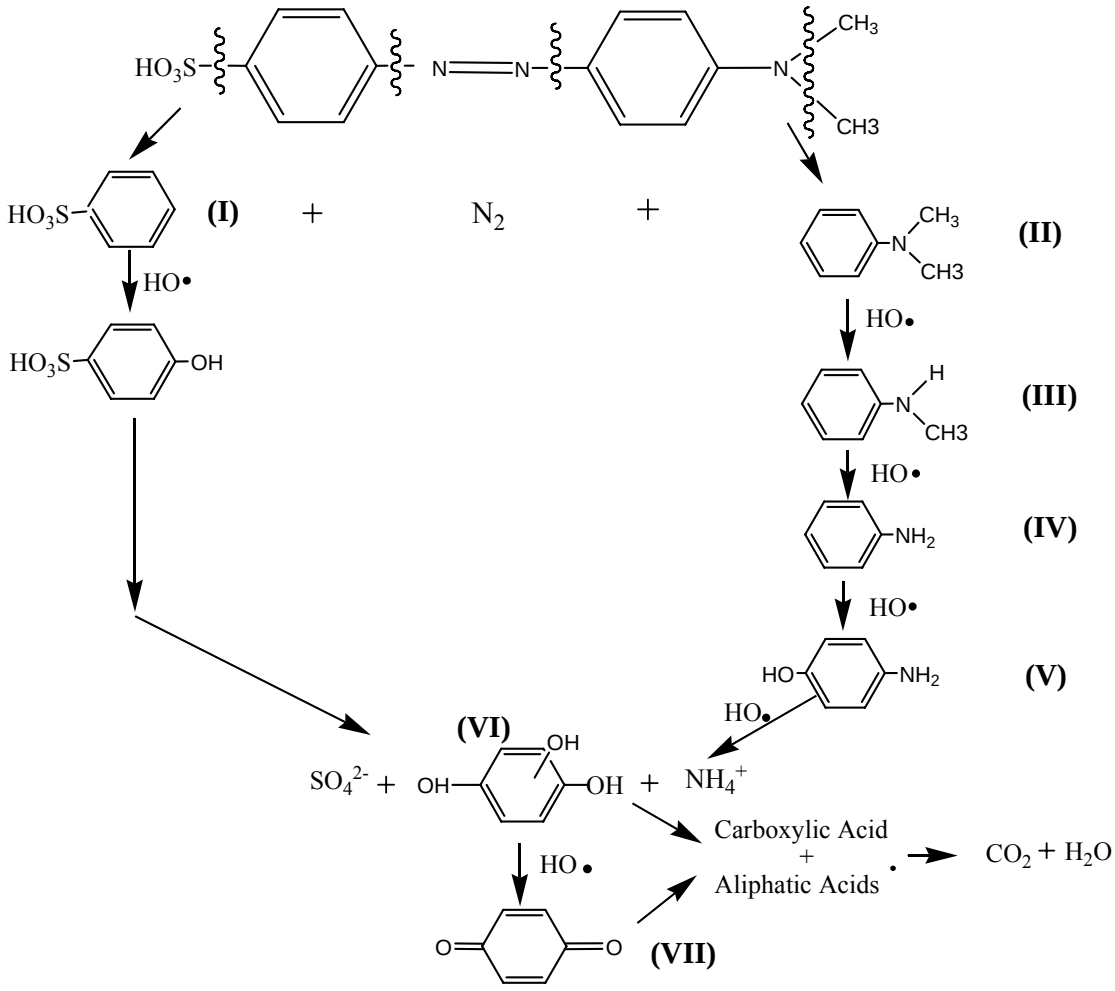

Figure 4.49. Postulated Degradation Mechanism of MeO

4.4.7. Proposed Model for TiO_2 Loading on ZSM-5 and Metal-Oxide Incorporations on TiO_2-ZSM-5 Surfaces and General Remarks

On the basis of our experimental analysis, a rough model for TiO_2 loading on ZSM-5 and metal-oxide incorporations on TiO_2-ZSM-5 surfaces is carried out (Figure 4.50). Before loading, the raw zeolite surface is covered with oxide thin layer and H^+ cations due to the adsorption of H_2O molecules. It is notable that the oxygen at the surface, which is combined with Al, is much more active than that combined with Si, due to the different electronic capability of Al and Si. Such Al sites are also referred as Lewis acid sites in the theory section of this study. The TiO_2 solution is like a random thread with –O-Ti- as the backbone and –OH covering the surface after the hydrolysis reaction of titanium propoxide with acetic acid (Figure 4.50 b).

When TiO_2 and ZSM-5 solutions are mixed together, the following routes are proposed for the combination of TiO_2 nanoparticles with the ZSM-5 surface [59].

1. The TiO_2 solution provides H^+ ions, and that's why -H reacts with the surface –OH, which has been combined with Al from ZSM-5, to create H_2O (Figure 4.50 a). And the left ≡Ti-O combines with -Al≡ to create the new Ti-O-Al bond.

2.The TiO_2 solution also provides –OH to react with the surface H- from ZSM-5 to produce H_2O. Thus, the left ≡Ti- is near to the O-Al≡. Then because of the static stress, the new bond Ti-O-Al comes into account.

Since ZSM-5 that we work with has a Si:Al=1000, the number of active adsorptions sites known as Lewis acid sites are limited. However, when the special surface Si atom is combined with the other three Si-O tetrahydron, the bond between this Si and the surface O becomes much weaker. Then, –H supplied from the acidic TiO_2 solution reacts with the surface oxygen of special Si to create H_2O. And, eventually, the left ≡Ti-O- combines with special –Si≡ to create Ti-O-Si new bond (Figure 4.50 c). Similarly, metal oxide nanoparticles

are assumed to occupy free-acidic sites and/or special –Si≡ sites to form M-O-Al and/or M-O-Si new bonds (Figure 4.51).

a)

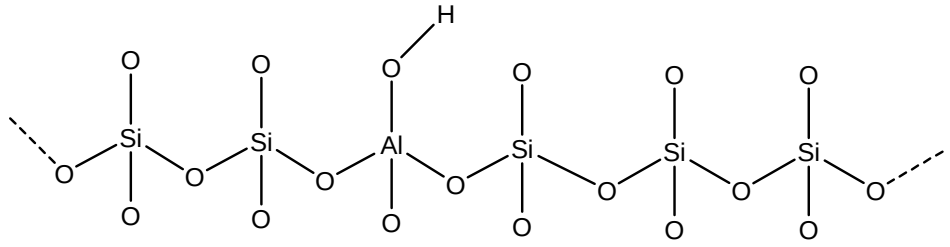

b)

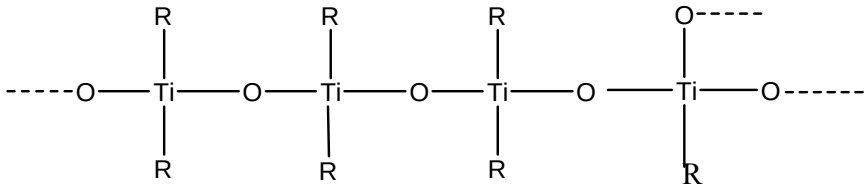

c)

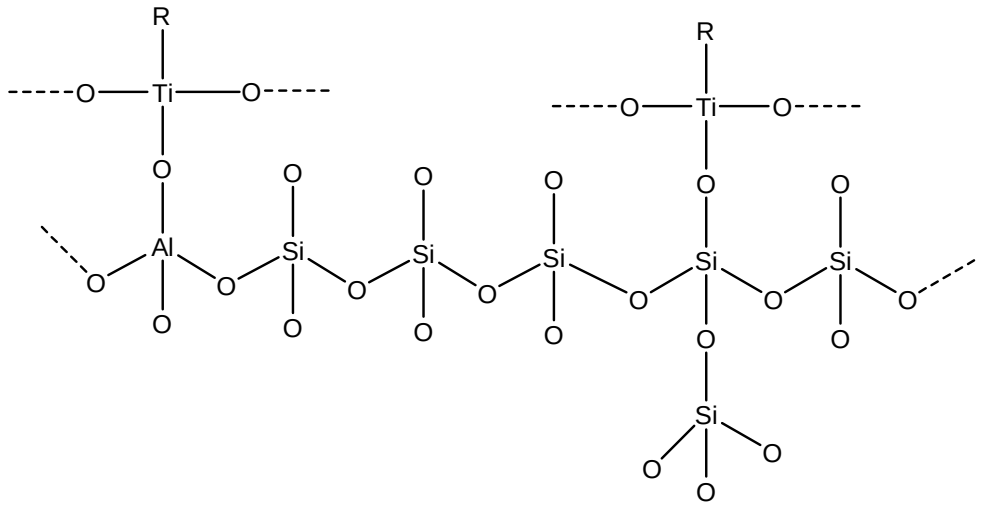

Figure 4.50. Proposed incorporation of TiO_2 on raw ZSM-5. (–R represents the –OH group)

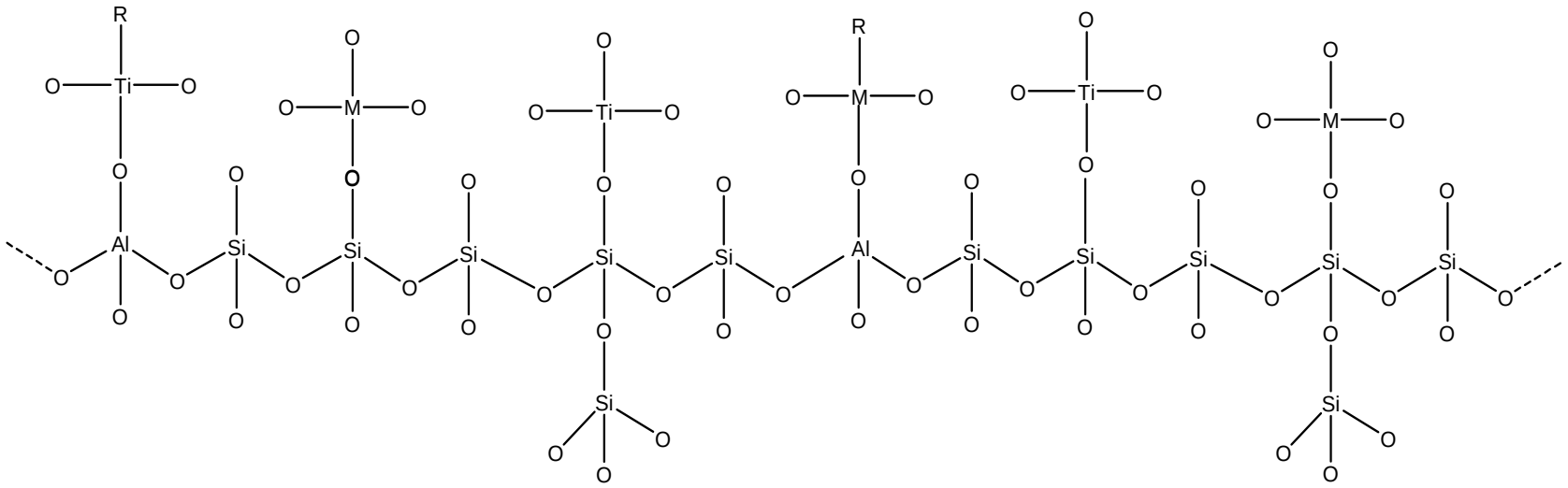

Figure 4.51. Proposed incorporation of metal oxides on TiO_2-ZSM-5 surface

Our SEM, XRD and AFM characterization results strongly support the above routes of adsorption processes. SEM image of 40-TiO_2-ZSM-5 catalyst showed that the aggregated TiO_2 particles of several nanometers spread on the surface of zeolite crystals of ca. 3-4 μm. In the XRD analysis, according to the Scherrer's equation, 15-35 nm sized anatase particles are evaluated for TiO_2-ZSM-5 catalysts depending on the content of TiO_2 at 400°C. As a function of calcination temperatures, 35-43 nm sized anatase particles at 400 and 600°C and 126-191 nm sized rutile particles at 800 and 1000°C are calculated in the presence of 40-TiO_2-ZSM-5 catalysts. In the case of metal loaded catalysts, for the same metal ion percentage (0.28 at. per cent), 26-46 nm sized anatase particles and 58-441 nm sized rutile particles are found. Variation in metal ion concentration does not cause a significant change both in the anatase and rutile sizes. Diameters of metal oxides are also calculated in metal ion containing catalysts. Around 20-25 nm sized La_2O_3 and Ce_2O_3 particles are obtained at different calcination temperatures. On the contrary, Y_2O_3 nanoparticles are evaluated as 42-49 nm. The particle sizes detected from the two dimensional (top-view) AFM images (Section 4.1.3) also indicate agglomeration of particles and results in much bigger sizes compared to the ones obtained from XRD analysis. Since all these diameter values are much greater than the reported diameter of ZSM-5 cavity (0.55 nm), major parts of TiO_2 and metal oxide particles are considered to exist on the outer surfaces of ZSM-5 support. The adsorption of MeO on the raw ZSM-5 and all supported catalysts is another important point on photocatalytic reactions. A detailed investigation of dark adsorption studies is mentioned in Section 4.4.3. According to the results of these experiments, an equilibration time in 30 min is achieved for ZSM-5 and supported catalysts. However, since the size of MeO is around 1 nm (due to the aromatic rings with large substituents of $–SO_3Na$ and $–N(CH_3)_3$) and the aperture size of ZSM-5 is about 0.55 nm, MeO cannot enter the inner surfaces of ZSM-5. So, for all supported catalysts, most of the MeO molecules can only be adsorbed on the outer surfaces of ZSM-5 at which TiO_2, Y_2O_3, La_2O_3 and Ce_2O_3 are already believed to exist.

It is also expected that incorporation of rare-earth-metal oxides onto a TiO_2-ZSM-5 matrix could provide a means to concentrate the MeO pollutant at the catalyst surface. $–SO_3Na$ functional group of MeO makes an interaction with the f-orbitals of lanthanides due to the ability of lanthanide ions to form complexes with various Lewis bases. The

places of these ions or their corresponding oxides are important; they may occupy free-acidic sites or special –Si≡ sites on TiO_2-ZSM-5 structrure (Scheme 3). If these sites are close to the TiO_2 locations, then the MeO molecule interacting with the metal oxides may easily spill over onto the TiO_2 sites, producing high photocatalytic activity.

The apparent decoloration of MeO solutions in the presence of supported catalysts is seen after 30 min irradiation, indicating loss of chromophoric group (-N=N-). This observation suggests that photocatalytic activities of supported catalysts are remarkable and photocatalytic degradation of MeO by these catalysts under UV illumination is possible. The decrease around 290 nm band indicates that photocatalytic degradation not only destroys the conjugate system but also destroys the benzene rings existing within the structure of MeO. However, according to the tentative mechanism proposed in Section 4.4.6, some intermediates forming during the irradiation experiments also constitute benzene or substituted benzene groups. Since such groups may also demonstrate an absorption maximum around 300 nm, we could not easily follow the decrement in 290 nm band of MeO in our experiments. That's why, in this study, the temporal change in the concentration of MeO is monitored only by examining the variation in maximal absorption band (around 460 nm).

The photodegradation of MeO is investigated by using the as-prepared catalysts and following the various effects. In the effect of TiO_2 loading, again considering the adsorption processes, an average loading of 40 per cent titania-sol addition is accepted. When the effect of metal ion incorporation on a TiO_2-ZSM-5 matrix is considered, for all supported catalysts, the highest degradation is achieved for the lowest metal ion content. And, for the same percentages, yttrium loaded catalyst shows the best efficiency whereas cerium loaded catalyst exhibits the worst degradation performance. Since adsorption capacities of all catalysts strongly depend on pH, a detailed pH effect in the dark and under irradiation is examined. For acidic pH values at which $pH<pH_{pzc}$, adsorption of MeO is favored due to the positively charged catalyst surfaces. However, at alkaline pH values where $pH>pH_{pzc}$, poor adsorption of MeO leads to a decrease in degradation efficiencies of supported catalysts. Before and after examining the pH effect, experiments are carried out

at the natural pH value of 3.27 mg/L MeO solution (pH=5.85) in order not to include an additional ion effect coming from HCl or NaOH sources used for the regulation of desired pH values of solutions. The photocatalytic degradation of MeO follows first-order kinetics. The apparent rate constant for each supported catalyst is found to decrease as MeO concentration increases due to the reduction in the generation of $OH^{\bullet}$ radicals. Langmuir-Hinshelwood model is also applicable to MeO degradation. Although, 0.28 Y-40 TiO_2-ZSM-5 possesses the lowest adsorption constant, its reaction rate constant is much greater in comparison to other metal-oxide including supported catalysts.

The variation in photocatalytic efficiencies of 0.28 Y-40 TiO_2-ZSM-5, 0.28 La-40 TiO_2-ZSM-5 and 0.28 Ce-40 TiO_2-ZSM-5 may lie in the differences of electronic configurations of metal ions and also in the diameter differences of corresponding metal oxides. The configuration of metal "Y" is [Kr] $5s^2$ $4d^1$, metal "La" is [Xe] $6s^2$ $5d^1$ and metal "Ce" is [Xe] $6s^2$ $4f^1$ $5d^1$. According to the ions precursors ($Y(NO_3)_3.6H_2O$, $La(NO_3)_3.6H_2O$, $Ce(NO_3)_3.6H_2O$) used in this study, Y^{3+} stays with [Kr] core, La^{3+} stays with [Xe] core, Ce^{3+} stays with [Xe] $4f^1$ configuration . Formation of a complex with at least one-electron pair of sulfonic group in MeO molecule is expected by filling empty 4d or 4f orbitals of metal ions. In the presence of Y^{3+} and La^{3+} ions, empty two-4d orbitals and two-4f orbitals can be occupied, respectively. However, in the presence of Ce^{3+} ion, new-electron pair will fill two-other 4f orbitals which leads to three un-paired electrons and the most unstable configuration among the supported catalytsts. According to XRD analysis of 0.28 Y-40 TiO_2-ZSM-5, 0.28 La-40 TiO_2-ZSM-5 and 0.28 Ce-40 TiO_2-ZSM-5 catalysts prepared at the same temperature, almost no difference is noticed in anatase nanoparticle sizes. However, when metal oxide sizes are compared, Y_2O_3 nanoparticles (around 49 nm) are found to be bigger than La_2O_3 and Ce_2O_3 nanoparticles. Two-dimensional AFM image of 0.28 Y-40 TiO_2-ZSM-5 exhibits well-dispersed particles of 53 nm. This average particle size is the lowest value in comparison to the ones obtained in the presence of other supported catalysts and even in the presence of 40-TiO_2 (400°C). The consistency between XRD and AFM results for 0.28 Y-40 TiO_2-ZSM-5 catalyst leads us to think about that MeO adsorption factor on the photocatalytic activity is very limited. Accordingly, 0.28 Y-40 TiO_2-ZSM-5 induces the lowest adsorption constant. Simultaneously, observation of the highest reaction rate constant with the same catalyst enhances the idea of degradation

in the solution phase instead of the catalyst surface. One last consideration concerning all supported catalysts, we believe that much more smaller sized TiO_2 and metal oxide nanoparticles also exist in our final catalyst configurations although they are not detectable or measurable according to our characterization techniques. Thus, increase in photoactivities may be explained with the presence of these species as well.

To sum up our experimental results, although ZSM-5 is selected as a support due to its high surface area and porous structure, neither anatase particles nor metal oxide particles enter the cavities of ZSM-5 specifically according to our XRD and AFM results. They only fill the outer surfaces of the support by extremely decreasing its surface area. The photocatalytic efficiency of supported catalysts is also compared with that of commercial TiO_2 Degussa (P-25) and 40-TiO_2. Approximately the same surface area with much smaller anatase particle diameters is attained with 40-TiO_2 catalyst prepared at 400°C in the absence of ZSM-5 support. Accordingly, the activity of this catalyst is found to be higher than the supported ones. The conventional TiO_2 (P-25), despite its higher particle dimensions, is found to be much more effective than 40-TiO_2 (400°C) and supported catalysts. The reason behind this efficiency may be explained by the special structural domain of Degussa where all anatase particles (80 per cent) play major role in degradation process. However, the reported particle size dimension (around 30 nm) does not coincide with our calculated value (around 140 nm) from Sherrer's equation. Based on this, since we are not able to check the surface area of this commercial source, we are not sure about the reported surface area of Degussa (50 g/m^2). Thus, comparison of Degussa with the other catalysts prepared in this study may not be a true evaluation. And, finally, although supported catalysts are often reported to be less photoactive due to the interaction of TiO_2 with the support, we find a positive effect for our supported catalysts due to the increase in the adsorption of probe molecule onto the support, TiO_2, Y_2O_3, La_2O_3 and Ce_2O_3 nanoparticles. Figure 4.48 shows photoactivities of all catalysts in 150 min irradiation period. In the inset of the figure, catalytic activity of Degussa P-25 is compared with the catalysts prepared in this study.

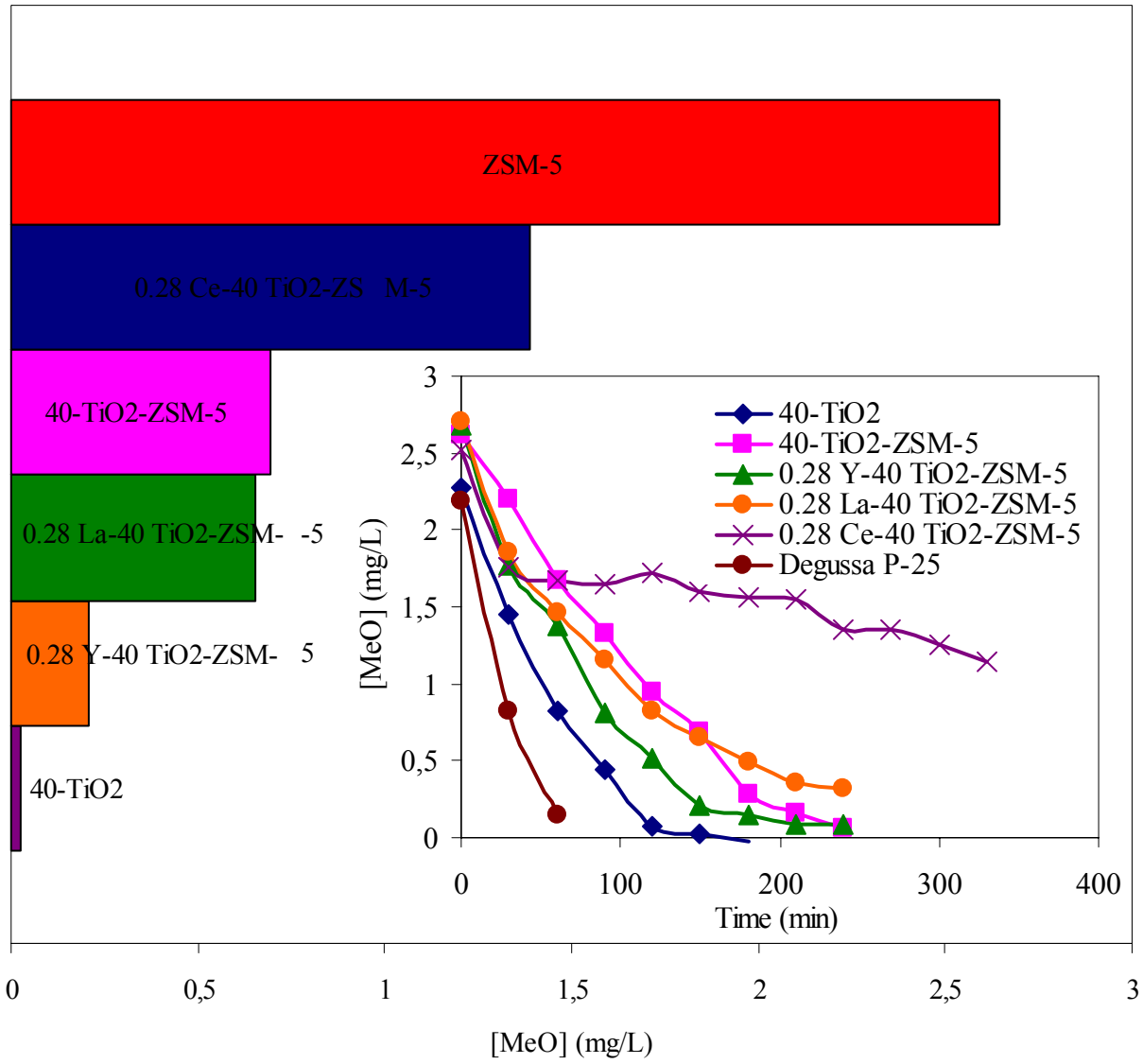

Figure 4.48. Photoactivities of 40-TiO_2 (400°C), 40 TiO_2–ZSM-5 (400°C), 0.28 Y-40 TiO_2–ZSM-5 (400°C), 0.28 La-40 TiO_2–ZSM-5 (400°C), 0.28 Ce-40 TiO_2–ZSM-5 (400°C) catalysts after 150 min irradiation time. Inset: Comparison of Degussa P-25 with the catalysts prepared in this study

5. CONCLUSIONS

In this study, 40-TiO_2 (sol-gel), TiO_2 supported ZSM-5 and rare-earth metal oxide supported TiO_2-ZSM-5 catalysts are produced, characterized and evaluated for photodegradation of model compound (MeO) under UV illumination.

The results of characterization techniques (SEM-EDX, XRD, BET and AFM) show that TiO_2 is in the anatase form for the lower temperatures of preparation. Also, TiO_2 and metal oxide (Y_2O_3, La_2O_3, Ce_2O_3) nanoparticles are formed on mainly the outer surface of ZSM-5 support.

The results of the photocatalytic reactions apparently exhibit the following sequence for the efficiencies of all prepared catalysts at 400°C and TiO_2 (Degussa P-25):

TiO_2 (Degussa P-25) > 40-TiO_2 > 0.28 Y-40 TiO_2-ZSM-5 > 0.28 La-40 TiO_2-ZSM-5 > 40-TiO_2-ZSM-5 > 0.28 Ce-40 TiO_2-ZSM-5

The conventional TiO_2 (Degussa P-25) catalyst, despite its higher particle dimensions is found to be more effective than supported TiO_2 nanoparticles in the MeO degradation process. The limited photocatalytic activity of nanoparticle-based systems (in comparison to Degussa P-25 and 40-TiO_2 catalysts) can be ascribed to the fact that the immobilization process reduces the active surface area available for adsorption and catalysis.

Finally, it is worthwhile to note that an enhancement of the performance of the nanoparticle-based catalysts can be obtained by optimizing the incorporation techniques in order to achieve an highly porous nanocrystal-based catalysts, able to overcome the drawbacks deriving from the lost in active surface area due to immobilization.

REFERENCES

1. Yoon K. B., "Electron- and Charge-Transfer Reactions within Zeolites", *Chemical Reviews*, Vol. 93, pp. 321, 1993

2. Braun I., G. Ihlein, F. Laeri, U. Nöckel, Ö. Weiss, "Catalytic reduction of N_2O over steam-activated FeZSM-5 zeolite: Comparison of CH_4, CO, and their mixtures as reductants with or without excess O_2", *Applied Physics B*, Vol. 70, pp. 335, 2000

3. Marlow F., J. Caro, L. Werner, J. Karnaowski, S. Dahne, "Optical Second Harmonic Generation of (Dimethy1amino)benzonitrile Molecules Incorporated in the Molecular Sieve AlP04-5", *Journal of Physical Chemistry*, Vol. 97, pp. 11286, 1993

4. Van Bekkum H., E. M. Flanigen, P. A. Jacobs, J. C. Jansen, *Introduction of Zeolite Science and Practice*, second edition, Elsevier, Amsterdam, 2001

5. Takeuchi M., T. Kimura, M. Hidaka, D. Rakhmawaty, M. Anpo, "Photocatalytic Oxidation of Acetaldehyde with Oxygen on TiO_2/ZSM-5 Photocatalysts: Effect of Hydrophobicity of Zeolites", *Journal of Catalysis*, Vol. 246, pp. 235, 2007

6. Corma A., Chemical Reviews, "Inorganic Solid Acids and Their Use in Acid-Catalyzed Hydrocarbon Reactions", Vol. 95, pp. 559, 1995 OR Hattori H., *Chemical Reviews*, Vol. 95, pp. 537, 1995

7. Hashimoto, S., "Zeolite photochemistry: impact of zeolites on photochemistry and feedback from photochemistry to zeolite science", *Journal of Photochemistry and Photobiology C: Photochemistry Reviews* Vol. 4, pp. 19–49 Review, 2003)

8. Catlow, C.R.A., *Modelling of Structure and Reactivity in Zeolites*, London, 1992

9. Subotic B., A. Graovac, L. Sekovanic, *Progress Report and Discussion of Fifth International Conference in Zeolites*, Giannini, Naples, pp. 55-57, 1980

10. Carp O., C.L. Huisman , A. Reller, "Photoinduced reactivity of titanium dioxide", *Progress in Solid State Chemistry,*Vol. 32, pp. 33-177, 2004

11. Schulz J, Hohenberg H, Pfuck F, Gartner E, Will T, Pfeiffer S, "Distribution of sunscreens on skin", *Advance Drug Delivery Review*, Vol. 54, pp. 157, 2002

12. Schwaz VA, Klein SD, Hornung R, Knochenmuss R, Wyss P, Fink D, "Skin protection for photosensitized patients", *Lasers in Surgery and Medicine*, Vol. 29, pp. 252, 2001

13. Yu, P. And M. Cardona, "Fundamentals of Semiconductors", *Physics and Materials Properties*, 2nd ed., Springer, Newyork, 1999

14. M. Anpo, M. Takeuchi, K. Ikeue, S. Dohshi, "Design and development of titanium oxide photocatalysts operating under visible and UV light irradiation.: The applications of metal ion-implantation techniques to semiconducting TiO_2 and Ti/zeolite catalysts", *Current Opinion in Solid State and Material Science*, Vol. 6, pp. 381-388, 2002

15. McMurraya T.A., J. A. Byrne, P.S.M. Dunlop, J. G. M. Winkelman, B.R. Eggins, E. T. McAdamsa, "Intrinsic kinetics of Photocatalytic Oxidation of Formic and Formic Oxalic Acid on Immobilised Films", *Applied Catalysis A: Genera,* Vol. 262, pp. 105-110, 2004

16 Carp, O., C. L. Huisman and A. Reller, "Photoinduced Reactivity of Titanium Dioxide", *Progress in Solid State Chemistry*, Vol. 32, pp.33-177, 2004

17. Atkins P., Julio de Paula, "*Atkin's Physical Chemistry*", 7th ed., New York, 2002

18. Jung Y. K., S. B. Park, "Anatase-phase Titania: Preparation by Embedding Silica and Photocatalytic Activity for the Decomposition of Tricholoroethylene", *Journal of Photochemistry and Photobiology A: Chemistry*, Vol. 127, pp. 117-122, 1999

19. Bach U., Lupo D., Comte P., Moster J.E., Weissortel F., **"**Solid-state dye-sensitized mesoporous TiO_2 solar cells with high photon-to-electron conversion efficiencies", *Nature,* Vol. 395, pp. 583, 1998

20. Takahashi Y., Matsuoka Y, "Dip-coating of TiO_2 films using a sol derived from Ti(O-*i*-Pr)$_4$-diethanolamine-H_2O-*i*-PrOH system", *Journal of Materials Science*, Vol. 23, pp. 2259-2266, 1988

21. Bhattacharyya A., S. Kawi and M.B. Ray, "Photocatalytic degradation of orange II by TiO_2 catalysts supported on adsorbents", *Catalysis Today*, Vol. 98, pp. 431-439, 2004

22. Li F. B, Li X. Z, Hou F., "Photocatalytic degradation of 2-mercaptobenzothiazole in aqueous La^{3+}–TiO_2 suspension for odor control", *Applied Catalysis B: Environmental*, Vol. 48, pp. 185-194, 2004

23. Hermann JM, Disdier J, Pichat P., "Effect of chromium doping on the electrical and catalytic properties of powder titania under UV and visible illumination", *Chemical Pysics Letters,* Vol. 108, pp. 618-622, 1984

24. Agatino Di Paola, Elisa Garc´ıa-López, Giuseppe Marc, Cristina Mart´ın , Leonardo Palmisano, Vicente Rives, Anna Maria Venezia, "Surface characterization of metal ions loaded TiO_2 photocatalysts: structure–activity relationship", *Applied Catalysis B: Environmental, Vol.* 48, pp. 223–233, 2004

25. Zhang Y., H. Zhang, Y. Xu, Y. Wang, "Europium Doped Nanocrystalline TiO_2: Preparation Phase Transformation and Photocatalytic Properties", *Journal of Matreials Chemistry*, Vol. 13, pp. 2261-2265, 2003

26. Xu Y., Cooper H. Langford, "Enhanced Photoactivity of a Titanium(IV) Oxide Supported on ZSM5 and Zeolite A at Low Coverage*", Journal of Physical Chem*istry, Vol. 99, pp. 11501-11507, 1995

27. Yang R. T., N. Tharappiwattananon and R. Q. Long, "Ion-exchanged pillared clays for selective catalytic reduction of NO by ethylene in the presence of oxygen *", Applied Catalysis B: Environmental,* Vol. 19, pp. 289-304, 1998

28. Lin J., Jimmy C. Yu, "An investigation on photocatalytic activities of mixed TiO_2-rare earth oxides for the oxidation of acetone in air", *Journal of Photochemistry and Photobiology A*: *Chemistry,* Vol. 116, pp. 63-67, 1998

29. Pal B., Maheshwar Sharon and Gyoichi Nogami, "Preparation and characterization of TiO_2/Fe_2O_3 binary mixed oxides and its photocatalytic properties", *Materials Chemistry and Physics* Vol. 59, pp. 254-261, 1999

30. Chen H., A. Matsumoto, N. Nishimiya and K. Tsutsumi, "Preparation and characterization of TiO_2 incorporated Y-zeolite", *Colloids and Surfaces A: Physicochemical and Engineering Aspects* Vol. 157, pp. 295-305, 1999

31. Kim Y. and Minjoong Yoon, "TiO_2/Y-Zeolite encapsulating intramolecular charge transfer molecules: a new photocatalyst for photoreduction of methyl orange in aqueous medium", *Journal of Molecular Catalysis A: Chemical* Vol. 168, pp. 257-263, 2001

32. Zhang Y., Anke Weidenkaff and Amin Reller, "Mesoporous structure and phase transition of nanocrystalline TiO_2", *Materials Letters* Vol. 54, pp. 375-381, 2002

33. Durgakumari V., M. Subrahmanyam, K. V. Subba Rao, A. Ratnamala, M. Noorjahan and Keiichi Tanaka "An easy and efficient use of TiO_2 supported HZSM-5 and TiO_2+HZSM-5 zeolite combinate in the photodegradation of aqueous phenol and p-chlorophenol", *Applied Catalysis A: General* Vol. 234, pp. 155-165, 2002

34. Francisco M., Valmor R. Mastelaro" Inhibition of the Anatase-Rutile Phase Transformation with Addition of CeO_2 to CuO-TiO_2 System: Raman Spectroscopy, X-ray Diffraction, and Textural Studies", *Chemistry of. Materials*, Vol. 14, pp. 2514-2518, 2002

35. Zhang Y., Stefan G. Ebbinghaus, Anke Weidenkaff, Thomas Kurz, Hans-Albrecht Krug von Nidda, Peter J. Klar, Martin Güngerich, and Armin Reller, "Controlled Iron-Doping of Macrotextured Nanocrystalline Titania", *Chemistry of Materials* Vol. 15, pp. 4028-4033, 2003

36. Zhang Y., H. Zhang, Y. Xu and Y. Wang, "Europium doped nanocrystalline titanium dioxide: preparation, phase transformation and photocatalytic properties**",** *Journal of Materials Chem*istry, Vol.13, pp. 2261-2265, 2003

37. Noorjahan M., V. Durga Kumari, M. Subrahmanyam and P. Boule "A novel and efficient photocatalyst: TiO_2-HZSM-5 combinate thin film", *Applied Catalysis B: Environmental* Vol. 54, pp. 155–163, 2004

38. Anipsitakis G. P., Dionysios D. Dionysiou, "Transition metal/UV-based advanced oxidation technologies for water decontamination", *Applied Catalysis B: Environmental* Vol. 54, pp. 155–163, 2004

39. Ismail A., Synthesis and characterization of $Y_2O_3/Fe_2O_3/TiO_2$ nanoparticles by sol–gel method1, *Applied Catalysis B: Environmental* Vol. 58, pp. 115–121, 2005

40. Dubey N., S. Rayalu, Nitin. K. Labhsetwar, R. Naidu, V. Chatti, S. Devotta, "Photocatalytic properties of zeolite-based materials for the photoreduction of methyl orange", Applied Catalysis A: General Vol. 303, pp. 152–157, 2006

41. Liu Y., Dezhi Sun, "Development of Fe_2O_3-CeO_2-TiO_2/γ-Al_2O_3 as catalyst for catalytic wet air oxidation of methyl orange azodye under room condition", *Applied Catalysis B: Environmental* Vol. 72, pp. 205–211, 2007

42. Pagga U., D. Brown, "Degradation of dyestuffs Part 2 Behaviour of dyestuffs in areobic biodegradation tests", *Chemosphere* Vol.15, pp. 476, 1986

43. Brown D., P. Laboureur, "Degradation of dyestuffs Part 2 Primary biodegradation under anaerobic conditions", *Chemosphere* Vol. 12, pp. 394, 1983

44. Kiriakidou F., D. Kondarides and E. Verykios, "The effect of operational parameters and TiO_2-doping on the photocatalytic degradation of azo-dyes" *Catalysis Today* , Vol. 54, pp. 119-130, 1999

45. Fuji T., T. Kodama, "Synthesis of Titania Pillared Mica in Aqueous Solution of Acetic Acid", *Journal of Porous Materials* Vol. 8, pp. 99, 2001

46. Matsuda Y., Y. Kıyamata, T. Kodama, M. Abe, "Synthesis of Titania Pillared Sepionite in Aqueous Solution of Acetic Acid", *Journal of Porous Materials* Vol. 5, pp. 121, 1998

47. Sayınsöz E., "*Characterization and Photocatalytic Activity of Sepiolite- TiO_2 and Na-Montmorillonite- TiO_2 catalyst*", M.S. Thesis, Boğaziçi University, 2006

48. Chen Y., C.Y. Lee, M.Y. Yeng, H.T. Chiu, "The effect of calcinations temperature on the crystallinity of TiO_2 nanopowders", *Journal of Crystal Growth*, Vol.247, pp. 363, 2003

49. Jung K., S. B. Park, "Anatase-phase titania: preparation by embedding silica and photocatalytic activity for the decomposition of trichloroethylene", *Journal of Photochemistry and Photobiology A*, Vol. 127, pp. 117, 1999

50. Su C., B.-Y. Hong, C.-M. Tseng, "Sol–gel preparation and photocatalysis of titanium dioxide", *Catalysis Today*, Vol. 96, pp. 119, 2004

51. Sobana N., M. Swaminathan, "The Effect of Operational Parameters on the Photocatalytic Degradation of Acid Red 18 by ZnO", *Seperation and Purification Technology*, Vol. 56, pp. 101-107, 2007

52. Wang J., Y. Jiang,Z. Zhnag, X. Zhang, T.Ma, G. Zhang, P. Zhnag, Y. Li, "Investigation on the Sonocatalytic Degradation of Acid Red B in the Presence of Nanometer TiO_2 Catalysts and Comparison of Catalytic Activities of Anatase and Rutile TiO_2 Powders", *Ultrasonics Sonochemistry*, Vol. 14, pp. 545-551, 2007

53. Wang W., Claudia Gomes Silva, Joaquim Faria, "Photocatalytic degradation of Chromotrope 2R using nanocrystalline TiO_2/activated-carbon composite catalysts", *Applied Catalysis B: Environmental*, Vol. 70, pp. 470–478, 2007

54. Ozen A., V. Aviyente , “Experimental and Modeling Approach to Decolorization of Azo Dyes by Ultrasound: Degradation of the Hydrazone Tautomer”, *Journal of Physical Chemistry A,* Vol. 109*, pp.* 3506-3516, 2005].

55. Joseph. J. M.; Destaillats, H.; Hung, H.; Hoffmann, M. R. “The Sonochemical Degradation of Azobenzene and Related Azo Dyes: Rate Enhancements via Fenton’s Reactions”, *Journal of Physical Chemistry. A*, Vol. 104, pp. 301-307, 2000

56. Spadaro J. T.; Isabelle, L.; Renganathan, V., “Hydroxyl radical mediated degradation of azo dyes: evidence for benzene generation” *Environmental Science Technology,* Vol. *28*, pp. 1389-1393, 1994

57. K. Ioannis, Triantafyllos Albanis, “TiO_2-assisted photocatalytic degradation of azo dyes in aqueous solution: kinetic and mechanistic investigations “, *Applied Catalysis B: Environmental* Vol. 49, pp. 1–14, 2004

58. Galindo C., Patrice Jacques and André Kalt, “Photodegradation of the aminoazobenzene acid orange 52 by three advanced oxidation processes: UV/H_2O_2, UV/TiO_2 and VIS/TiO_2 Comparative mechanistic and kinetic investigations “, *Journal of Photochemistry and Photobiology A: Chemistry*, Vol.130, pp. 35–47, 2000

59. Li F., Y. Jiang, L. Yu, Z. Yang, T. Hou, S. Sun, “Surface effect of natural zeolites on the photocatalytic activity of TiO_2”, *Applied Surface Science*, Vol. 252, pp. 1410-1416, 2005